

Detecting the Undetectable:
Functional Protein Motions in the Hidden Timescale Window
Revealed by NMR Relaxation Measurements

Dissertation
for the award of the degree
“Doctor rerum naturalium” (Dr. rer. nat.)
of the Georg-August-Universität Göttingen

within the doctoral program “Chemistry”
of the Georg-August University School of Science (GAUSS)

submitted by
Supriya Pratihar

from Kantapahari, India

Göttingen, 2021

Thesis Committee

Prof. Dr. Christian Griesinger
NMR-based Structural Biology
Max Planck Institute for Biophysical Chemistry, Göttingen, Germany

Prof. Dr. Ulf Diederichsen
Institute of Organic and Biomolecular Chemistry
Georg-August University, Göttingen, Germany

Prof. Dr. Bert de Groot
Computational Biomolecular Dynamics
Max Planck Institute for Biophysical Chemistry, Göttingen, Germany

Members of the Examination Board

Reviewer: Prof. Dr. Christian Griesinger
NMR-based Structural Biology
Max Planck Institute for Biophysical Chemistry, Göttingen, Germany

Second Reviewer: Prof. Dr. Andreas Janshoff
Institute for Physical Chemistry
Georg-August University, Göttingen, Germany

Further Members of the Examination Board

Prof. Dr. Bert de Groot
Computational Biomolecular Dynamics
Max Planck Institute for Biophysical Chemistry, Göttingen, Germany

Dr. Loren Andreas
NMR-based Structural Biology
Max Planck Institute for Biophysical Chemistry, Göttingen, Germany

Prof. Dr. Henning Urlaub
Bioanalytical Mass Spectrometry
Max Planck Institute for Biophysical Chemistry, Göttingen, Germany

Prof. Dr. Helmut Grubmüller
Theoretical and Computational Biophysics
Max Planck Institute for Biophysical Chemistry, Göttingen, Germany

Date of oral examination: 02.11.2021

Affidavit

I hereby declare that this thesis entitled “Detecting the Undetectable: Functional Protein Motions in the Hidden Timescale Window Revealed by NMR Relaxation Measurements” represents my own work with no other sources and aids than quoted.

Place, Date

Signature

“How can the events in space and time which take place within the spatial boundary of a living organism be accounted for by physics and chemistry?”

--Erwin Schrödinger

Acknowledgement

This thesis would not be possible without the support of many people, to whom I am very grateful.

First, I would like to express my gratitude to my supervisor Prof. Dr. Christian Griesinger for giving me the opportunity to perform my doctoral work under his supervision and for his constant guidance and input throughout these years. This helped a lot in driving the projects forward.

I would like to thank Prof. Dr. Ulf Diederichsen and Prof. Dr. Bert de Groot for being part of my thesis committee and their feedback during our meetings. Furthermore, I would like to thank all members of the examination board for the evaluation of my dissertation.

I am very grateful to Prof. Dr. Donghan Lee for educating me with both practical and theoretical knowledge of NMR and guiding me in all the projects described in thesis.

Prof. Dr. Helmut Grubmüller and Prof. Dr. Bert de Groot for fruitful discussions and collaboration. Dr. Loren Andreas for discussions and help in measurements.

I am also thankful to Dr. Jithender Reddy Gurralla for sharing his pulse programming knowledge with me and for being actively involved in the p53-TAD project. With Dr. Adolfo Moraes I had many insightful discussions one of which, led to the finding of the linear decay in RD profiles.

Dr. Stefan Becker and his group; Karin Giller, Melanie Wegstroth and Claudia Schwiegk for providing the high quality protein samples without which none of these projects would have been successful.

Dr. Dirk Bockelmann for helping with all IT related problems and Petra Breiner for the administrative supports.

A special thanks to Niels Karschin and Dr. Venus Singh Mithu for their help during the writing of this thesis. I am grateful to Dr. Colin Smith, Dr. Pablo Trigo Mourino, Dr. David Ban, Dr. Sebastian Frischkorn, Dr. Michael Sabo, Dr. Ashok Rout and all other present and past “cubic” group, lunch group and NMR-II members with whom I had insightful discussion.

I am especially grateful to my wife, parents and all other family and friends for their love and support.

List of Publications

- 1: Movellan KT, Najbauer EE, Pratihar S, Salvi M, Giller K, Becker S, Andreas LB. Alpha protons as NMR probes in deuterated proteins. *J Biomol NMR*. 2019 Feb;73(1-2):81-91. doi: 10.1007/s10858-019-00230-y. Epub 2019 Feb 14. PMID: 30762170; PMCID: PMC6441447.
- 2: Reddy JG, Pratihar S, Ban D, Frischkorn S, Becker S, Griesinger C, Lee D. Simultaneous determination of fast and slow dynamics in molecules using extreme CPMG relaxation dispersion experiments. *J Biomol NMR*. 2018 Jan;70(1):1-9. doi: 10.1007/s10858-017-0155-0. Epub 2017 Nov 29. PMID: 29188417.
- 3: Pratihar S, Sabo TM, Ban D, Fenwick RB, Becker S, Salvatella X, Griesinger C, Lee D. Kinetics of the Antibody Recognition Site in the Third IgG-Binding Domain of Protein G. *Angew Chem Int Ed Engl*. 2016 Aug 8;55(33):9567-70. doi: 10.1002/anie.201603501. Epub 2016 Jun 27. PMID: 27345359.
- 4: Chakrabarti KS, Ban D, Pratihar S, Reddy JG, Becker S, Griesinger C, Lee D. High-power (1)H composite pulse decoupling provides artifact free exchange-mediated saturation transfer (EST) experiments. *J Magn Reson*. 2016 Aug;269:65-69. doi: 10.1016/j.jmr.2016.05.013. Epub 2016 May 21. PMID: 27240144.
- 5: Smith CA, Ban D, Pratihar S, Giller K, Paulat M, Becker S, Griesinger C, Lee D, de Groot BL. Allosteric switch regulates protein-protein binding through collective motion. *Proc Natl Acad Sci U S A*. 2016 Mar 22;113(12):3269-74. doi: 10.1073/pnas.1519609113. Epub 2016 Mar 9. PMID: 26961002; PMCID: PMC4812760.
- 6: Smith CA, Ban D, Pratihar S, Giller K, Schwiegk C, de Groot BL, Becker S, Griesinger C, Lee D. Population shuffling of protein conformations. *Angew Chem Int Ed Engl*. 2015 Jan 2;54(1):207-10. doi: 10.1002/anie.201408890. Epub 2014 Nov 6. PMID: 25377083.
- 7: Michielssens S, Peters JH, Ban D, Pratihar S, Seeliger D, Sharma M, Giller K, Sabo TM, Becker S, Lee D, Griesinger C, de Groot BL. A designed conformational shift to control protein binding specificity. *Angew Chem Int Ed Engl*. 2014 Sep 22;53(39):10367-71. doi: 10.1002/anie.201403102. Epub 2014 Aug 12. PMID: 25115701; PMCID: PMC4497613.
- 8: Anoop A, Ranganathan S, Das Dhaked B, Jha NN, Pratihar S, Ghosh S, Sahay S, Kumar S, Das S, Kombrabail M, Agarwal K, Jacob RS, Singru P, Bhaumik P, Padinhateeri R, Kumar A, Maji SK. Elucidating the role of disulfide bond on amyloid formation and fibril reversibility of somatostatin-14: relevance to its storage and secretion. *J Biol Chem*. 2014 Jun 13;289(24):16884-903. doi: 10.1074/jbc.M114.548354. Epub 2014 Apr 29. PMID: 24782311; PMCID: PMC4059132.
- 9: Mithu VS, Pratihar S, Paul S, Madhu PK. Efficiency of heteronuclear dipolar decoupling schemes in solid-state NMR: investigation of effective transverse relaxation times. *J Magn Reson*. 2012 Jul;220:8-17. doi: 10.1016/j.jmr.2012.04.005. Epub 2012 May 3. PMID: 22683576.
- 10: Chakraborty S, Pratihar S, Hosur RV. NMR derived model of GTPase effector domain (GED) self association: relevance to dynamin assembly. *PLoS One*. 2012;7(1):e30109. doi: 10.1371/journal.pone.0030109. Epub 2012 Jan 12. PMID: 22253896; PMCID: PMC3257262.

Abstract

About 50 years ago, even before NMR was ready to determine structure of proteins, it could unveil a surprising motion in aromatic side-chain (Wuthrich & Wagner, 1975) from 1D ^1H spectra. With decades of development, NMR is now the most powerful technique for studying atomic resolution dynamics in proteins at biological conditions, even inside live cells. Although NMR offers relaxation-based methods to determine motion on the entire dynamics timescale spectrum, accurate characterization of the supra- τ_c dynamics (4 ns-40 μs) was not possible due to technical limitations. Dynamics from this timescale window is indicated to play a decisive role in molecular recognition and binding events. By combining the advancement in hardware with smart design of pulse programs, we have developed a high-power RD (relaxation dispersion) method, which can accurately detect dynamics in this previously inaccessible window.

By applying this newly developed high-power $R_{1\rho}$ RD, a hidden supra- τ_c motion was found in the first loop of the well-known protein GB3. From the timescale of motion measured at several supercooled temperatures, the activation energy for the loop-motion was estimated to be 65.6 kJ mol $^{-1}$. Arrhenius extrapolation showed that the loop moves with a timescale of \sim 400 ns at physiological temperature of 308 K. Analyzing the 640-membered ERMD (Ensemble-Restrained-Molecular-Dynamics) RDC ensemble, we found elevated dynamics from higher fluctuation of backbone atoms as well as lower supra- τ_c order parameters ($S_{\text{supra}}^2 = S_{\text{RDC}}^2/S_{\text{LS}}^2$) in the region where RD is detected. Interestingly, the newly observed supra- τ_c motion takes place in a region, which binds to antibodies. This hints to a link of the observed motion with the antibody recognition of GB3.

After unveiling a functional backbone motion in GB3, in chapter 2 we have studied the dynamics of methyl groups in the side-chains of ubiquitin, with a new type of RD method; ^{13}C Extreme-CPMG (E-CPMG), developed in our group. This method can cover the detectable timescale range of both conventional CPMG and $R_{1\rho}$. E-CPMG reported the same timescale and amplitude of motion, which was previously found from $R_{1\rho}$ measurements with much longer measurements time. Similarity in timescale and activation energy of the detected side-chain motion with previously found backbone dynamics hints towards a common mechanism. This hypothesis was proven by the absence of the side-chain motion in two different single point mutants (E24A and G53A), which were designed and tested for the quenching of backbone dynamics.

In chapter 3, we have extended the E-CPMG approach to a nucleus (^1H) with higher gyromagnetic ratio, where we could generate higher B_1 field with less applied RF power. We found and corrected a linear decay in RD profiles, arising from the phase cycle, which is widely used even in conventional CPMG measurements. Using this approach, we could detect the peptide-flip induced breathing motion in twice as many residues in ubiquitin compared to a previous report. In addition, we could directly detect the large amplitude pincer-mode motion for the first time, in segments where the existence of supra- τ_c motion was predicted from both RDC and MD simulations. This newly detected motion was already predicted to contribute to the conformational adaption power of ubiquitin while binding to other proteins.

Finally, in chapter 4, we found a very fast (4 μ s) dynamics at 263 K in an intrinsically disordered protein p53-TAD, in residues which are found to be in helical conformation in a bound complex. So far, this is the fastest detected motion with RD. The helical propensity was also predicted in the same stretch of residues from SSP (secondary structural propensity) score calculation with the experimental chemical shifts of the free protein. A great reduction in exchange rate (\sim 100 times) was found when the proline residue at the C-terminal of the helix was removed. In addition to that, more residues, including some from a second helix, were found to undergo conformational exchange. A doubling in helical propensity was found in this mutant (P27A) from SSP score calculations. In two other mutants (W23A; F19A and W23A; F19A; P27A) where the hydrophobic residues with aromatic side-chains were removed, no conformational exchange was detected. These findings suggest that the RD-observed 4 μ s motion could originate from fast folding of the transiently formed helix which is assisted by the hydrophobic core in the center.

In this thesis, by applying high-power RD, functionally relevant supra- τ_c motion is discovered in both backbone and side-chains of well-folded and disordered proteins. These findings helped in understanding molecular recognition and folding processes in the studied proteins.

Contents

1	Introduction.....	15
1.1	Characterization of Proteins	15
1.1.1	Protein Structure	15
1.1.2	Protein Dynamics.....	16
1.2	NMR for Protein Dynamics	17
1.2.1	Basic Concepts of NMR	17
1.2.2	NMR Relaxation	19
1.2.3	Chemical Exchange	19
1.3	Protein Dynamics from NMR: The Timescale Spectrum	22
1.4	Relaxation Dispersion	24
1.4.1	$R_{1\rho}$ Relaxation Dispersion.....	24
1.4.2	CPMG Relaxation Dispersion.....	25
1.4.3	Need for Speed: E-CPMG	26
1.5	The Current State of our Art: Thesis Outline.....	27
2	Antibody Recognition is Linked with Conformational Exchange in Protein GB3 ...	29
2.1	Introduction	29
2.2	Results and Discussion.....	30
2.3	Conclusion.....	37
2.4	Materials and Methods	38
2.4.1	Sample Preparation	38
2.4.2	NMR Experiments	38
2.4.3	Data Analysis	39
3	Common Origin of Backbone and Side-chain dynamics Found with ^{13}C E-CPMG..	41
3.1	Introduction	41
3.1.1	Side-chains: Powerful Probes for Structure and Dynamics.....	41
3.1.2	Hierarchy of Motion in Side-chains from $R_{1\rho}$ RD	41
3.1.3	Need for Speed: ^{13}C E-CPMG	42
3.2	Results and Discussion.....	43
3.3	Conclusion.....	49
3.4	Materials and Methods	50
3.4.1	Sample Preparation	50
3.4.2	NMR Experiments	51
3.4.3	Data Analysis	51
4	Direct Detection of Pincer Mode Motion in Ubiquitin by ^1H E-CPMG.....	53

4.1	Introduction	53
4.1.1	Ubiquitin: The key player in eukaryotic biology	53
4.1.2	“Blind-spot” in ubiquitin dynamics	54
4.2	Results and Discussions	55
4.2.1	¹ H E-CPMG: Linear Decay Compensation in RD Profiles	55
4.2.2	Peptide flip motion found in more residues	60
4.2.3	Pincer-Mode Motion Found in Ubiquitin	62
4.2.4	Arrhenius fitting of obtained timescale of motions	66
4.3	Conclusion.....	67
4.4	Materials and Methods	68
4.4.1	Sample Preparation	68
4.4.2	NMR Experiments	69
4.4.3	Data Analysis	70
5	Rapid Conformational Exchange in intrinsically disordered p53-TAD domain	71
5.1	Introduction	71
5.1.1	N-terminal TAD Domain of Protein p53	71
5.2	Results and Discussion.....	72
5.2.1	Fast Conformational Exchange Found in Wild-type p53-TAD.....	72
5.2.2	Slower Dynamics in P27A Mutant of p53-TAD	76
5.2.3	Removal of the Hydrophobic Patch (F19, W23) in the Core of Helix-1	81
5.3	Conclusion.....	82
5.4	Materials and Methods	83
5.4.1	Sample Preparation	83
5.4.2	NMR Experiments	83
5.4.3	Data Analysis	84
6	Conclusion and Outlook	87
7	Appendix.....	89
7.1	Figures and Tables	89
7.2	Pulse Programs.....	100
7.2.1	Backbone amide ¹ H R _{1ρ}	100
7.2.2	Side-chain ¹³ C E-CPMG	103
7.2.3	Backbone ¹ H E-CPMG	106
7.2.4	Backbone ¹⁵ N E-CPMG.....	110

1 Introduction

Physics began with a big bang about 14 billion years ago. 300,000 years later the universe became cool enough to let the chemistry happen by allowing the merging of neutrons, protons and electrons, forming atoms and then molecules. Finally, about 3.8 billion years ago on our planet earth biology started with the formation of living organisms. The Cell is the fundamental building block of all such existing lifeform (Alberts et al., 2015) on earth. Cells are nothing but a suspension of biomolecules separated by lipid bilayers from the environment (Pawson, 1995; Voet & Voet, 2000). Investigation of the interplay of these tiny biomolecules at various levels of functional and structural organization is the key to understand any life process. Having a link to all biological actions, proteins are one of the most versatile biomolecules that exist in cells. They perform a diverse array of functions, like cargo trafficking, cell signaling, immune response, cell adhesion, enzymatic functions and many more. (Voet & Voet, 2000).

1.1 Characterization of Proteins

1.1.1 Protein Structure

Thousands of atoms are connected in a defined spatial arrangement to constitute the structure of proteins. In a basic level, all protein molecules are polypeptide chains consisting of mainly twenty different kinds of L-amino acids, which are arranged following the primary sequence. Secondary structures in proteins are formed by intramolecular interaction (hydrogen bonds, salt bridge *etc.*) between amino acids, which are distant from one another in the primary sequence. These structural elements can be characterized by their characteristic dihedral angles (Balasubramanian & Ramakrishnan, 1972; Ramakrishnan & Ramachandran, 1965). In the next level of complexity, the tertiary structure in proteins is created by interactions of side-chains from different secondary structural elements, generating motifs and cavities for molecular recognition processes. Several protein chains or subunits can be packed together to make the protein structure of

highest complexity, known as the quaternary structure. Finding the spatial arrangement of atoms in a protein is the basic criterion to understand its function. Although there are techniques like X-ray crystallography and cryo-electron microscopy (cryo-EM) for obtaining atomic-resolution structures of proteins, nuclear magnetic resonance (NMR) is the only technique that can provide the same atomic resolution in solution and at near physiological conditions. Although in practice NMR measurements are often performed in conditions not identical to inside a cell, if needed it can be tuned to biologically relevant environments. In special cases, measurements can be done even in living mammalian cells causing almost no disturbance to the process under investigation (Sakakibara et al., 2009; Theillet et al., 2016). The isotopic labeling required for NMR study can be considered as minimally invasive as possible. In addition to studying rigid globular proteins, NMR is equally powerful for the investigations of intrinsically disordered proteins (IDPs), which is not possible by X-ray crystallography and cryo-EM. The structure of protease inhibitor IIA, is the first structure determined by solution NMR that came in 1985 (Williamson, Havel, & Wuthrich, 1985). Following this NMR has provided atomic resolution structure of many macromolecular complexes, which have played a crucial role in understanding many biological processes.

1.1.2 Protein Dynamics

Elements of life are marked by changes over time, and proteins are no exception. The spatial arrangement of atoms in the protein's structure does change over time. In addition to the structure of proteins, knowledge about these structural changes are crucial to understand its function. Biological processes in any organism are exquisitely mediated by changes in protein structure occurring on a wide range of timescales. Perturbation in amplitude and/or frequency of these conformational fluctuations could potentially lead to deadly diseases. In addition to the motions within one stable equilibrium structure, proteins undergo conformational exchanges between two or more equilibrium structures. These exchange processes in proteins provide them the necessary shape and form required, as for a particular function for example cargo trafficking, signal transduction and numerous enzymatic activities (Hammes-Schiffer & Benkovic, 2006; Tang & Kaneko, 2021). A special class of conformational transitions are found in so-called allosteric proteins. Substrate binding to one subunit of these multiunit proteins triggers a conformational change that alters the substrate affinity of the other subunits, thereby sharpening the

switching response of these proteins. Dynamics not only plays an important role in the native state of proteins for regulating their functions, the motional preferences of the polypeptide chain also influences the folding trajectory (Fossat, Garcia, Barrick, Roumestand, & Royer, 2016; Pawson, 1995).

Nuclear magnetic resonance (NMR) is the only technique that can capture protein dynamics with atomic resolution in biological ambience. Although structural ensembles are well characterized by molecular dynamics simulations, the kinetics of their interconversion is still very difficult to access computationally. The real strength of NMR comes from its capability of characterizing a wide range of timescales of motion and detecting lowly populated functional states. This is described in the following sections of this chapter.

1.2 NMR for Protein Dynamics

1.2.1 Basic Concepts of NMR

All NMR active nuclei have a nuclear spin angular momentum, whose magnitude is given by the equation

$$|\vec{I}| = \hbar \sqrt{I(I+1)} , \quad 1.1$$

where I is the spin angular momentum quantum number and \hbar is the reduced Planck constant. The z-component of $|\vec{I}|$ is

$$I_z = \hbar m_I , \quad 1.2$$

where m_I is the azimuthal quantum number which can assume values of $I, I-1, \dots, -I+1, -I$. If we restrict ourselves to only commonly used nuclei in protein NMR (^1H , ^{13}N and ^{15}N) (Cavanagh, Fairbrother, Palmer, Rance, & Skelton, 2007) the value of spin quantum number I is $\frac{1}{2}$. This gives two possible orientations of the nuclear spin; parallel and anti-parallel to the external magnet field. These states of different orientations are termed as α -state ($m_I = +1/2$) and β -state ($m_I = -1/2$), respectively. Magnetic moments ($\vec{\mu}_z$) corresponding to these two orientations are given by:

$$\vec{\mu} = \gamma \vec{I} \quad 1.3$$

$$\mu_z = \gamma I_z = \gamma \hbar m_I, \quad 1.4$$

where γ is the gyromagnetic ratio of the nucleus of interest. Energies for these two orientations are given by

$$E_{\pm} = \pm \frac{1}{2} \hbar \gamma B_0, \quad 1.5$$

where B_0 is the external magnetic field along the z-direction and \hbar is the reduced Planck constant. According to the Boltzmann distribution, the relative populations of these two states, in thermal equilibrium are expressed as following

$$\frac{N_{m_I}}{N} \approx \frac{1}{2} \left(1 + \frac{m_I \hbar \gamma B_0}{k_b T} \right), \quad 1.6$$

Where N_{m_I} denotes the number of spins in the spin state m_I , N is the total number of spins, k_b is the Boltzmann constant, and T is the temperature under consideration. The resulting bulk magnetization (M_0) along z direction is given by the following equation:

$$M_0 = \gamma \hbar \sum_{m_I=-I}^I m_I N_{m_I} \approx N I (I + 1) \frac{\gamma^2 \hbar^2 B_0}{3 k_b T} \quad 1.7$$

From equation 1.7 is it clear that the bulk magnetization depends on the three factors; the external magnetic field (B_0), the measurement temperature (T) and the gyromagnetic ratio of the nuclei. Hence for ^1H nuclei at room temperature, only one in 10^4 spins contributes to the detected NMR signal, making it a very insensitive technique compared to other types of spectroscopy. The relative energy difference between the populated states can be used to calculate the precession frequency (Larmor Frequency) along z-axis:

$$\omega = \frac{\Delta E}{\hbar} = \gamma B_0 \quad 1.8$$

Resonance occurs when an RF pulse ($\nu = \frac{\gamma B_0}{2\pi}$) is applied orthogonal to the z-axis (x-y plane) and the bulk magnetization is transferred to the x-y plane.

1.2.2 NMR Relaxation

Relaxation is the phenomenon where the bulk magnetization tends to go back to its equilibrium value. Time dependent oscillating local magnetic fields create relaxation in NMR. These oscillating magnetic fields, generated by the Brownian motion, are distributed over all frequencies. The probability of a motion to occur at a certain frequency is given by the spectral density function:

$$J(\omega) = \frac{2}{5} \left(\frac{\tau_c}{1 + \omega^2 \tau_c^2} \right) \quad 1.9$$

where τ_c is the rotational correlation time. Relaxation rates are described by a sum of Lorentzian functions at the respective Eigen frequencies of the spin system and the corresponding interaction strength of the relaxation mechanism. There are different pathways through which non-equilibrium magnetization decays. Longitudinal relaxation (R_1) describes the decay of non-equilibrium spin populations and transverse relaxation (R_2) describes the dephasing of bulk magnetization in the transverse plane. Among all sources of relaxation, chemical exchange is the most relevant one for the scope of this dissertation and is described below.

1.2.3 Chemical Exchange

Chemical exchange is discussed here from the equations derived from (Cavanagh et al., 2007) and the figure 1.1 is adapted from the PhD thesis of Dr. Sebastian Frischkorn. Chemical exchange describes the modulation of the chemical shift of a nuclear spin, which is involved in a time dependent exchange process. A two-state exchange is represented by



where k_{AB} and k_{BA} are the forward and the reverse rates for the exchange process respectively. The McConnell equation describing the effect of the exchange on the transverse relaxation is

$$\frac{dM^+(t)}{dt} = (i\Omega - R + K) M^+(t), \quad 1.11$$

where $M^+(t)$ is the time dependent transverse magnetization, Ω , R and K are chemical shift, relaxation and exchange matrices respectively (McConnell, 1958). These are related as

$$-i\Omega + R - K = \begin{pmatrix} -i\Omega_A - \rho_A + k_{AB} & -k_{BA} \\ -k_{AB} & -i\Omega_B - \rho_B + k_{BA} \end{pmatrix}, \quad 1.12$$

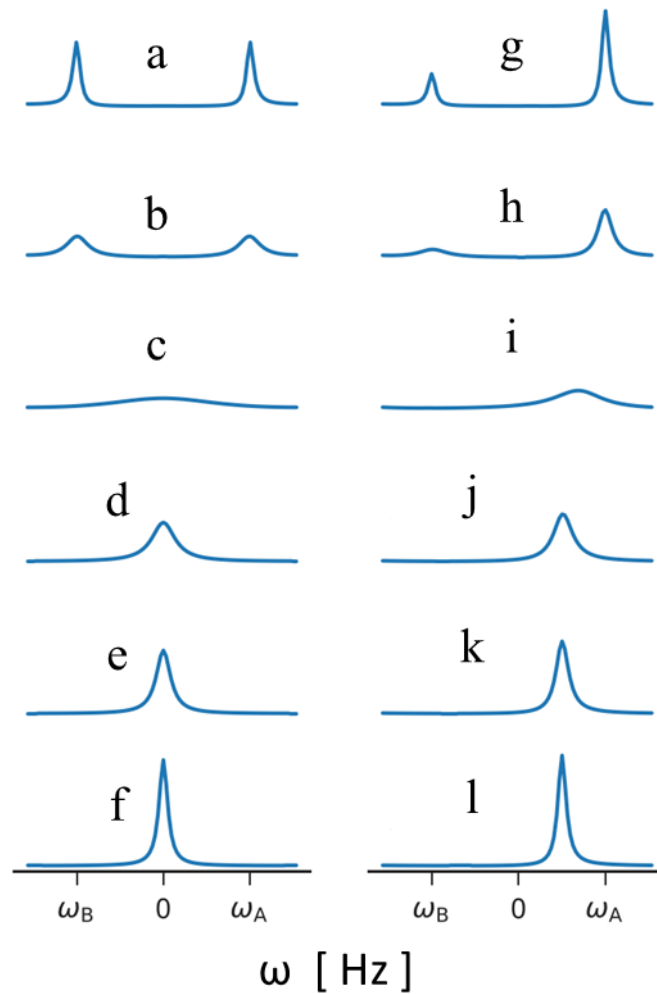


Figure 1.1: Effect of chemical exchange on the NMR resonance. The populations of both states are equal ($p_A = p_B$) in (a-f); in (g-l) $p_A = 4 p_B$. A difference in chemical shift of 200 Hz was kept between A and B. It was assumed that both the states has same intrinsic transverse relaxation rates (10 s^{-1}). Considered exchange rates are 0 s^{-1} (a, g), 20 s^{-1} (b, h), 200 s^{-1} (c, i), 900 s^{-1} (d, j), 2000 s^{-1} (e, k) and 10000 s^{-1} (f, l) for both equal and skewed population.

where ρ is the transverse relaxation rate and Ω is the chemical shift. Assuming that both the states have the same transverse relaxation rates ($R_{2,0}^A = R_{2,0}^B = R_{2,0}$), the eigenvalues (λ) of the rate matrix simplify to

$$\lambda_{\pm} = i\Omega - R_{2,\text{eff}}, \quad 1.13$$

where,

$$R_{2,\text{eff}} = R_{2,0} + \frac{k_{\text{ex}}}{2} \pm \frac{1}{\sqrt{8}} (k_{\text{ex}}^2 - \Delta\omega^2 + [(k_{\text{ex}}^2 + \Delta\omega^2)^2 - 16p_A p_B \Delta\omega^2 k_{\text{ex}}^2]^{1/2})^{1/2} \quad 1.14$$

and

$$\Omega = \frac{\Omega_A + \Omega_B}{2} \pm \frac{1}{\sqrt{8}} (\Delta\omega^2 - k_{\text{ex}}^2 + [(k_{\text{ex}}^2 + \Delta\omega^2)^2 - 16p_A p_B \Delta\omega^2 k_{\text{ex}}^2]^{1/2})^{1/2} \quad 1.15$$

are the observed transverse relaxation rate and chemical shift respectively, $k_{\text{ex}} (= k_{\text{AB}} + k_{\text{BA}})$ is the rate of exchange and $\Delta\omega$ is the chemical shift difference between two states. In the first exchange regime ($k_{\text{ex}} \gg \Delta\omega$) the population weighted transverse relaxation rate ($\overline{R_{2,0}}$) and chemical shifts ($\overline{\Omega}$) are given by

$$\overline{\Omega} = p_A \Delta\omega_A + p_B \Delta\omega_B \quad 1.16$$

$$\overline{R_{2,0}} = p_A R_{2,0}^A + p_B R_{2,0}^B \quad 1.17$$

The effect of exchange phenomenon on NMR signal is described in figure 1.1. When both the states are equally populated and no exchange is present, two peaks appear at their own chemical shifts with linewidth as expected from their intrinsic transverse relaxation rates. When the exchange rate is smaller than the chemical shift difference ($k_{\text{ex}} \ll \Delta\omega$; slow exchange) the exchange process will contribute (R_{ex}) in the relaxation process in addition to the intrinsic transverse relaxation rates ($R_{2,0}$) following the equation

$$R_{2,\text{eff}}^A = R_{2,0} + p_B k_{\text{ex}} \quad 1.18$$

The exchange contribution is maximum at the intermediate exchange regime ($k_{\text{ex}} \approx \Delta\omega$). In this condition the peak may be broadened beyond detection. If we keep increasing the exchange rates, after this point it enters the fast exchange regime ($k_{\text{ex}} > \Delta\omega$), where a single peak is observed at a population weighted chemical shift. When the exchange rate is much faster than the chemical shift difference ($k_{\text{ex}} \gg \Delta\omega$), the effective transverse relaxation rate is given by

$$R_{2,\text{eff}} = R_{2,0} + \frac{p_A p_B \Delta\omega^2}{k_{\text{ex}}} \quad 1.19$$

assuming both the states have same $R_{2,0}$ value. It can be seen from equation 1.19 that $R_{2,\text{eff}}$ has a quadratic dependence on the chemical shift differences between the states (in Hz). Due to this, it is easier to detect any exchange process at higher B_0 field. Also, the chemical

shift variance ($p_A p_B \Delta\omega^2$) gets scaled with k_{ex} before contributing to $R_{2,eff}$, which makes it difficult to detect exchange process at higher temperature where higher exchange rate is expected.

1.3 Protein Dynamics from NMR: The Timescale Spectrum

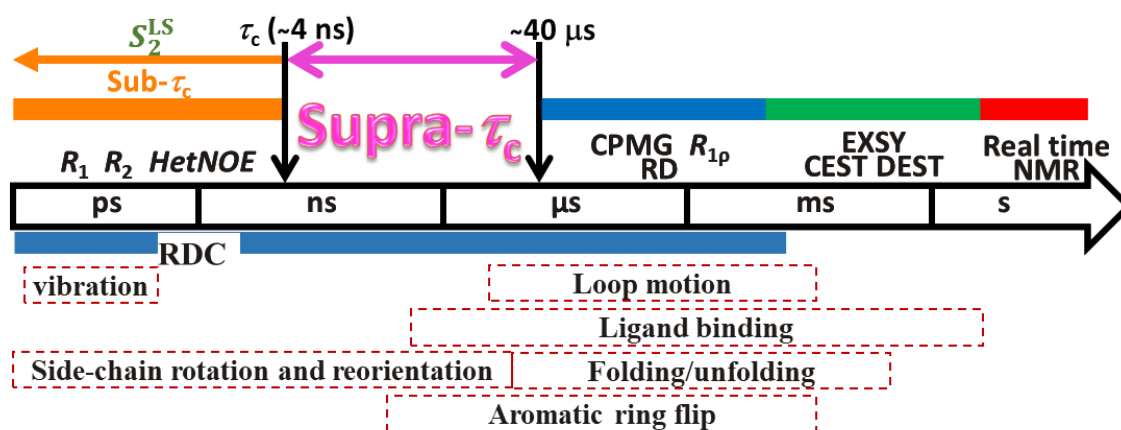


Figure 1.2: NMR detected protein dynamics timescale spectrum. A Wide range of timescales of motion appearing in proteins are shown together with the NMR based techniques that can detect those motions. The hidden supra- τ_c window of protein dynamics is highlighted in magenta.

To be able to carry out their functions, proteins carry a precise and required amount of rigidity and flexibility as designed by nature. Proteins should be flexible enough to allow product release and substrate binding; at the same time, they should also be able to retain the overall three-dimensional fold. “Evolutionary perfect” ubiquitin was found to contain a desired amount of structural dynamics, which made this protein as rigid as necessary and as flexible as required to provide the wide range of recognition capability (Lange et al., 2008). As depicted in figure 1.2, dynamics with a large range of lifetimes (picoseconds to seconds) are present in proteins. The bond vibrations and thermal fluctuations occur in the faster end of the spectrum and have lifetimes of picoseconds to nanoseconds. Rotation of methyl groups in the side-chains of amino acids also have this order of lifetimes. Whereas, the lid opening for nucleotide binding in adenylate kinase was found to be dependent on the collective domain motion which appears in the μ s-ms timescale (Wolf-Watz et al., 2004).

Although other methods exist for studying protein dynamics (Frauenfelder & Wolynes, 1985; Kolano, Helbing, Kozinski, Sander, & Hamm, 2006), NMR has the unique capability of studying protein motions in their native environments with its intrinsic atomic resolution. In NMR, rotational tumbling of the protein and other internal dynamics cause relaxation of nuclear magnetization. NMR uses this relaxation phenomenon to study motions in both the fast and the slow end of the timescale spectrum. In the previous decades, Lipari-Sabo order parameters (S_{LS}^2) (Lipari & Szabo, 1982a, 1982b), derived from R_1 , R_2 , and NOE values are extensively used to characterize motion faster than the rotational tumbling of proteins, termed as the sub- τ_c motion. These dynamics appear at the faster (ps-ns) end of the timescale spectrum. Slower internal motions in proteins, which have lifetime larger the rotational tumbling time (τ_c) do not affect the Lipari-Sabo order parameters. Although these fast local fluctuations in proteins contribute through entropy in binding events, the amplitude of movement is much smaller than what is expected in molecular recognition processes (Marlow, Dogan, Frederick, Valentine, & Wand, 2010; Yang, Mok, FormanKay, Farrow, & Kay, 1997). In the slower end of the spectrum, protein dynamics with lifetime higher than 10 milliseconds can be studied directly from NMR spectra because they results in peak-splitting. Exchange spectroscopy (EXSY) can track motions with lifetimes of 50ms to seconds, which was used to find the aromatic ring-flip in BPTI (Meier & Ernst, 1979). Slow turn-over events (Haupt et al., 2011) and folding processes (Zeeb & Balbach, 2004) are monitored by real-time NMR where the dynamics happens so slowly that it spans over several FIDs. The “dark” or “invisible” minor population of conformers are detected by Chemical Exchange Saturation Transfer (CEST) and Darks state Exchange-mediated Saturation Transfer (DEST) experiments. Both of these methods are extensions of the rotating frame relaxation dispersion approach ($R_{1\rho}$ RD), which is discussed in the following section. Cross-Correlated Relaxation (Reif, Hennig, & Griesinger, 1997) and Residual Dipolar Coupling (Lange et al., 2008; Meiler, Prompers, Peti, Griesinger, & Bruschweiler, 2001; Peti, Meiler, Bruschweiler, & Griesinger, 2002) can sense motions occurring on a large timescale window from ps-ms, covering both the sub- τ_c and the supra- τ_c window of the timescale-spectrum. Biologically significant process like protein folding and molecular recognition cannot be accessed by conventional sub- τ_c relaxation methods (S_{LS}^2) (Neira, 2013; Robustelli, Piana, & Shaw, 2020). The experimental design that gives the most detailed information about the supra- τ_c protein motions are relaxation dispersion (RD) experiments.

1.4 Relaxation Dispersion

The time-dependent fluctuations of chemical shift originating from conformational exchange can be a source of additional transverse relaxation (explained in section 1.4.1). This additional exchange contribution is detected by the relaxation dispersion (RD) method. NMR based RD is capable of giving crucial information about the timescale of exchange, the chemical shift difference between exchanging conformers and their populations. This helps in kinetic, structural and thermodynamic understanding of the process being monitored (Ban, Smith, de Groot, Griesinger, & Lee, 2017). There are two ways of quenching the chemical exchange contribution (R_{ex}) to the effective transverse relaxation ($R_{2,eff}$) which adds to the intrinsic transverse relaxation rate ($R_{2,0}$) originating purely from molecular tumbling.

$$R_{2,eff} = R_{2,0} + R_{ex} \quad 1.20$$

These are transverse rotating frame ($R_{1\rho}$) and Carr-Purcell-Meiboom-Gill (CPMG) based relaxation dispersion. Both these techniques are particularly useful in the fast exchange regime ($k_{ex} \gg \Delta\omega$), where a single resonance is observed at a population averaged chemical shift of both the exchanging partners. Both of these RD methods can be used to characterize lowly populated excited states (Korzhnev et al., 2004) as well as ground states (Ban et al., 2011) of protein conformations.

1.4.1 $R_{1\rho}$ Relaxation Dispersion

In the $R_{1\rho}$ experiment, the magnetization is locked in the rotating frame with a radio-frequency spin-lock (Cavanagh et al., 2007). The relaxation rate constant of this magnetization is measured with a varying amplitude and offset of the spin-lock. The effective field makes an angle with the B_0 field (z-axis), which is given by

$$\theta = \tan^{-1} \left(\frac{2 \pi \nu_{RF}}{\Omega} \right) \quad 1.21$$

where $2 \pi \nu_{RF}$ is the nutation frequency of the applied spin-lock B_1 field, and Ω is the offset between the NMR peak under consideration and the carrier frequency of the spin-lock. Both R_1 and R_2 contribute to the $R_{1\rho}$ value depending on the tilt angle (θ) and are calculated with the following equation:

$$R_{1\rho} = R_1 \cos^2 \theta + R_{2,eff} \sin^2 \theta \quad 1.22$$

In the case of on-resonance $R_{1\rho}$ the tilt angle is $\pi/2$, which eliminates the R_1 dependence, hence the knowledge of R_1 is no longer required for the analysis. Although this approach makes the analysis simpler, it increases the measurement time by an order of magnitude, since a separate set of on-resonance $R_{1\rho}$ experiments has to be measured for each peak. The off-resonance version of this experiment gains an advantage due to a higher effective field, given by

$$\omega_{eff} = \sqrt{(\Omega)^2 + (2\pi\nu_{RF})^2}. \quad 1.23$$

This permits detection of faster motions. The exchange contribution to off-resonance $R_{1\rho}$ is given by

$$R_{ex} = \frac{p_A p_B \Delta\omega^2 \tau_{ex}}{1 + (\omega_{eff} \tau_{ex})^2} \quad 1.24$$

where $\Delta\omega$ is the chemical shift difference between the exchanging conformers and τ_{ex} is the timescale of the exchange process which can be obtained from fitting the RD profile with equation 1.22.

1.4.2 CPMG Relaxation Dispersion

In the constant time CPMG (CT-CPMG) (Ban, Sabo, Griesinger, & Lee, 2013; Carr & Purcell, 1954; Cavanagh et al., 2007; Loria, Rance, & Palmer, 1999; Meiboom & Gill, 1958) RD experiments, the transverse effective relaxation rate is measured with a spin-echo sequence containing a series of 180° pulses with some inter-pulse delay (τ_{cp}). The spin-echo sequence causes dephasing of the spins and the amount of dephasing is proportional to the total CPMG delay (T_{CPMG}). When chemical exchange is present, the net magnetization is not refocused causing a broadening in the observed lines. With an increasing number of 180° pulses in the fixed CPMG delay the inter-pulse gap decreases. This gives less time to the chemical shifts of the exchanging partners to mix, which reduces the dephasing of magnetization and leads to sharper lines. This quenching of dephasing of transverse magnetization or $R_{2,eff}$ is performed with several inter-pulse (τ_{cp}) delays, generating different CPMG frequencies, which produce the RD profile.

$$\nu_{CPMG} = \frac{1}{4\tau_{cp}} \quad 1.25$$

In the fast exchange limit (the topic of this thesis) the RD profile is fitted with the simplified Luz-Meiboom model (Luz & Meiboom, 1963) as described by the following equation

$$R_{2,\text{eff}} = R_{2,0} + \frac{4\pi^2 B_0^2 \Phi_{\text{ex}}}{k_{\text{ex}}} \left(1 - \frac{4\nu_{\text{CPMG}}}{k_{\text{ex}}} \tanh\left(\frac{k_{\text{ex}}}{4\nu_{\text{CPMG}}}\right) \right), \quad 1.26$$

where, $\Phi_{\text{ex}} = p_A p_B \Delta\omega^2$ is the population weighted chemical shift variance (CSV) and $\Delta\omega$ is the chemical shift difference between the exchanging conformers.

1.4.3 Need for Speed: E-CPMG

As described in the previous sections, in both CPMG and $R_{1\rho}$ relaxation dispersion experiments, exchange contribution (R_{ex}) to effective transverse relaxation rates ($R_{2,\text{eff}}$) is quantified, which provide kinetic, thermodynamic and structural parameters of the motion under investigation (Ban et al., 2017; Neudecker, Lundstrom, & Kay, 2009; A. G. Palmer, Kroenke, & Loria, 2001). In $R_{1\rho}$ -based RD experiments, the additional exchange contribution is quenched by applying a spin-lock of variable radio frequency (RF) field strength. However, it is very difficult to precisely implement a spin-lock with weaker field strength (< 2 kHz) due to the higher spatial inhomogeneity of the B_1 field and nonlinearity of the amplifiers. In addition, at a weaker RF field, R_1 contributes more to $R_{1\rho}$ than $R_{2,\text{eff}}$, particularly for the resonances appearing far from the RF carrier offset. These off-resonance residues displays more pseudo-dispersion effects on the RD profiles originating from dipole-dipole (DD) and chemical shift anisotropy cross-correlated relaxation (CCR). These limitations demand $R_{1\rho}$ to be recorded at near on-resonance conditions that requires the measurement to be repeated at several narrow sampling offset for specific resonances. This needs prior knowledge about the residues, which are likely to undergo conformational exchange. On the other hand, CPMG-based RD experiments are commonly used to achieve quenching of exchange contributions at lower refocusing frequencies (Ishima, 2012; Ishima & Torchia, 2003). This RD data is then combined with the $R_{2,\text{eff}}$ values obtained with higher spin-lock fields in $R_{1\rho}$ to extract the kinetic parameters (Ban, Mazur, et al., 2013; Hansen, Vallurupalli, & Kay, 2008). In addition to the necessity of setting up two different sets of experiments, this approach is disadvantageous due to dissimilar heating effects. The entire applicable range of both conventional CPMG and $R_{1\rho}$ can be covered by slowly decreasing the inter-pulse delay between the 180° pulses in the CPMG block to an extreme where there is no delay window. We have recently introduced this windowless approach of CPMG as Extreme-CPMG (E-CPMG) on the backbone amide ^{15}N nuclei of the protein gpW to study its fast folding with 6.4 kHz maximum refocusing frequency (Reddy et al., 2018). In different chapters of this thesis, E-CPMG is performed on all of the three commonly used

nuclei in bio-molecular NMR (^{15}N , ^{13}C and ^1H) and the benefits are explained in the corresponding chapter.

1.5 The Current State of our Art: Thesis Outline

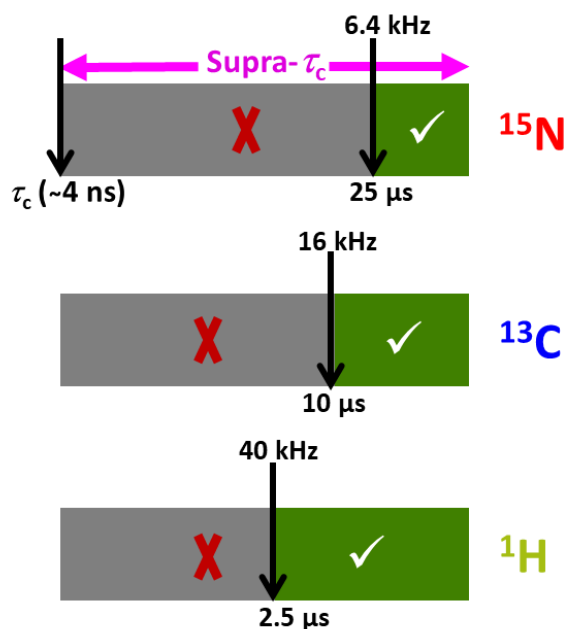


Figure 1.3: The gradual progress of high power RD experiments and narrowing of the unobservable timescale window. The supra- τ_c window of the dynamics timescale spectrum (figure 1.1) is shown, where the green areas indicate the timescale window that is already made detectable by high power RD and the gray regions are still undetectable. Narrowing of the undetectable window is evident at nuclei with higher gyromagnetic ratio (γ), due to higher available B_1 field.

From figure 1.2 it can be seen that NMR offers several relaxation based method to characterize motion in every timescale from picoseconds to seconds. The window between the rotational correlation time of standard size protein (~ 4 ns; ~ 8 kDa) and $40 \mu\text{s}$ is termed as the supra- τ_c window. Over the years an increasing number of experimental evidence are being accumulated where conformational sampling occurring in the supra- τ_c window has been demonstrated to play a crucial role for bimolecular function (Ban et al., 2011; Lange et al., 2008; Zhang, Stelzer, Fisher, & Al-Hashimi, 2007). For example, a direct connection between the internal motion of ubiquitin and its binding affinity to other proteins is proven both experimentally and from molecular dynamics simulations (Michielssens et al., 2014;

Smith et al., 2016). The only method that can hint at the existence of motion in this window is RDC (Lange et al., 2008). Although RDC can tell the presence of elevated dynamics in the supra- τ_c window, it was not possible to ascertain the kinetics, which is possible by measuring relaxation dispersion (RD) experiments. In spite of the wide range of applicability of RD until very recently it could not study motions with timescales faster than 40 μ s because of technical limitations. To detect a motion in $R_{1\rho}$ RD, spin-locks with B_1 -fields comparable to the frequency (inverse of lifetime) of the motion is necessary. Whereas for CPMG RD, the frequency of motion should match with the repetition frequency of the 180° pulses. This brought the limitation to RD method. Until recently in ^{15}N the maximum achievable B_1 field was only 1 kHz, making detection of motion faster than 40 μ s impossible. Combining the development in the hardware of probes and amplifiers with more significant design of acquisition scheme for better heat dissipation, we could apply 6.5 kHz of B_1 field in both $R_{1\rho}$ (Ban et al., 2012) and E-CPMG (Reddy et al., 2018). This enabled us to detect motion as fast as 25 μ s. For achieving higher B_1 field with less input power, we gradually moved to nuclei with higher gyromagnetic ratio. On the ^{13}C and ^1H channel, we could achieve 16 kHz and 40 kHz B_1 field, respectively with much less applied power than in ^{15}N nuclei. With this development, we could extend the RD-detectable window to single-digit microsecond for both $R_{1\rho}$ and CPMG. In this thesis, the newly developed high power RD technique is applied to several folded and intrinsically disordered proteins where we found hidden functional motions that helped in understanding molecular recognition and folding events. In the conclusion and outlook section of this thesis, I have briefly mentioned about our ongoing effort to make the entire supra- τ_c detectable by performing RD experiments in nonconventional NMR probes.

2 Antibody Recognition is Linked with Conformational Exchange in Protein GB3

2.1 Introduction

As described in the previous chapter, molecular recognition events greatly rely on spatial and temporal changes of enzyme conformations (Ban, Sabo, et al., 2013; A. G. Palmer, 3rd, 2004; A. G. Palmer, 3rd & Massi, 2006). Over the years an increasing number of experimental evidences are being accumulated where conformational sampling occurring in the supra- τ_c window (from molecular tumbling time; τ_c - 40 μ s) has been demonstrated to play a crucial role for bimolecular function (Ban et al., 2011; Lange et al., 2008; Zhang et al., 2007). For example, a direct connection between the internal motion of ubiquitin and its binding affinity to other proteins is proven both experimentally and from molecular dynamics simulations (Michielssens et al., 2014; Smith et al., 2016). In this chapter, I have described the link between supra- τ_c dynamics and antibody recognition of the third immunoglobulin (IgG) binding domain of protein G (GB3). Being a part of protein G, GB3 plays an important role in antibody binding and immunoprecipitation (Derrick & Wigley, 1994). Because of its long-term stability at higher concentration, GB3 is routinely being investigated by NMR from both structural and kinetic aspect for several decades. A series of previous investigations from residual dipolar coupling (RDC) and exact NOE (eNOE) measurement have indicated the presence of supra- τ_c dynamics in the loop region between the first and second β -strand of GB3 (Sabo et al., 2014; Vogeli, Kazemi, Guntert, & Riek, 2012; Yao, Vogeli, Torchia, & Bax, 2008). Although these studies could hint at the presence of elevated dynamics in the loop, it was not possible to ascertain the kinetics, which is possible by measuring relaxation dispersion (RD). In spite of the wide range applicability of RD until very recently it could not study motions with timescales faster than 40 μ s, because of technical limitations. Here we have applied high-power rotating

frame relaxation ($R_{1\rho}$) dispersion to capture the so far undetected supra- τ_c motion in the protein GB3.

2.2 Results and Discussion

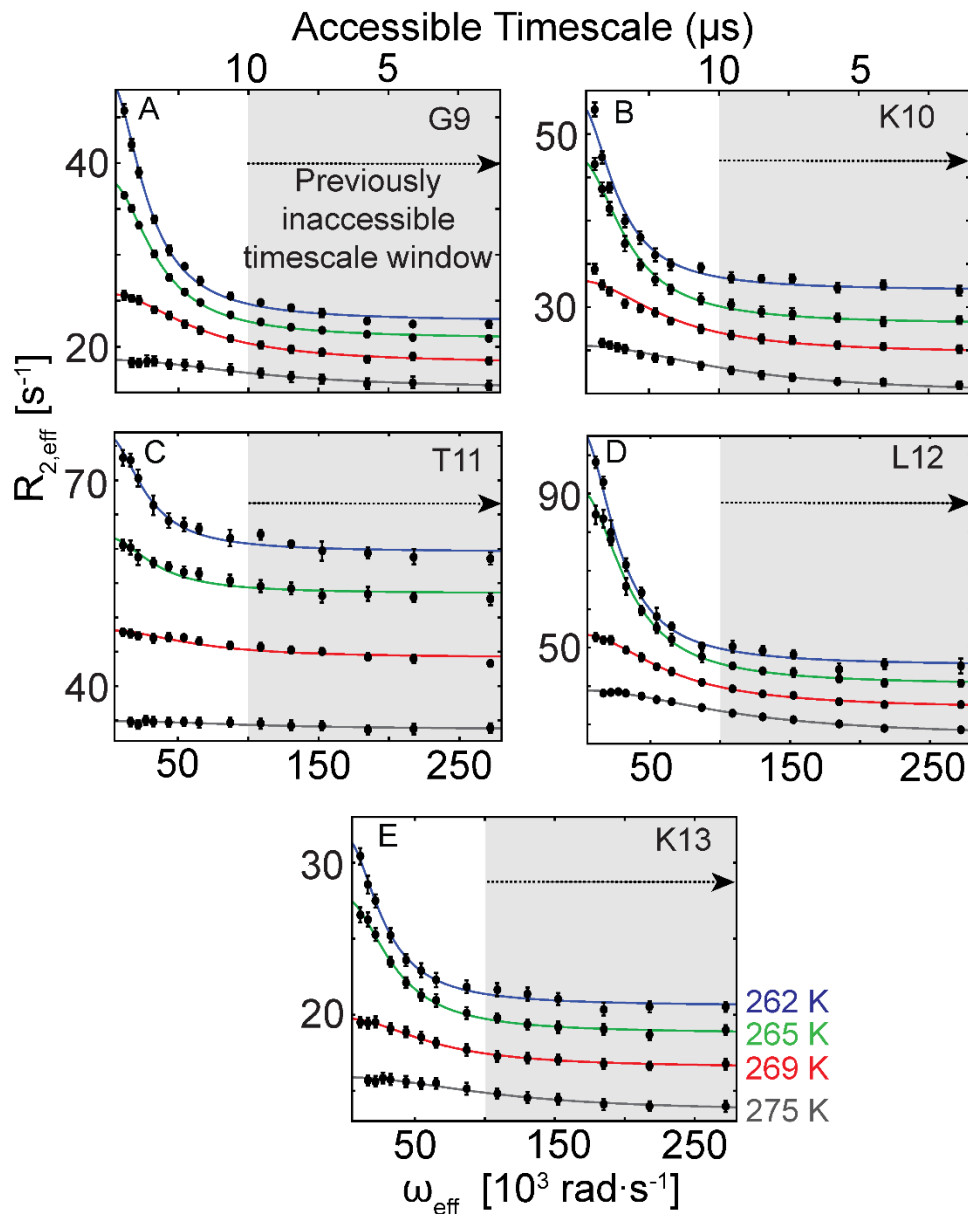


Figure 2.1: **Relaxation dispersion (RD) found in GB3 for the first time by high power $R_{1\rho}$.** Previously undetected loop dynamics are measured at four different temperatures. At each temperature, the global fitting of RD profiles to a single lifetime is shown with curves of gray, red, green and blue color at 275, 269, 265 and 262 K respectively. The shaded area in each plot indicates the previously inaccessible timescale window, which was made detectable by use of higher spin-lock power in the $R_{1\rho}$ measurements.

As discussed in the previous chapter, presently we can safely apply high RF power, which is sufficient to characterize dynamics with single digit microsecond lifetime (Pratihari et al., 2016). To probe the loop dynamics of GB3, for the first time we have combined this high power ^1H $R_{1\rho}$ relaxation dispersion method with supercooled water.

High power RD was first applied to the backbone amide nitrogen nuclei at 275 K temperature through on-resonance $R_{1\rho}$ relaxation dispersion measurements, where a maximum 6 kHz of RF power could be applied. This study did not show any measurable exchange contribution to relaxation which led to flat dispersion profiles for all observed residues. This suggested either the chemical shift variance (CSV) of amide ^{15}N for the conformational ensemble is too small to be detected by RD or the timescale of interconversion between the conformers is too fast ($< 25 \mu\text{s}$) to be captured with 6 kHz RF power. For achieving higher B_1 field with less input power, we moved to a nucleus with higher gyromagnetic ratio. On the ^1H channel, we could achieve 25 kHz B_1 field with twelve times less applied power than in ^{15}N nuclei. This increase in achievable RF power extended the detectable timescale window by an order of magnitude. In the off-resonance ^1H $R_{1\rho}$ experiment, maximum effective B_1 field of 272,000 rad s^{-1} can now detect dynamics as fast as 3.7 μs . This high power off-resonance ^1H $R_{1\rho}$ was then applied to backbone amide protons of GB3 protein at 275 K on a perdeuterated sample to reduce pseudo-dispersion effects caused by cross-relaxation (Eichmüller & Skrynnikov, 2005). Use of perdeuteration also decreases the transverse relaxation rates of backbone amide protons, which makes detection of small exchange contribution to relaxation much easier.

In total five residues showed relaxation dispersion in this measurement. The RD profiles are shown in figure 2.1 for residues G9 (A), K10 (B), T11 (C), L12 (D) and K13 (E). All five RD profiles at 275 K could be fitted to a single global timescale of $9.1 \pm 0.4 \mu\text{s}$ with equation 2.2, which is explained in the materials and methods section of this chapter. The global fitting at 275 K is shown as a gray curve in figure 2.1. The detection of such fast motion was possible only because we could achieve such a high spinlock field in ^1H nuclei. Interestingly these five residues appear in the same stretch (9-13) and are located in the first loop between the first and second β strand of GB3 (figure 2.2 (A)). To get the activation energy barrier for the detected motion by Arrhenius fitting we need to study the dynamics at other temperatures.

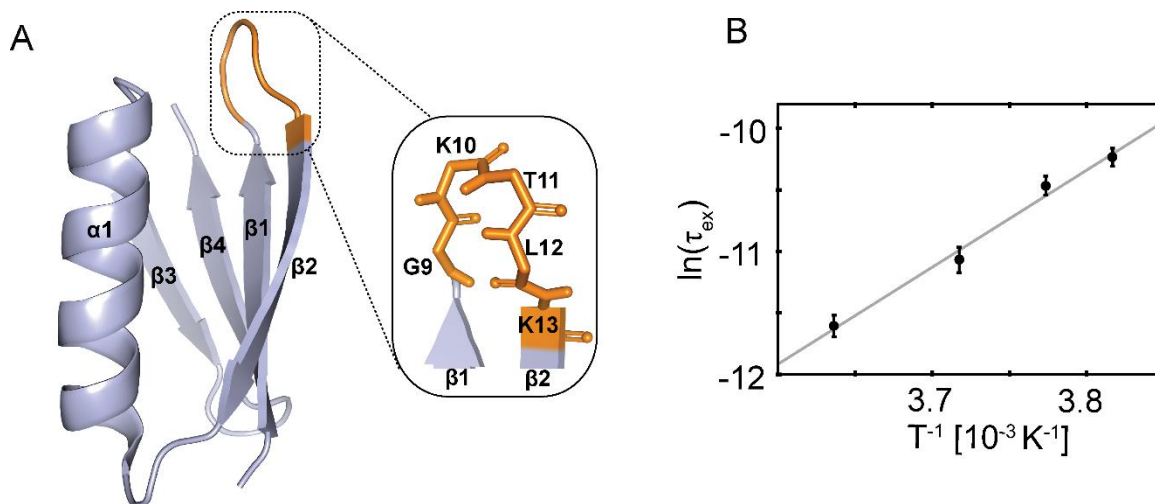


Figure 2.2: Spatial and temporal distribution of the observed supra- τ_c motion in GB3.

(A) The residues showing supra- τ_c dynamics are shown in orange in the RDC refined crystal structure of GB3 (PDB ID: 2OED). (B) Natural logarithm of the global motion obtained from RD measurements is plotted against the inverse of temperature ($1/T$) for Arrhenius analysis. From the fitting of this data to the Arrhenius model (equation 2.3), the activation energy was found to be $65.6 \pm 4.7 \text{ kJ mol}^{-1}$.

Since the timescale of the detected loop dynamics is already at the faster edge of the detection limit, at higher temperatures the loop motion will be much faster and go beyond the detection limit. Hence the only way to study the temperature dependence of the motion was to go down in temperature from 275 K (2°C), which is very close to freezing temperature of water. To stop the sample from freezing, we have used 1 mm capillaries (details are in materials and method of this chapter) for the measurements of dynamics at lower temperature (Mills & Szyperski, 2002; Swenson, Jansson, & Bergman, 2006). In this experimental design, we could reach temperatures as low as 262 K (-11°C) where the sample could still be kept in liquid state. The loop dynamics was measured at three additional lower temperatures where only the same stretch of five residues showed relaxation dispersion as shown in figure 2.1. Like at 275 K, at each temperature all five residues could be fitted to a single global timescale of 15.5 ± 0.8 , 28.5 ± 1.1 and $35.9 \pm 1.3 \mu\text{s}$ at 269, 265 and 262 K respectively. All fitted parameters from global and individual fitting are shown in table 2.1. These temperature dependent lifetimes were then fitted to a Arrhenius-type equation to obtain the activation energy barrier for the loop motion.

Table 2.1: Exchange lifetimes (τ_{ex}), chemical shift variance (Φ_{ex}) and intrinsic transverse relaxation rates ($R_{2,0}$), obtained from fitting the relaxation dispersion curves in figure 2.1 is shown here for both global and individual fitting. The fitting was done with equation 2.2 as explained in the material and methods section of this chapter.

T [K]	residue	G9	K10	T11	L12	K13
262	τ_{ex} [μs]	35.9 ± 1.3				
	Φ_{ex} [$10^3 \text{ rad}^2 \cdot \text{s}^{-2}$]	735 ± 18	603 ± 17	472 ± 23	1706 ± 63	309 ± 12
	$R_{2,0}$ [s^{-1}]	22.7 ± 0.2	31.9 ± 0.2	59.6 ± 0.2	42.3 ± 0.5	20.6 ± 0.1
265	τ_{ex} [μs]	28.5 ± 1.1				
	Φ_{ex} [$10^3 \text{ rad}^2 \cdot \text{s}^{-2}$]	605 ± 17	670 ± 24	287 ± 22	1770 ± 49	310 ± 12
	$R_{2,0}$ [s^{-1}]	20.9 ± 0.1	28.0 ± 0.2	53.5 ± 0.2	40.3 ± 0.3	18.8 ± 0.1
269	τ_{ex} [μs]	15.6 ± 0.8				
	Φ_{ex} [$10^3 \text{ rad}^2 \cdot \text{s}^{-2}$]	488 ± 28	542 ± 29	258 ± 23	1238 ± 64	209 ± 16
	$R_{2,0}$ [s^{-1}]	18.1 ± 0.2	24.6 ± 0.2	44.1 ± 0.2	34.1 ± 0.4	16.5 ± 0.2
275	τ_{ex} [μs]	9.0 ± 0.4				
	Φ_{ex} [$10^3 \text{ rad}^2 \cdot \text{s}^{-2}$]	357 ± 45	625 ± 52	139 ± 55	1342 ± 97	255 ± 32
	$R_{2,0}$ [s^{-1}]	15.4 ± 0.3	19.9 ± 0.2	33.7 ± 0.4	26.9 ± 0.4	13.6 ± 0.2

T [K]	residue	G9	K10	T11	L12	K13
262	τ_{ex} [μs]	34.3 ± 1.2	48.9 ± 3.5	31.2 ± 3.1	35.4 ± 1.6	36.4 ± 2.3
	Φ_{ex} [$10^3 \text{ rad}^2 \cdot \text{s}^{-2}$]	756 ± 15	521 ± 15	517 ± 43	1720 ± 66	307 ± 14
	$R_{2,0}$ [s^{-1}]	22.6 ± 0.1	32.6 ± 0.2	59.3 ± 0.3	45.2 ± 0.5	20.6 ± 0.1
265	τ_{ex} [μs]	27.8 ± 0.7	33.9 ± 2.1	16.9 ± 3.1	28.3 ± 1.3	27.7 ± 1.7
	Φ_{ex} [$10^3 \text{ rad}^2 \cdot \text{s}^{-2}$]	616 ± 14	598 ± 26	460 ± 92	1780 ± 54	317 ± 14
	$R_{2,0}$ [s^{-1}]	20.8 ± 0.1	28.5 ± 0.2	52.6 ± 0.5	40.2 ± 0.4	18.7 ± 0.1
269	τ_{ex} [μs]	15.7 ± 1.2	21.4 ± 2.1	6.8 ± 1.6	15.3 ± 1.0	14.1 ± 1.8
	Φ_{ex} [$10^3 \text{ rad}^2 \cdot \text{s}^{-2}$]	484 ± 39	405 ± 35	784 ± 224	1263 ± 89	233 ± 35
	$R_{2,0}$ [s^{-1}]	18.2 ± 0.2	25.3 ± 0.2	42.2 ± 0.7	34.0 ± 0.4	16.4 ± 0.2
275	τ_{ex} [μs]	7.6 ± 2.1	12.5 ± 1.9	5.3 ± 10.6	8.7 ± 0.4	7.5 ± 1.8
	Φ_{ex} [$10^3 \text{ rad}^2 \cdot \text{s}^{-2}$]	451 ± 152	422 ± 72	328 ± 166	1404 ± 107	327 ± 112
	$R_{2,0}$ [s^{-1}]	15.1 ± 0.6	20.7 ± 0.3	33.1 ± 0.7	26.7 ± 0.4	13.4 ± 0.4

Although with high power RD we are measuring conformational exchange of a continuum of states, here we are assuming that all interconversions occur with same activation energy barrier and attempt frequency. The activation energy was found to be $65.6 \pm 4.7 \text{ kJ mol}^{-1}$ and the extrapolated exchange timescale at the physiological temperature of 310 K was $371 \pm 115 \text{ ns}$. The high amount of uncertainty in the extrapolated timescale is coming from

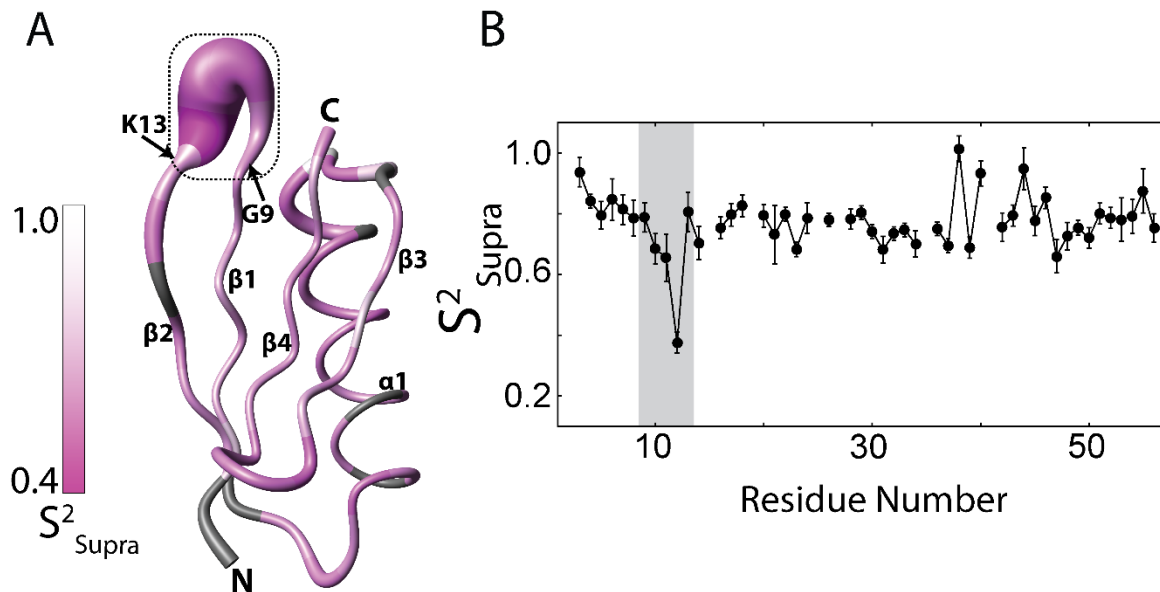


Figure 2.3: Elevated Supra- τ_c dynamics found in GB3 from RDC ensemble. Previously measured RDC data sets (Yao et al., 2008) were used to generate the ERMD (Ensemble-Restrained-Molecular-Dynamics) ensemble containing 640 members. (A) The ensemble is represented as tube, where the mean positions of backbone C α atoms represent the axis of the tube and the square fluctuations of the C α atoms are shown as the radius of the tube. The additional amount of supra- τ_c mobility in addition to the Lipari-Sabo model ($S_{supra}^2 = S_{RDC}^2/S_{LS}^2$) is represented by the intensity of magenta color in the tube surface. (B) S_{supra}^2 values are plotted along the sequence of GB3. The residues that shown relaxation dispersion are represented by boxed region in (A) and shaded area in (B).

the narrow range of temperature (262-275 K) where the exchange process was detectable. The lifetime at the physiological temperature is still far from being in the RD detectable window and could be accessed only by studying the motion at several supercooled conditions and subsequent extrapolation.

Although RDC cannot provide details about the timescale of motion, it is sensitive to bond vector fluctuations occurring in a wide range of timescale (ps-ms), which includes the supra- τ_c window (Ban, Sabo, et al., 2013; Fenwick et al., 2011; Lange et al., 2008; Sabo et al., 2014). Since Lipari-Sabo order parameters (S_{LS}^2) gives information about sub- τ_c motion (faster than τ_c), supra- τ_c order parameter (S_{supra}^2), calculated by normalizing RDC derived order parameters (S_{RDC}^2) with S_{LS}^2 , will emphasize the additional amount mobility in the supra- τ_c window. S_{supra}^2 , calculated from previously reported S_{RDC}^2 (Sabo et al., 2014) and

S_{LS}^2 (Hall & Fushman, 2003) of GB3, is plotted in figure 2.3(B) along the sequence. It is evident from the plot that among all residues, the first β -turn region of GB3 shows elevated supra- τ_c mobility with L12 being the most dynamic one. The shaded region in the plot indicates the residues that showed relaxation dispersion in backbone amide proton $R_{1\rho}$ relaxation dispersion measurements at various temperatures, and they coincide with the residues with highest supra- τ_c mobility indicated by lower S_{supra}^2 values. The ERMD (Ensemble-Restrained-Molecular-Dynamics) ensemble containing 640 members, calculated from previously published RDC data sets (Yao et al., 2008) is shown in figure 2.3 (A) in tube fashion. The axis of the tube indicates the mean backbone $C\alpha$ position of all 640 members and the square fluctuations of the $C\alpha$ atoms from their mean position is represented by the thickness of the tube. The boxed region of the protein denotes the stretch of residues with RD detectable conformational exchange. The tube is colored with magenta according to the supra- τ_c order parameters of each residue. Lower values of S_{supra}^2 are

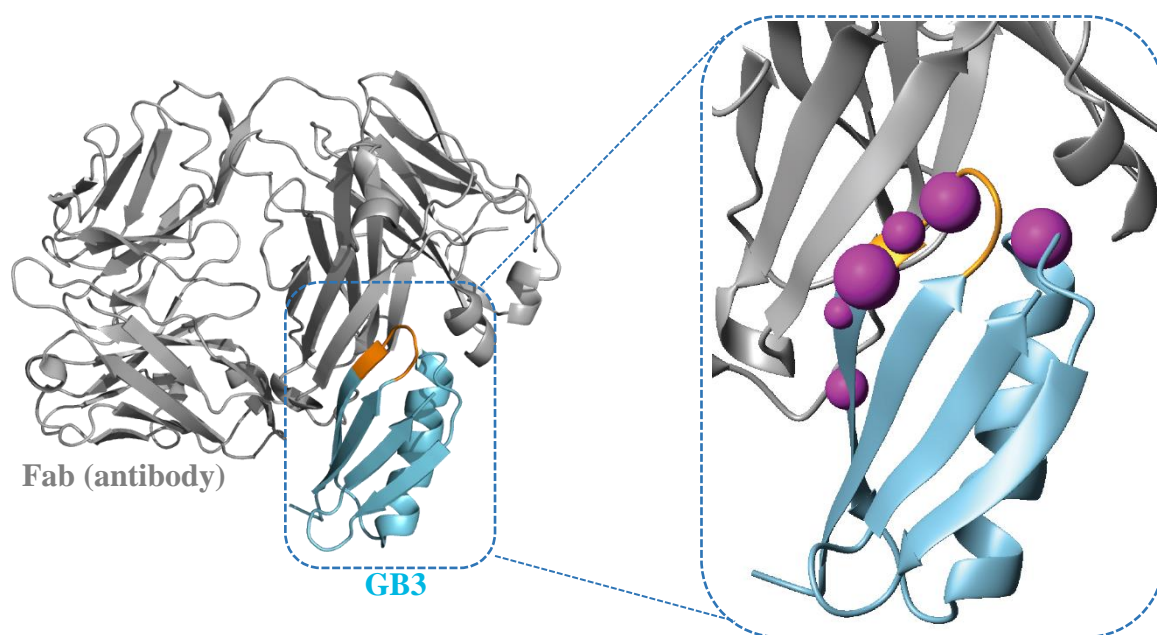


Figure 2.4: Antibody recognition in linked with supra- τ_c loop motion. Crystal structure of GB3 in complex with a Fab fragment (MOPC21) is shown (PDB id: 1IGC), where GB3 is presented in blue and the Fab fragment is shown in gray. The residues showing relaxation dispersion are colored in orange. Selected portion of the complex is enlarged to show the binding region of GB3. The radius of magenta spheres represents the number of contacts (within 5 Å) of the binding partner to GB3 backbone amide protons.

indicated by a more intense color. From both color intensity and the tube thickness, it is evident that the same region of GB3 displays lower supra- τ_c order parameters and higher fluctuation of the ensemble members. This region again coincides with residues where relaxation dispersion was observed as indicated by the dotted box in figure 2.3 (A). GB3 is known to play an important role in antibody (immunoglobulin) binding of protein G. Through the GB3 domain protein G binds to several antibodies (Bjorck & Kronvall, 1984), one of which is presented in figure 2.4. The crystal structure of the Fragment antigen-binding (Fab) region of MOPC21 antibody in complex with GB3 is shown (PDB ID: 1IGC), where Fab is presented in gray and GB3 is shown in blue. The structure of the whole complex is enlarged to highlight the part of GB3 that takes part in binding. The residues where exchange contributions to relaxation was detected are colored in orange. The number of contacts within 5 Å of every backbone amide proton of GB3 to the antibody fragment was calculated, which is represented by the radius of magenta spheres in figure 2.4. From this contact map it is evident that mainly two regions of GB3 are involved in recognizing the Fab antibody fragment; the first β -turn region which extends further to the following

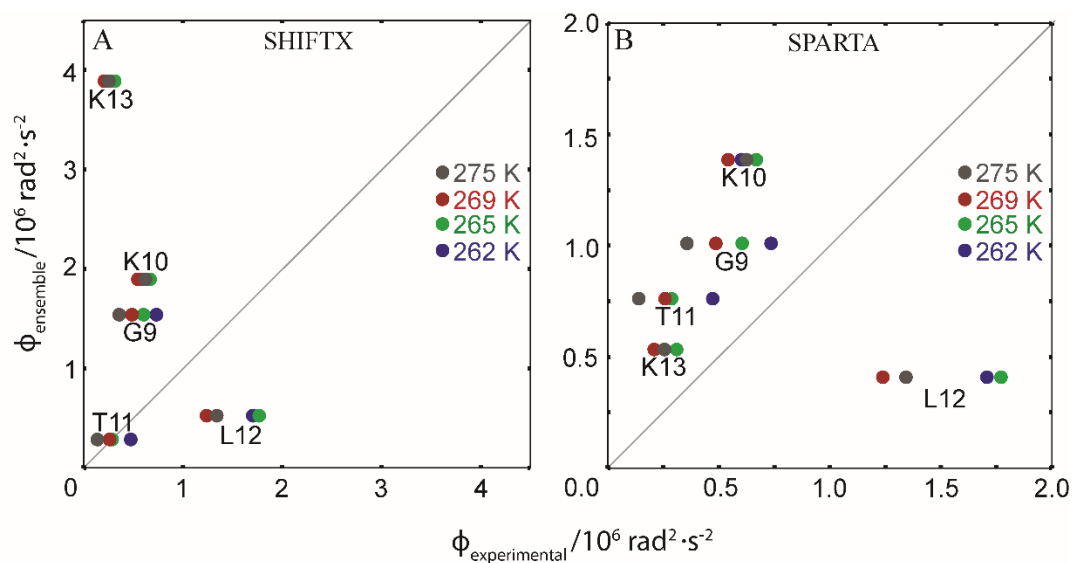


Figure 2.5: Comparison of experimental and predicted chemical shift variance (CSV). CSV variance of the 640-membered ERMD ensemble was calculated after chemical shift prediction of the ensemble members with both SHIFTX and SPARTA. The correlation plot of experimental and predicted CSV are made at 262 K (purple), 265 K (green), 269 K (red) and 275 K (gray).

β -strand, and the C-terminal part of the α -helix. Interestingly, in five residues from this β -turn region relaxation dispersion was detected. We did not observe any detectable RD from the C-terminus of the α -helix. This could be due to the lower value of weighted chemical shift variance or this segment of GB3 could be moving at a faster lifetime, which is still beyond the detection limit ($\sim 4 \mu\text{s}$) of RD. Chemical shift variance (CSV) of both amide ^1H and ^{15}N nuclei were calculated for the 640-membered ERMD ensemble using an N-site jump model (Ban et al., 2011). Both SHIFTX (Neal, Nip, Zhang, & Wishart, 2003) and SPARTA (Shen & Bax, 2007) were used for chemical shift prediction. Since the first loop of GB3 moves with a timescale, which is impossible to detect with the applicable RF power in ^{15}N nuclei, experimental CSV was not available for comparison. Figure 2.5 shows the comparison of backbone amide proton experimental and predicted CSVs. For the CSV calculated with SHIFTX no correlation was observed (figure 2.5 (A)). For the predicted CSV calculated from chemical shifts from SPARTA the relative sizes match with experimentally obtained CSVs except for L12. The amide proton of L12 shows a large CSV in the RD measurement, which could be due to the formation and breaking of hydrogen bonds with G9 carbonyl oxygen. Inaccuracy in the chemical shift prediction of hydrogen-bonded protons (Fu, Case, & Baum, 2015) could lead to lower predicted CSV of L12 at all four temperatures. After removing L12 correlation coefficients of 0.74, 0.91, 0.94 and 0.88 were obtained at 262 K, 265 K, 269 K and 275 K, respectively.

2.3 Conclusion

By using high power spin-lock in off-resonance amide proton $R_{1\rho}$ relaxation dispersion measurements we could extend the RD-detectable window to single-digit microsecond. Using this high power RD we found supra- τ_c motion in a stretch five residues belonging to the first loop region of GB3. From the ERMD ensemble, calculated from previously measured RDC, we found elevated fluctuations in this loop compared to the rest of the protein. By calculating supra- τ_c order parameter by scaling RDC order parameters with S_{LS}^2 , enhanced supra- τ_c mobility could be detected in the same region. By combining the high power RD with the supercooled technique, we could study the loop motion at several temperatures. The Arrhenius fitting of the global timescale at different temperature shows that the activation energy barrier for the loop motion in GB3 is $65.6 \pm 4.7 \text{ kJ mol}^{-1}$. Interestingly, this energy barrier is even higher than what is found for the peptide-flip

motion ($48.4 \pm 0.5 \text{ kJ mol}^{-1}$) in ubiquitin that originates through rearrangement of hydrogen bonds (chapter 4). This suggests that the loop motion in GB3 may also involve similar high-energy processes. Indeed during the interconversion of ERMD ensemble members of GB3, we could observe formation and breaking of hydrogen bond between amide proton of L12 and carbonyl oxygen of G9. The observed loop motion was extrapolated to be $371 \pm 115 \text{ ns}$ at physiological temperature, which is still far away from recently extended detectable timescale window. Interestingly, the newly observed supra- τ_c motion takes place in a region, which binds to antibodies. This hints to a link of the observed motion with the antibody recognition of GB3. We believe that in future this combination of high power RD and supercooled conditions together with RDC will be able to find functional supra- τ_c dynamics in many more biomolecules, which will help to understand their functions.

2.4 Materials and Methods

2.4.1 Sample Preparation

For the high power backbone amide $^1\text{H } R_{1\rho}$ measurements, ^{15}N -labeled perdeuterated GB3 protein was expressed in *Escherichia coli*, which were adapted to a 100% D_2O Toronto minimal medium supplemented with D_7 -glucose as a the carbon source and $^{15}\text{N-NH}_4\text{Cl}$ as the nitrogen source. The protein sample was then purified as described before (Gronenborn et al., 1991). NMR measurements were performed on a 2.8 mM protein sample in a 50 mM sodium phosphate buffer of pH 6.5 containing 100 mM NaCl and 0.05 % sodium azide. 10% D_2O was added before the NMR measurements. All RD experiments at different temperatures ranging from 262 to 275 K were carried out in capillaries of 1 mm diameter to achieve supercooled conditions. 25 μl of GB3 sample was transferred to each capillary (Wilmad, Buena, New Jersey) using a Hamilton syringe. Twelve such capillaries were then placed in a standard 5 mm NMR tube, which was used for all measurements described in this chapter.

2.4.2 NMR Experiments

All NMR measurements were performed in a Bruker Avance III spectrometer operating at ^1H Larmor Frequency of 600 MHz (14.1 T). Backbone amide proton $R_{1\rho}$ measurements were performed at 262 K, 265 K, 269 K and 275 K. For reaching the supercooled conditions, the sample temperature was lowered slowly (0.5 K / min) to avoid freezing of

the liquid sample. A high VT gas flow of 1070 liter/hour was used for achieving better dissipation of heat generated by high power RF pulses. Heavy ceramic spinner (sample holder) was necessary to avoid wobbling of the sample by the high gas flow rate.

Each two dimensional plane corresponding to a particular spin-lock power and delay was recorded with 64 complex points in the indirect dimension ($t_{1,\max} = 31$ ms) and 512 complex points in the direct dimension ($t_{2,\max} = 65.5$ ms); 4 scans were performed for each FID. The recycle delay (d_1) was set to 3 seconds for better heat dissipation and to protect the integrity of the probe and amplifiers. The pulse program for off-resonance $R_{1\rho}$ measurement was written following the work published previously (Eichmuller & Skrynnikov, 2005) and provided in the appendix. The spin-lock power was varied between 1 kHz and 25 kHz during the measurement to obtain effective transverse relaxation rates at different RF field. The average tilt angle was kept at 35.3° ($\tan^{-1}[1/\sqrt{2}]$) to minimize the pseudo-dispersion effects caused by NOE and ROE transfers. This was achieved by choosing proper spin-lock carrier offset relative to the center of amide region (8 ppm). The off-resonance approach helped us to achieve higher maximum effective RF field of 272,000 rad/s, which can detect single digit microsecond motion (3.4 μ s). All the spins under investigation were aligned with the off-resonance spin-lock field by applying adiabatic RF pulse of 100 kHz sweep width phase and amplitude modulation. Effective transverse relaxation rates at each spin-lock power was measures by varying the spin-lock delay from 2 ms to 125 ms. To achieve homogeneous heat distribution all measurements were performed in interleaved fashion.

2.4.3 Data Analysis

The scan interleaved RD data was divided and then co-added using a home-built pearl script to generate multiple .ser files corresponding to every spin-lock power and delay. The raw data was then processed with NMRpipe (Delaglio et al., 1995) software. All processed 2D planes were loaded to Computer-Aided Resonance Assignment (CARA) as .ft2 format and the intensities were extracted with a peak tolerance of 10% in both dimensions to take care of minor peak shifts. At every spin-lock power $R_{1\rho}$ values were obtained by fitting the peak intensities from spectra corresponding to spin-lock delay of 2, 45, 90 and 125 ms with the following equation

$$I_t = I_0[\exp(-R_{1\rho}t)]. \quad 2.1$$

The uncertainties of fitted $R_{1\rho}$ values were obtained from residuals of the four fitted points. Effective $R_{1\rho}$ values and effective spin-lock power were then calculated following a previously described method (Eichmuller & Skrynnikov, 2005). RD profiles measured at all four temperatures were fitted to the following equation

$$\frac{R_{1\rho}}{\sin^2\theta} = R_{2,0} + \frac{\Phi_{ex}\tau_{ex}}{(1 + \tau_{ex}^2 \omega_{eff}^2)}. \quad 2.2$$

Where θ is the tilt angle of every spins appearing at a particular resonance frequency, Φ_{ex} is the population weighted chemical shift variance, τ_{ex} is the lifetime of exchange process and ω_{eff} is the effective spin-lock field. The fitting was done using the NMinimize function in Mathematica software. Uncertainties of the fitted parameters were obtained by Monte Carlo method with 500 runs. R_2 and Φ_{ex} values were local to each residues even when all residues were fitted to a single global lifetime value at a particular temperature. The lifetimes τ_{ex} obtained from the above mentioned procedure were used for the Arrhenius fitting with the following equation

$$\ln(\tau_{ex}) = -\ln(A) + \left(\frac{E_a}{R}\right) \left(\frac{1}{T}\right). \quad 2.3$$

Where A is attempt frequency, E_a is activation energy and R is the universal gas constant.

3 Common Origin of Backbone and Side-chain dynamics Found with ^{13}C E-CPMG

3.1 Introduction

3.1.1 Side-chains: Powerful Probes for Structure and Dynamics

NMR has developed into a very powerful tool for studying functional dynamics of biomolecules with atomic resolution at near physiological conditions. In the previous chapter, we have linked a newly found backbone dynamics in the protein GB3 with its antibody recognition events. Although motions occurring in both backbone and side-chains of proteins are proven to play an important role in binding and folding events (Pratihari et al., 2016; Reddy et al., 2018; Smith et al., 2016), in high molecular weight proteins and their complexes, it is difficult to observe backbone resonances due to their fast transverse relaxation rates. In such challenging situations, methyl groups in the side-chains of amino acids act as prominent probes for investigation of both structure and dynamics (Tugarinov, Hwang, Ollerenshaw, & Kay, 2003) of large molecules. Due to their high abundance and excellent relaxation properties, methyl groups are gaining significance, especially while measuring large complexes at very high magnetic fields (Schutz & Sprangers, 2020).

3.1.2 Hierarchy of Motion in Side-chains from $R_{1\rho}$ RD

Fast local fluctuations are known to be linked to relatively slower functional domain motions, forming a hierarchy in the timescale of motions in enzymes, which is necessary for their function (Hammes-Schiffer & Benkovic, 2006; Henzler-Wildman et al., 2007). Methyl containing side-chains display motions in both the sub- τ_c (ns-ps) and the supra- τ_c (ms- μ s) window in previously published work (Fares et al., 2009; Tzeng & Kalodimos, 2012). A clear understanding of the interplay of side-chain motions with different

timescales was obtained from $R_{1\rho}$ -based relaxation dispersion measurements performed on side-chain methyl groups (Smith et al., 2015). It was demonstrated that ubiquitin displays microsecond motion by shuffling the populations of their side-chain rotamers, which interconvert on the ps-ns timescale. To know the activation energy of the observed side-chain motion and to know the timescale of side-chain motion at physiological temperature it was necessary to follow the dynamics at several temperatures. Additionally, to investigate the origin of the observed side-chain motion, it is necessary to perform relaxation dispersion experiments on several mutations, which are already proposed from a previous study of the backbone dynamics of ubiquitin (Smith et al., 2016).

3.1.3 Need for Speed: ^{13}C E-CPMG

In both Carr-Purcell-Meiboom-Gill (CPMG) and transverse rotating frame relaxation ($R_{1\rho}$) relaxation dispersion (RD) experiments, exchange contribution (R_{ex}) to effective transverse relaxation rates ($R_{2,\text{eff}}$) is quantified, which provide kinetic, thermodynamic and structural parameters of the motion under investigation (Ban et al., 2017; Neudecker et al., 2009; A. G. Palmer et al., 2001). In $R_{1\rho}$ based RD experiments, the additional exchange contribution is quenched by applying a spin-lock of variable radio frequency (RF) field strength. However, it is very difficult to precisely implement a spin-lock with weaker field strength (< 2 kHz) due to the higher spatial inhomogeneity of the B_1 field and nonlinearity of the amplifiers. In addition, at weaker RF field, R_1 contributes more to $R_{1\rho}$ than $R_{2,\text{eff}}$, particularly for the resonances appearing far from the RF carrier offset. The off-resonance residues displays more pseudo-dispersion effects on the RD profiles originating from dipole-dipole (DD) and chemical shift anisotropy cross-correlated-relaxation (CCR) (Reddy et al., 2018). These limitations demand $R_{1\rho}$ to be recorded at near on-resonance conditions that requires the measurement to be repeated at several narrow sampling offset for specific resonances. This needs prior knowledge about the residues, which are likely to undergo conformational exchange. On the other hand, CPMG based RD experiments are commonly used to obtain quenching of exchange contribution at lower refocusing frequencies (Ishima, 2012; Ishima & Torchia, 2003). This RD data is then combined with the $R_{2,\text{eff}}$ values, obtained with higher spin-lock fields in $R_{1\rho}$ to extract the kinetic parameters (Ban, Mazur, et al., 2013; Hansen et al., 2008). In addition to the necessity of setting up two different sets of experiments, this approach is disadvantageous due to dissimilar heating effects.

The entire applicable range of both conventional CPMG and $R_{1\rho}$ can be covered by slowly decreasing the inter-pulse delay between the 180° pulses in the CPMG block, to an extreme where there is no delay window. We have recently introduced this windowless approach of CPMG as Extreme-CPMG (E-CPMG) on the backbone amide ^{15}N nuclei of protein gpW to study its fast folding with 6.4 kHz maximum refocusing frequency (Reddy et al., 2018). In this chapter, we have extended the E-CPMG approach to ^{13}C nuclei to achieve higher B_1 field with lower applied power. ^{13}C E-CPMG was used to study the temperature dependence of the side-chain motion in ubiquitin. The side-chain dynamics were also studied in two different single point mutants of ubiquitin, which are known to quench the global breathing motion in ubiquitin originated by flipping of the peptide bond between D52 and G53 (Smith et al., 2016).

3.2 Results and Discussion

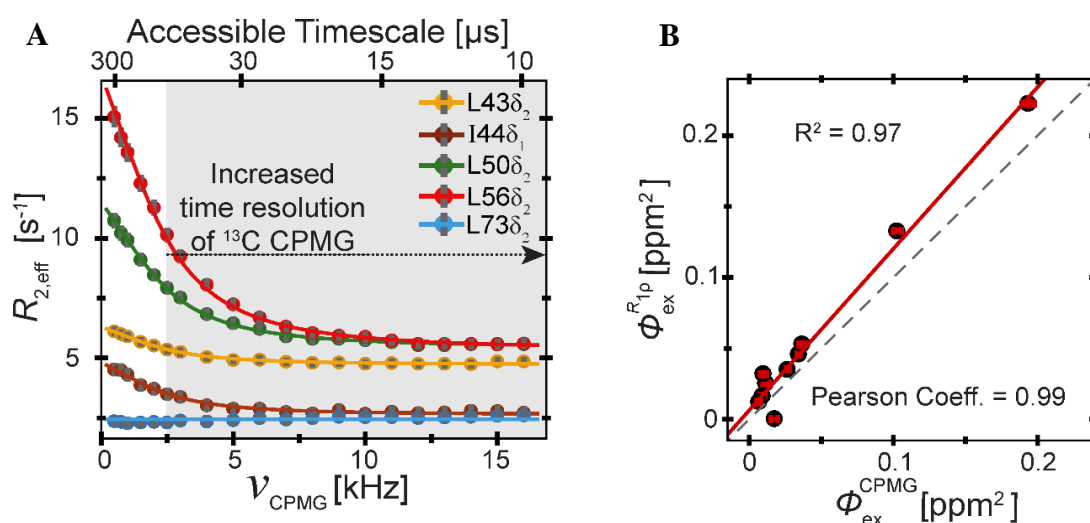


Figure 3.1: ^{13}C E-CPMG relaxation dispersion in side-chain of ubiquitin and comparison to $R_{1\rho}$. (A) Four out of ten dispersion profiles found at 277 K are shown in colored dots. A flat profile from the δ_2 methyl carbon of L73 is presented with gray dots. The shaded area indicates the previously inaccessible timescale window of conventional ^{13}C -CPMG. All RD profiles were fitted to a single global exchange rate of 15.11 ± 0.42 kHz. (B) Chemical shift variance (CSV) obtained from E-CPMG RD is compared with previously reported CSV from $R_{1\rho}$ measurements (Smith et al., 2015).

To compare with previously reported side-chain dynamics of ubiquitin from $R_{1\rho}$ measurements (Smith et al., 2015), ^{13}C E-CPMG experiments were first performed at 277 K on selectively $^{13}\text{CHD}_2$ -labeled ubiquitin. The use of a deuterated background and selective $^{13}\text{CHD}_2$ labeling of methyl groups in side-chains produced an AX spin system instead of AX_3 , which greatly reduced the complications involved in the ^{13}C CPMG measurements. Exchange contribution were detected in 10 out of 33 labeled methyl groups of ubiquitin at 277 K. Four of these RD profiles and a flat profile coming from methyl group of residue L73 are shown in figure 3.1. RD profiles were first fitted individually to the Luz-Meiboom model (Luz & Meiboom, 1963) as described by equation 3.4, which produced similar exchange rates at all methyl groups showing exchange contribution to relaxation (figure 3.2 A). All ten RD profiles were then subjected to a global fitting, which resulted in a single global exchange rate of 15.11 ± 0.42 kHz (66 ± 1.8 μs lifetime). This matches well with the reported exchange lifetime of 61 ± 1 μs from previous $R_{1\rho}$ measurements. Interestingly this timescale also matches closely with the global backbone dynamics observed previously in ubiquitin (55 μs) (Smith et al., 2015). This suggests that the side-chains also take part in the global breathing motion of ubiquitin, which is generated by a rearrangement of the hydrogen bonding network. In addition to the exchange frequency, the chemical shift variances obtained for the observed methyl groups also matches very well as seen from the correlation plot in figure 3.1 (B). A Pearson coefficient of 0.99 was obtained when the CPMG and the $R_{1\rho}$ derived amplitude of motion were compared. With the successful implementation of E-CPMG in ^{13}C nuclei, RD profiles of all 33 different methyl groups could be measured from a single set of experiments at the same ^{13}C carrier offset. Additionally, the detectable timescale window of conventional ^{13}C -CPMG is extended by a significant amount, which is represented by the shaded area in figure 3.1 (A). This was possible due to the availability of higher B_1 field in ^{13}C channel (16 kHz), which expanded the detectable window of E-CPMG that was previously implemented on ^{15}N nuclei, where maximum achievable refocusing was only 6 kHz. Good agreement between the global (green) and the individual (red) fitting in indicated by similar fitted chemical shift variance (CSV; Φ_{ex}) and intrinsic transverse relaxation ($R_{2,0}$) rates in figure 3.2. For both type of fitting (figure 3.2 (B)) it was observed that the δ_2 -methyl carbon of residue L50 shows the most significant exchange contribution (0.2 ppm²) among all 10

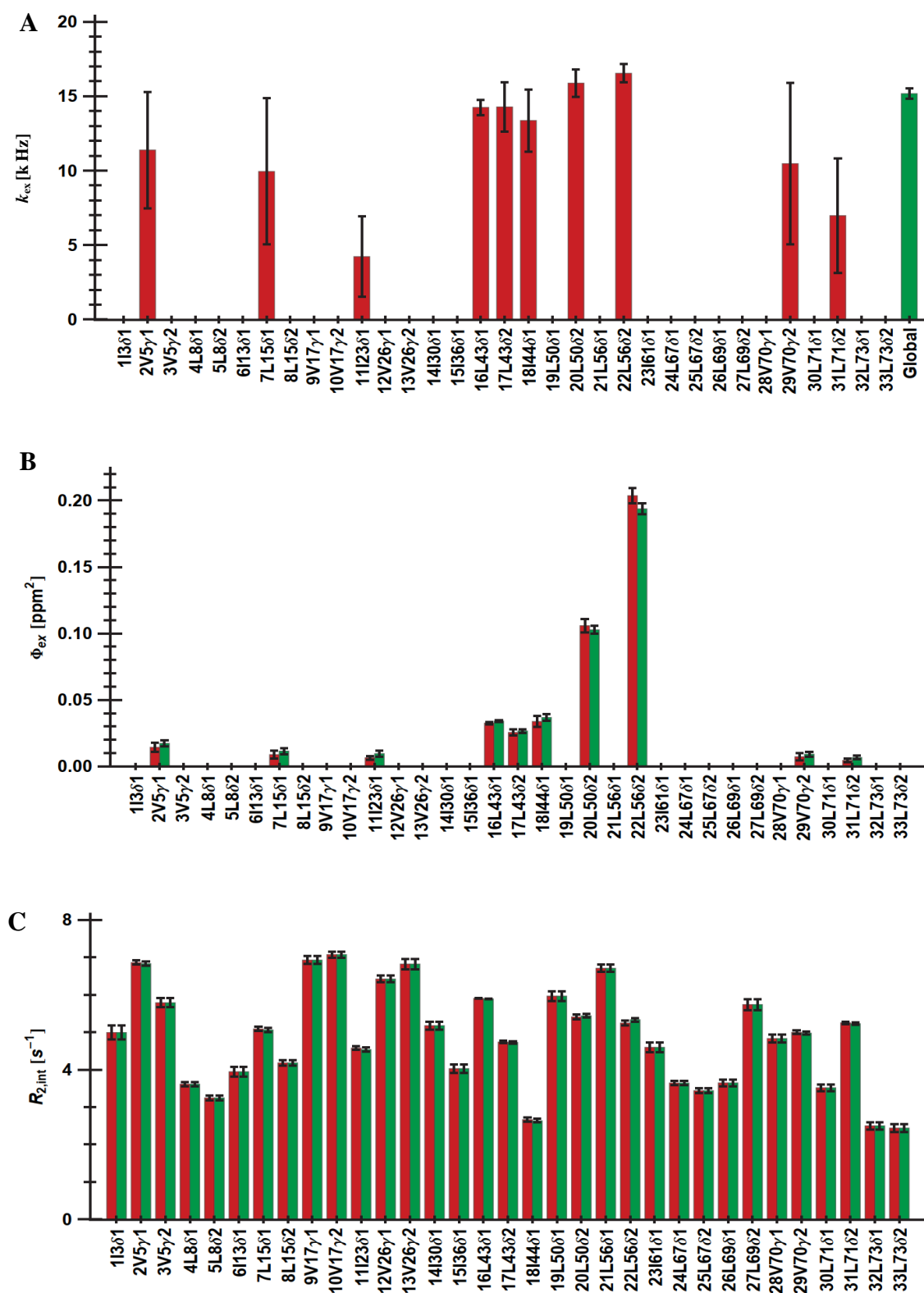


Figure 3.2: **Global and individual exchange parameters for ubiquitin side-chain motion at 277 K.** Both global and individual fitting parameters obtained by fitting relaxation dispersion profiles with the Luz-Meiboom model are plotted in green and red respectively.

methyl groups that showed dispersion. The obtained Φ_{ex} value is much smaller compared to what is expected in a two-state inter-rotamer model. This lower RD observed CSV was previously explained with a population shuffling model (Smith et al., 2015). According to this model the observed global μs motion, shuffle the populations of rotamers, which interconvert with a much faster timescale (ns-ps). This supports the presence of a hierarchy of timescales, where slowly interconverting macrostates are formed by rapidly exchanging microstates. For both L50 and L56, which show the most significant exchange contribution (fig 3.2(B)), RD was observed in one of the two δ methyl carbons. This too can be explained by a population alternation of either trans or gauche⁺ rotamers which are most abundant in crystal structure (Shapovalov & Dunbrack, 2011).

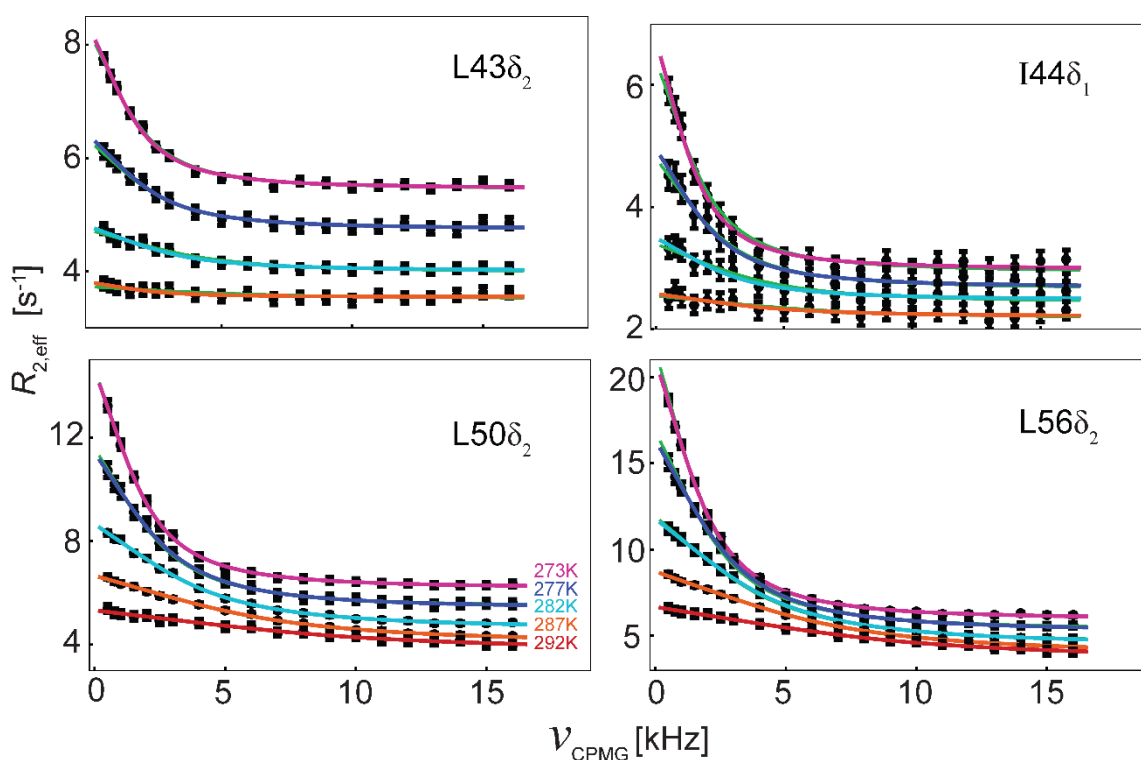


Figure 3.3: **Temperature dependence of side-chain motion in ubiquitin.** An exchange contribution could be detected at five different temperatures ranging between 273 to 292 K. RD profiles of four residues at these temperatures are shown in black dots. The global fitting of all RD profiles at a particular temperature to a single exchange rate is represented in colored lines and the color scheme is explained the plot of L50 δ_2 .

Since in the E-CPMG approach, RD profiles for all resonances can be measured with a single carrier offset, the observed side-chain motion could be studied at several temperatures using much less measurement time. In addition, the robustness of the E-CPMG approach for detecting slow and fast motions made it applicable in both low and high temperature. Although RD profiles were measured at six different temperatures from 273 to 298 K, no exchange contribution could be detected at 298 K. This is because the timescale of the motion at room temperature moves out of the detectable window of ^{13}C E-CPMG. Observation of this motion at room temperature by E-CPMG will be demonstrated in next chapter by applying even higher RF field in another nucleus (^1H) with much higher gyromagnetic ratio (γ). At each of the five temperatures, the RD profiles could be fitted to a single global exchange rate and the fitted rates were; 11.7 ± 0.3 , 15.1 ± 0.4 , 23.4 ± 0.5 , 36.9 ± 1.1 and 50.6 ± 5.7 kHz at 273, 277, 282, 287 and 292 K respectively. The number of methyl groups with significant exchange contribution decreases with increasing temperature. At 292 K, RD could be observed for only two methyl groups (L50 δ_2 and L56 δ_2) that possess higher chemical variances than others (figure 3.2 (B)).

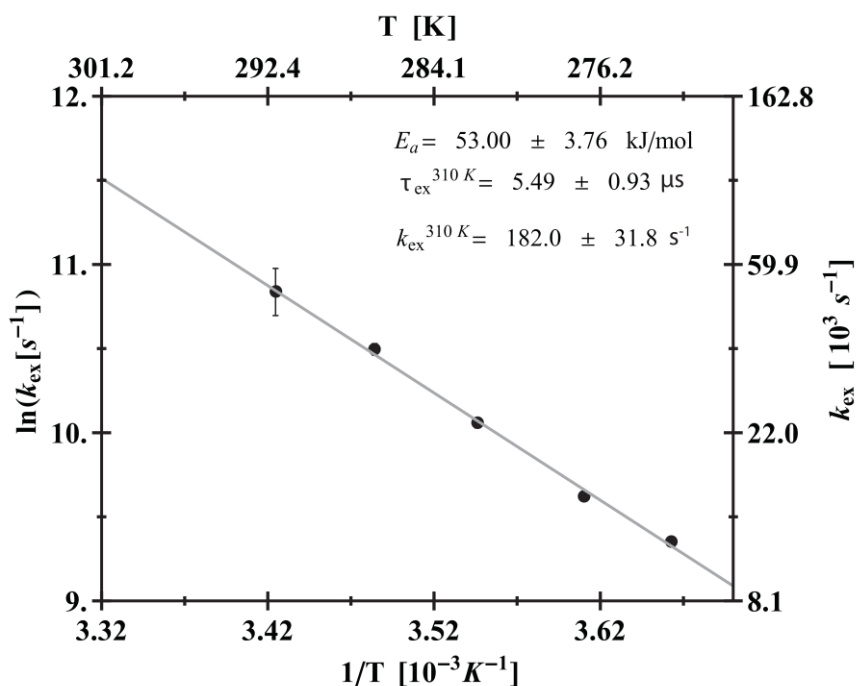


Figure 3.4: **Arrhenius fitting of global side-chain motion in ubiquitin.** Global exchange rates found in the side-chains of ubiquitin at different temperatures ranging from 273 to 292 K are shown in black dots. The gray line represents the fitting to the Arrhenius model as shown in equation 3.1. Obtained activation energies and the extrapolated timescale at 310 K are mentioned in the plot.

Arrhenius analysis was done with the global exchange rate obtained at each temperature from 273 to 292 K. Figure 3.4 shows the Arrhenius plot where the solid line was obtained from fitting the exchange rates with the following equation

$$\ln(k_{\text{ex}}) = \ln(A) - \left(\frac{E_a}{R}\right)\left(\frac{1}{T}\right). \quad 3.1$$

An activation energy of 53.0 ± 3.8 kJ/mol was obtained from the Arrhenius fitting. This matches with the activation energy of the global peptide-flip induced backbone motion of ubiquitin. From the fitted parameters, the timescale of the side-chain motion at physiological temperature (310 K) was extrapolated to be 5.5 ± 0.9 μs which is also the timescale of peptide-flip induced global motion found in the backbone of ubiquitin (Smith et al., 2016). These findings suggests that the observed side-chain motion of ubiquitin is linked with its backbone dynamics.

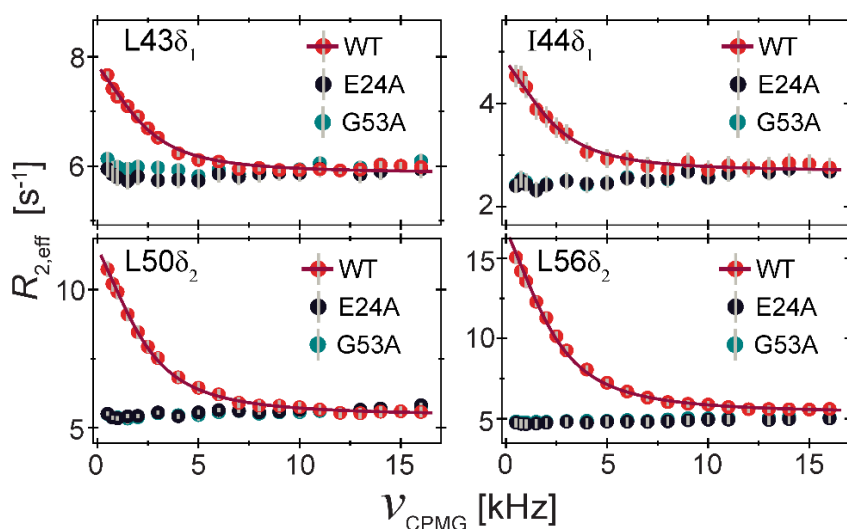


Figure 3.5: **Quenching of side-chain motion in single point mutants of ubiquitin.** ^{13}C E-CPMG relaxation dispersion profiles (RD) measured on methyl side-chains of the wild-type (red), E24A (black) and G53A (green) are shown here. All measurements were done at 277 K. The red lines indicate the global fitting of RD profiles from wild-type ubiquitin to the Luz-Meiboom model as shown in equation 3.4.

In a previous work from our group, two different single point mutants (E24A and G53A) were demonstrated to quench the peptide-flip induced global breathing motion in ubiquitin, which resulted in a decreased affinity of binding with USP2 (Smith et al., 2016). Both the mutants were shown to hinder the rearrangement of hydrogen bonds, which is necessary

for the peptide-flip to occur. From the observed timescale and the activation energy, now it is quite clear that the motion in the backbone and side-chains of ubiquitin are linked. To know if the peptide-flip is crucial for the global side-chain motion, we have applied the ^{13}C E-CPMG method to study the side-chain motions in both the mutants. Relaxation dispersion profiles of four methyl group that showed high exchange contribution (figure 3.2 (B)) in the wild-type ubiquitin are compared with the RD measured in both E24A and G53A mutants in figure 3.5. From this comparison, it is quite clear that RD originating from the side-chain conformational exchange is abolished in both the mutants. This indicates that the peptide-flip happening in the backbone of ubiquitin plays decisive role in the global side-chain motion of ubiquitin.

3.3 Conclusion

In this chapter, the E-CPMG approach is applied on the ^{13}C nuclei of methyl groups to study the side-chain motion in proteins. Side-chain dynamics of ubiquitin is investigated on a heavily deuterated and selectively $^{13}\text{CHD}_2$ labelled methyl groups of leucine, isoleucine and valine residues. The timescale and amplitude of the observed motion matches very well with a previous RD measurement based on $R_{1\rho}$ approach (figure 3.1). From our ^{13}C E-CPMG RD measurement at 277 K, the global timescale of motion in side-chains of ubiquitin is $66 \pm 1.8 \mu\text{s}$, whereas in the previous $R_{1\rho}$ study, this was found to be $61 \pm 1 \mu\text{s}$. In both the cases, the δ_2 -methyl carbon of residue L50 shows the most significant exchange contribution (0.2 ppm^2). A good correlation is observed (Pearson coefficient = 0.99) for amplitude of motion for all 10 methyl groups. Due to the robustness of the E-CPMG to detect both slow and fast motions, we could study the side-chain motion at low and high temperatures. Additionally, since the complete set of RD measurement could be performed with a single carrier offset, the entire experiment was done with much less measurement time compared to the $R_{1\rho}$ approach. From the Arrhenius analysis of the fitted global motion at several temperatures, the activation energy of the exchange process was found to be $53.0 \pm 3.8 \text{ kJ mol}^{-1}$, which matches with what is found for the peptide-flip induced backbone motion in ubiquitin (Chapter 4, figure 4.7). From extrapolation of Arrhenius fitting, for the first time, the timescale of the side-chain motion in ubiquitin at physiological temperature (310 K) was found to be $5.5 \pm 0.9 \mu\text{s}$. This is also the timescale of peptide-flip induced global motion in backbone of ubiquitin (Smith et al., 2016). The similarity in timescale, amplitude and activation energy barrier in both backbone and

side-chain motion suggests a common origin. To test this common hypothesis, side-chain dynamics were investigated in two mutants (E24A and G53A) of ubiquitin. Both the mutants are known to abolish the peptide-flip and hence the induced global backbone motion that was found to disrupt binding. All ^{13}C E-CPMG RD profiles of wild-type ubiquitin were suppressed in both the mutants. This confirms that the peptide-flip happening between D52-G53 is the source of the global side-chain motion in ubiquitin.

Appearing in all hydrophobic cores, methyl groups are crucial sites to extract key information about protein interior. Due to their excellent relaxation properties, side-chain methyl resonances appear sharp and resolved even in large protein complexes where signals from backbone cannot be clearly observed. In such cases, the dynamics observed through side-chain can be extrapolated to the backbone of the same protein due to the link we have found through this work.

3.4 Materials and Methods

3.4.1 Sample Preparation

For measuring ^{13}C E-CPMG relaxation dispersion experiments at temperatures ranging from 273 to 298 K, a ^{15}N labeled perdeuterated ubiquitin sample was produced with selective $^{13}\text{C}\text{HD}_2$ labelling in the following methyl groups δ_1 -Ile, δ_1 and δ_2 -Leu, and γ_1 and γ_2 -Val. The protein was expressed in *Escherichia coli*, which were adapted to 100% D_2O minimal medium, supplemented with D_7 -glucose as a carbon source and $^{15}\text{N}\text{-NH}_4\text{Cl}$ as a nitrogen source. Additionally, the selective $^{13}\text{C}\text{HD}_2$ labeling was done by adding two precursors; 2-keto- $3\text{D}_2\text{-}4\text{-}^{13}\text{C},\text{D}_2$ -butyrate and 2-keto-3-methyl- $\text{D}_3\text{-}3\text{-D}_1\text{-}4\text{-}^{13}\text{C},\text{D}_2$ -butyrate (Cambridge Isotope Laboratories) one hour prior to induction (Tugarinov, Kanelis, & Kay, 2006). The protein was then purified as described before (Lazar, Desjarlais, & Handel, 1997). NMR measurements were performed on a 3 mM protein sample in a D_2O buffer of pH 6.5 containing 20 mM sodium phosphate 50 mM NaCl and 0.05 % sodium azide. A standard 3 mm NMR tube was used for the measurement at all temperatures including 273 K.

3.4.2 NMR Experiments

The use of selective $^{13}\text{CHD}_2$ labeling of methyl groups in side-chains produced an AX spin system instead of AX_3 , which greatly reduced the complications involved in the ^{13}C CPMG measurements. All the NMR measurements were performed in a Bruker Avance III spectrometer operating at a ^1H Larmor Frequency of 600 MHz (14.1 T). The ^{13}C E-CPMG measurements were performed at 273 K, 277 K, 282 K, 287 K, 292 K and 298 K. Measurable exchange contributions were found at all temperature except at 298 K. Each of the two dimensional planes corresponding to a particular refocusing frequency was recorded with 50 complex points in the indirect dimension ($t_{1,\text{max}} = 45$ ms) and 1024 complex points in the direct dimension ($t_{2,\text{max}} = 143$ ms); 8 scans were performed for each of the FIDs. The recycle delay (d_1) was set to 3 s for better heat dissipation and to protect the integrity of the probe and amplifiers. To maintain the same sample temperature in all CPMG measurements, a heat-compensation block similar to the CPMG block was used during the recycle delay. The pulse program used for the measurements in this chapter is presented in Bruker format in the Appendix. The constant time CPMG measurements were performed as a pseudo-3D experiment in scan-interleaved fashion to spread out and minimize heating due to the RF irradiation. The CPMG block length was kept to 100 ms and 20 CPMG frequencies were acquired up to a maximum of 16000 Hz of refocusing frequencies.

3.4.3 Data Analysis

The ^{13}C E-CPMG raw data was divided and then co-added using a home-built perl script to generate multiple .ser files corresponding to every CPMG frequency. The time-domain data was then processed with NMRpipe (Delaglio et al., 1995). All processed 2D planes were loaded into Computer-Aided Resonance Assignment (CARA) program as .ft2 files and the intensities were extracted with a peak tolerance of 10 % in both dimensions to take care of any minor peak shift. The extracted intensities were then used to calculate the $R_{2,\text{eff}}$ values at different refocusing frequencies with the following equation

$$R_{2,\text{eff}} = \frac{1}{\Delta t} \ln \frac{I_{\text{ref}}}{I_{\text{CPMG}}} , \quad 3.2$$

where, Δt is the length of the CPMG delay (100 ms), I_{ref} is the intensity from the reference experiment where the CPMG block was omitted, I_{CPMG} is the intensity from CPMG measurement with a particular CPMG refocusing frequency. The uncertainty in intensity

was obtained by repeating three refocusing CPMG frequencies and their standard deviation was used to calculate the root-mean-square-deviation (RMSD) for every peak with the following equation

$$\Delta R_{2,eff} = \sqrt{(R_{2,eff}^{\text{repeat 1}} - R_{2,eff}^{\text{repeat 2}})^2}. \quad 3.3$$

Relaxation dispersion profiles were fitted to the Luz-Meiboom model (Luz & Meiboom, 1963) as described by the following equation

$$R_{2,eff} = R_{2,0} + \frac{4\pi^2 B_0^2 \Phi_{ex}}{k_{ex}} \left(1 - \frac{4\nu_{CPMG}}{k_{ex}} \tanh\left(\frac{k_{ex}}{4\nu_{CPMG}}\right) \right), \quad 3.4$$

using the NMinimize function of Mathematica. Uncertainties of the fitted parameters were obtained by Monte Carlo method with 100 runs.

4 Direct Detection of Pincer Mode Motion in Ubiquitin by ^1H E-CPMG

4.1 Introduction

4.1.1 Ubiquitin: The key player in eukaryotic biology

Ubiquitin is a small globular protein consists of 76 amino acids and has a molecular weight of 8.6 kDa. This regulatory protein is ubiquitously found in all eukaryotic cells and its amino acid sequence remains unchanged from invertebrate worms to humans (Allan & Phillips, 2017). “Evolutionary perfect” ubiquitin plays a crucial role in many cellular signaling networks, one of the most important being the protein degradation through “Kiss of death” (Brzovic & Klevit, 2006; Harper & Schulman, 2006). Being in the heart of eukaryotic biology, ubiquitin is studied routinely since its discovery about 50 years ago (Glickman & Ciechanover, 2002; Goldstein et al., 1975; Wilkinson, 2005), yet the mystery behind its broad range of recognition capability is not fully understood.

To control various cellular processes, ubiquitin binds to an extensive collection of modular proteins with great specificity (Hicke, Schubert, & Hill, 2005; Kliza & Husnjak, 2020). Knowledge about structure and dynamics of ubiquitin is crucial to understand the binding events. Except at the flexible C-terminal, ubiquitin has a compact, tightly hydrogen-bonded structure belonging to the β -grasp fold. The β -grasp fold is made of a mixed five-stranded β -sheet, a short 3_{10} -helix and a 3.5 turn α -helix. While the high-resolution structure of ubiquitin is well characterized decades ago (Vijay-Kumar, Bugg, & Cook, 1987; Vijay-Kumar, Bugg, Wilkinson, & Cook, 1985), its atomic resolution dynamics is constantly being discovered until today and a major portion is still undetected.

4.1.2 “Blind-spot” in ubiquitin dynamics

Dynamic processes in ubiquitin have been studied extensively in atomic detail mostly by two techniques; NMR spectroscopy and molecular dynamics simulation. A breakthrough in the field came in 2008 (Lange et al., 2008) when a structural ensemble of ubiquitin was calculated with constraints from an extensive set of Residual Dipolar Coupling (RDC) (36 NH RDC; 6 $^1\text{H}^{\text{N}}\text{C}'$, NC' RDC and 11 side-chain methyl RDC). Since RDCs can capture motion from milliseconds to picoseconds, the RDC refined ensemble indicated presence of supra- τ_c dynamics in ubiquitin, which was not possible to observe previously. This study indicated that the free ubiquitin ensemble covers the heterogeneity in conformations, which are found in bound complexes with a variety of binding partners, pointing to a conformational selection type binding mechanism.

Although RDCs can reveal the presence of motions in a wide range of timescales, it cannot directly quantify the dynamic process with its exact rate of interconversion and other kinetic parameters. Over the last decade, NMR based relaxation dispersion (RD) experiments have developed to be a powerful tool that can determine the specific timescale of motions in proteins (Ban et al., 2017). However, until very recently, due to technical limitation, RD could only detect motions with lifetime of 40 μs or slower (explained in Chapter 1). Due to this limitation, no RD profile could be observed for supra- τ_c motion in ubiquitin at room temperature. Off-resonance ^{15}N $R_{1\rho}$ performed at supercooled condition (265 K) could detect the presence of supra- τ_c motion at four different residues of ubiquitin (Ban et al., 2011). With ^1H $R_{1\rho}$, RD could be observed in more residues, spreading throughout the structure showing a common lifetime of 55 μs (Smith et al., 2016) at 277 K. This was attributed to a collective global motion (henceforth will be mentioned as peptide-flip motion), originating from rearrangement of hydrogen bond network due to flipping of the peptide bond between D52 and G53 in ubiquitin.

The RDC based structural ensemble of free ubiquitin (Lange et al., 2008) indicated that the largest amplitude conformational changes occur as a pincer like movement involving the β_1 - β_2 and β_3 - α_2 loops (from here onwards will be referred as pincer-mode motion). However, these two loops have shown a very small contribution to the peptide-flip mode (Smith et al., 2016). This indicated that the pincer-mode motion could occur in a much faster rate putting it in the “blind-spot” of NMR detectable timescale window. In this

chapter, I have described how the E-CPMG RD approach on backbone amide proton, enabled us to detect peptide flip motion in many more residues with much less experimental time and to detect pincer-mode motion in ubiquitin directly for the very first time.

4.2 Results and Discussions

4.2.1 ^1H E-CPMG: Linear Decay Compensation in RD Profiles

E-CPMG is a very useful approach for simultaneous detection of fast and slow motion in biomolecules. We have applied this method on ^{15}N (Reddy et al., 2018) and ^{13}C nuclei (Chapter 3) and experienced the benefits of measuring a large number of relaxation dispersion data sets in a much shorter measurement time compared to the $R_{1\rho}$ approach. This advantage comes from the fact that unlike in $R_{1\rho}$, in E-CPMG the measurement of the same experiment at multiple RF carrier offsets is not necessary. Here we have extended the limit further by going to a nucleus with a higher gyromagnetic ratio (^1H) where it is easier to achieve higher B_1 fields with less applied radio frequency power.

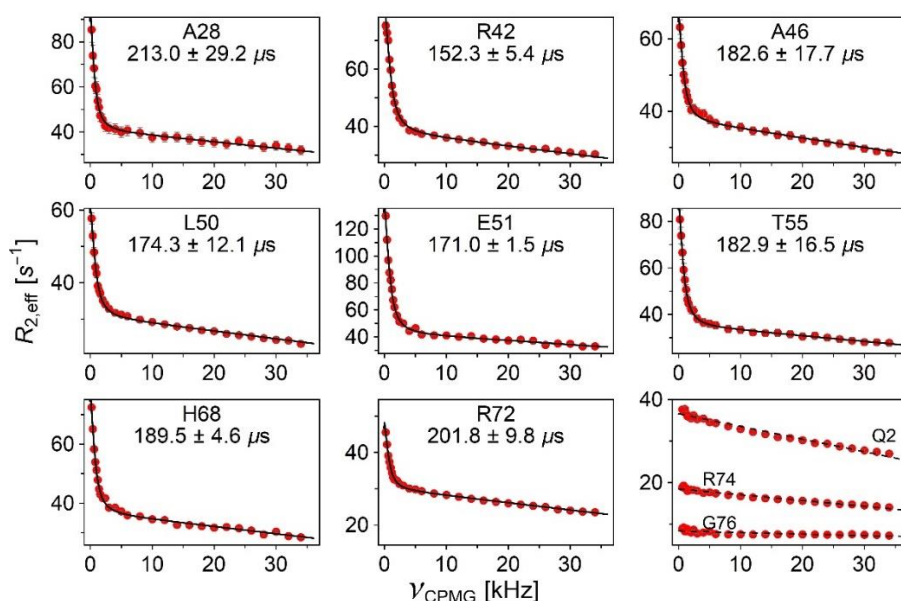


Figure 4.1: Fitting of dispersion profiles with measured R_1 as an input parameter.

^1H E-CPMG backbone amide proton relaxation dispersion profiles of selected residues of ubiquitin measured at 260 K at 950 MHz (22.3 T). Red dots denote the measured $R_{2,\text{eff}}$ values and black solid lines indicate the fitting to equation 4.4. Some of the flat profiles from both the C- and N- termini are shown on the right bottom corner, where the dashed black line is the fitting without any exchange term in equation 4.4.

^1H E-CPMG relaxation dispersion profiles were measured on backbone amide protons of a perdeuterated ubiquitin sample where the labile amide protons were back-exchanged. In figure 4.1 the uncorrected RD profiles measured at 950 MHz (22.3 T) at 260 K are shown with red dots. The dispersion profiles show a fast quench of $R_{2,\text{eff}}$ with increasing CPMG frequency till ~ 5 kHz and then a slow decay is seen till the last point. This second decay could be interpreted to arise from another exchange process.

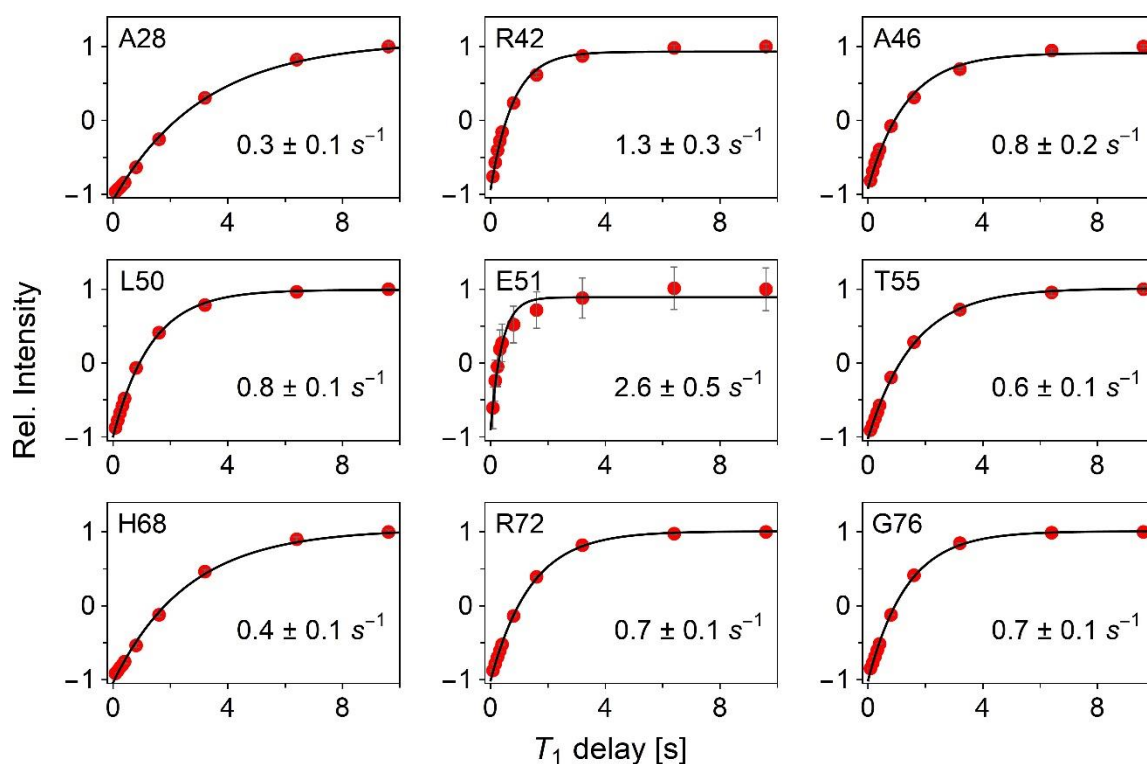


Figure 4.2: Measurement of R_1 rates of backbone amide protons in ubiquitin at 260 K. Selected inversion profiles measured at 950 MHz (22.3 T) are shown with red dots, and the black lines indicate fitting of the data to equation 4.5. Residue number and the fitted R_1 value of each residue is mentioned in the corresponding plot.

A closer look at the data revealed that RD profiles from all the residues of ubiquitin at 260 K shows this slow decay, including the terminal residues (right bottom corner of Figure 4.1) where relaxation dispersion is not expected. This made us realize that at such low temperature (260 K) and high B_0 field (22.3 T, $\omega_{\text{H}}/2\pi = 950$ MHz) R_2 values are much higher than R_1 which can induce a linear decay of the observed $R_{2,\text{eff}}$ as a function of CPMG frequency. This slow decay appears in the RD profile due to the phase cycle used

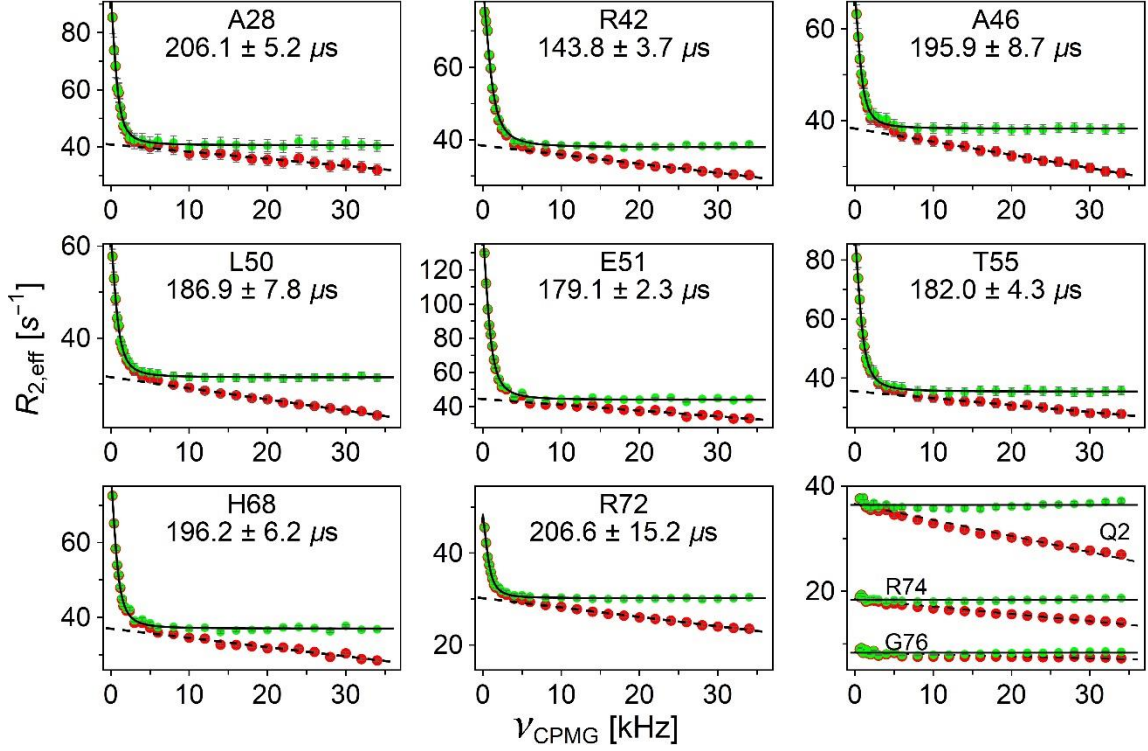


Figure 4.3: Additional decay correction in relaxation dispersion profiles. Red dots indicated the measured $R_{2,\text{eff}}$ from ^1H E-CPMG experiments, dashed black lines show the linear fitting of data points from 10 kHz onwards. Green dots are the corrected RD profiles, which are free from the decay coming from the phase cycle. The solid black line is the fitting of the corrected RD profile to equation 4.3.

in 180° pulses in the CPMG block (figure 4.8) as introduced by (Yip & Zuiderweg, 2004). The phase cycle is necessary to remove the off-resonance effects caused by the evolution of spins out of x-y plane during 180° pulses and inter-pulse delays, thereby mixing R_1 relaxation with R_2 . This results in multiple large amplitude oscillations in the R_2 decay profile, which creates complication in the extraction of accurate R_2 values. Although this phase cycle removed the offset dependence from R_2 rates through an equal balance of orthogonal and parallel evolution, it introduces a dependence on the number of 180° pulses, i.e. the CPMG frequency as

$$R_2^{\text{CPMG}} = \frac{(R_1 - R_2) \tau_\pi}{4 \tau_{\text{cp}}}, \quad 4.1$$

where τ_π is the length of 180° pulse and τ_{cp} is the delay between 180° pulses in CPMG block. This can be expressed as

$$R_2^{\text{CPMG}} = \frac{(R_1 - R_2)\tau_\pi \nu_{\text{CPMG}}}{2}, \quad 4.2$$

where $\nu_{\text{CPMG}} = \frac{1}{4\tau_{\text{cp}}}$ is the CPMG frequency.

As introduced in chapter 1 for two-site exchange in a fast exchange regime the Luz-Meiboom (Luz & Meiboom, 1963) model is described as

$$R_{2,\text{eff}} = R_{2,0} + \frac{4\pi^2 B_0^2 \Phi_{\text{ex}}}{k_{\text{ex}}} \left(1 - \frac{4\nu_{\text{CPMG}}}{k_{\text{ex}}} \tanh\left(\frac{k_{\text{ex}}}{4\nu_{\text{CPMG}}}\right) \right) \quad 4.3$$

If we incorporate the linearly decaying factor in all the points of dispersion profiles, the observed $R_{2,\text{eff}}$ ($R_{2,\text{eff}}^{\text{obs}}$) will be

$$R_{2,\text{eff}}^{\text{obs}} = R_{2,\text{eff}} + \frac{(R_1 - R_{2,\text{eff}})\tau_\pi \nu_{\text{CPMG}}}{2} \quad 4.4$$

If we fit the relaxation dispersion profiles with this corrected model, there is an extra fitting parameter (R_1) compared to the standard Luz-Meiboom model. A combination of many R_1 and R_2 values can fulfill the fitting criteria and that can restrict the optimization procedure to a local minimum. To avoid this obstacle, we have measured the longitudinal relaxation rates (R_1) for backbone amide protons of ubiquitin at 260 K (figure 4.2) on the same perdeuterated sample which was also used for all ^1H E-CPMG measurements. The R_1 measurement was performed using the method described previously (Markus, Dayie, Matsudaira, & Wagner, 1994). Selected inversion recovery profiles from some residues of ubiquitin are shown in figure 4.2 as red dots. The R_1 values were obtained by fitting the data to the following equation

$$I_t = I_0[1 - 2 \exp(-R_1 t)] \quad 4.5$$

which is shown as black lines in figure 4.2. The fitted R_1 values are mentioned inside corresponding plot.

All residues were found to have a very low R_1 which can be attributed to the stronger B_0 field ($\omega_{\text{H}}/2\pi = 950.38$ MHz, $B_0 = 22.3$ T), slower tumbling at lower temperature (260 K) and perdeuteration of the protein sample, all of which were required for the detection of fast dynamics by RD measurement. The obtained R_1 values were then used as an input parameter for fitting the dispersion profiles with equation 4.4. Selected dispersion profiles

are shown in figure 4.1 where red dots indicate the experimental data points and the fitted curve with equation 4.4 is shown as a solid black line. Obtained lifetimes of the exchange process are mentioned in the corresponding plot. In some residues, only linear decay was observed in the entire CPMG frequency range (bottom right corner of Figure 4.1). This decay does not indicate any exchange process and is coming from the mixing or R_1 and R_2 in the CPMG block. The fitting of these residues were done by removing the exchange terms from equation (4.3), i.e replacing $R_{2,\text{eff}}$ with $R_{2,0}$ which makes it a linear model with a slope proportional to both $(R_2 - R_1)$ and CPMG frequency.

By fitting the data in this manner we are removing the additional decay effect in the dispersion profile, originating from the phase cycle, which has no connection to the undergoing exchange process. Alternatively, we can determine this additional decay by fitting the last part of the dispersion profile where the exchange decay is already completed to a simple linear model. Subtraction of this linear decay from the original RD data generate RD profiles with decay originating only from the quenching of exchange contributions to relaxation. This corrected data can now be fitted directly with the simple Luz-Meiboom model as in equation 4.3. This correction procedure and subsequent fitting is demonstrated in figure 4.3. The red dots indicate the measured $R_{2,\text{eff}}$ values at 260 K and 950 MHz, the dashed black line indicates the additional linear decay originating from the phase cycle and the green dots indicate the corrected RD profile. The Luz-Meiboom model fitted to the corrected RD profiles are shown as solid black lines and the fitted exchange lifetimes are mentioned in the corresponding plot. The exchange lifetime obtained in this manner matches (within its uncertainty range) to when experimental R_1 is used as an input parameter (figure 4.1). The small amount of discrepancy can be attributed to the inaccuracy of measured amide proton R_1 values, which are known to have contributions from solvent exchange (Markus et al., 1994; Ulmer, Campbell, & Boyd, 2004). For the analysis of RD data at higher temperatures the method of linear correction prior to fitting was followed. Although the consequence of the use of this phase cycle was pointed out known before for single point R_2 measurement (Yip & Zuiderweg, 2004), this is the first time it is shown in RD profile.

4.2.2 Peptide flip motion found in more residues

The ^1H E-CPMG experiments on backbone amide protons of ubiquitin were measured at eight different temperatures from 260 K to 298 K at 950 MHz. At 260 K a total of 46 residues, distributed throughout the whole protein, show relaxation dispersion which were fitted to the Luz-Meiboom model as described in equation 4.3, to extract the timescale and

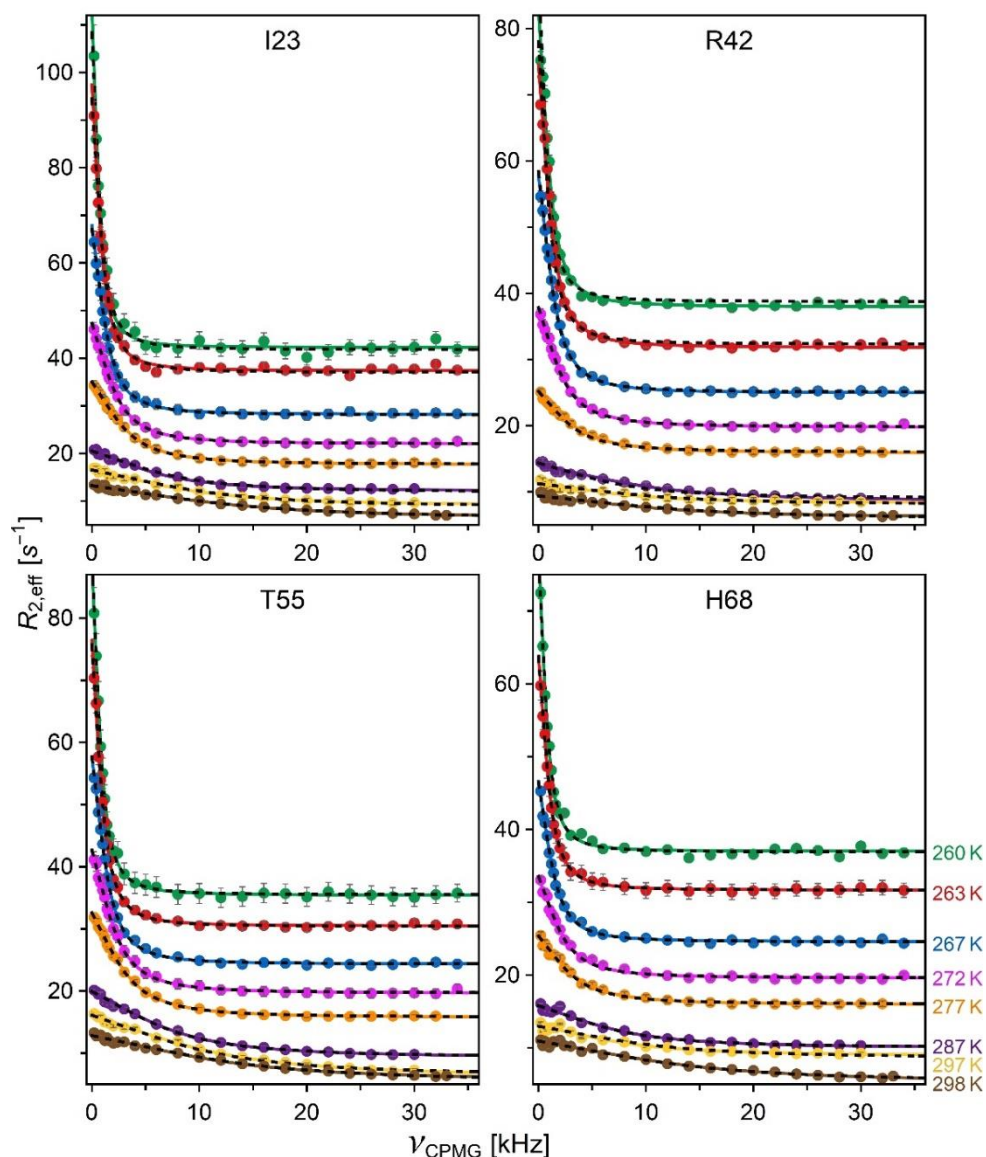


Figure 4.4: Temperature dependence of peptide flip motion in ubiquitin. ^1H E-CPMG backbone amide proton RD profiles of four selected residues, where detectable motion was found in all measured temperatures from 260 K to 298 K are shown in colored dots. The measurement temperatures are color coded and indicated in the right bottom corner. The individual fittings are shown in corresponding color in each temperature and the global fitting is represented by dashed black line.

amplitude of the underlying motion. Forty of these residues show similar exchange lifetimes in individual fitting and are shown as blue dots in figure 4.6. These residues could be globally fitted to a single timescale of $187.9 \pm 19.1 \mu\text{s}$ indicated as the blue arrow in figure 4.6. Previously we have identified this timescale as a collective motion, originating from a peptide bond flip between residues D52 and G53 (Smith et al., 2016). Figure 4.4 shows relaxation dispersion profiles of four such residues; the green dots indicate the experimentally measured $R_{2,eff}$ values at 260 K in a 2 mm capillary tube, the solid green line indicates the individual fitting of each residue and the black dashed line represents the global fitting where all residues were fitted to a single timescale. All dispersion profiles at different temperatures, individual fitting and global fitting are shown in figure A1, and all the fitted timescales are shown in table A1 in the appendix. Although this peptide-flip motion was previously detected by a combination of $^1\text{H}^{\text{N}}$ high power $R_{1\rho}$ and CPMG (up to 2.5 kHz CPMG frequency), with the application of the E-CPMG now we could detect the motion in more than twice the number of residues in much less NMR measurement time. One of the reasons behind finding the peptide-flip motion in more residues is the robustness of E-CPMG method, which makes it favorable in detecting both slow and fast motion at low and high temperatures, respectively, as described in (Reddy et al., 2018). Another advantage was the use of a single capillary instead of multiple capillaries in a 5mm tube (explained in materials and method of this chapter). This setup allowed us to reach 2 K lower temperature (260 K) compared to the previous study (Smith et al., 2016) without freezing the sample and in addition it allowed better dissipation of RF heating, since the VT gas now can directly access the sample tube.

Like at 260 K, at every temperature all dispersion profiles showing peptide-flip motion could be fitted to a single global timescale. The fitted individual and global timescales are plotted in figure 4.6 in blue colored dots and arrows respectively, and the fitted timescales are listed in table A.1 in the appendix. Residues that displayed the peptide-flip motion at 260 K are colored in blue in the PDB structure of ubiquitin (1UBI) in figure 4.7(A). The size of the blue spheres are proportional to the fitted chemical shift variance which represents the amplitude of motion. It can be seen from figure 4.7(A) that the residues showing higher amplitude of motion are in the close vicinity of the peptide bond between D52 and G53 which flips to generate the overall breathing motion in the whole protein.

Global exchange timescales and the Arrhenius fitting is shown in figure 4.7(B) and discussed in the following section.

4.2.3 Pincer-Mode Motion Found in Ubiquitin

In addition to the peptide-flip motion, the ^1H E-CPMG experiment at 260 K measured on backbone amide protons of ubiquitin, revealed the existence of a faster dynamic process in six residues. Relaxation dispersion profiles of these residues are shown in figure 4.5, where the green dots indicate the measured $R_{2,\text{eff}}$ at 260 K, and the green solid line represent the fitted curve to the Luz-Meiboom model as described in equation 4.3.

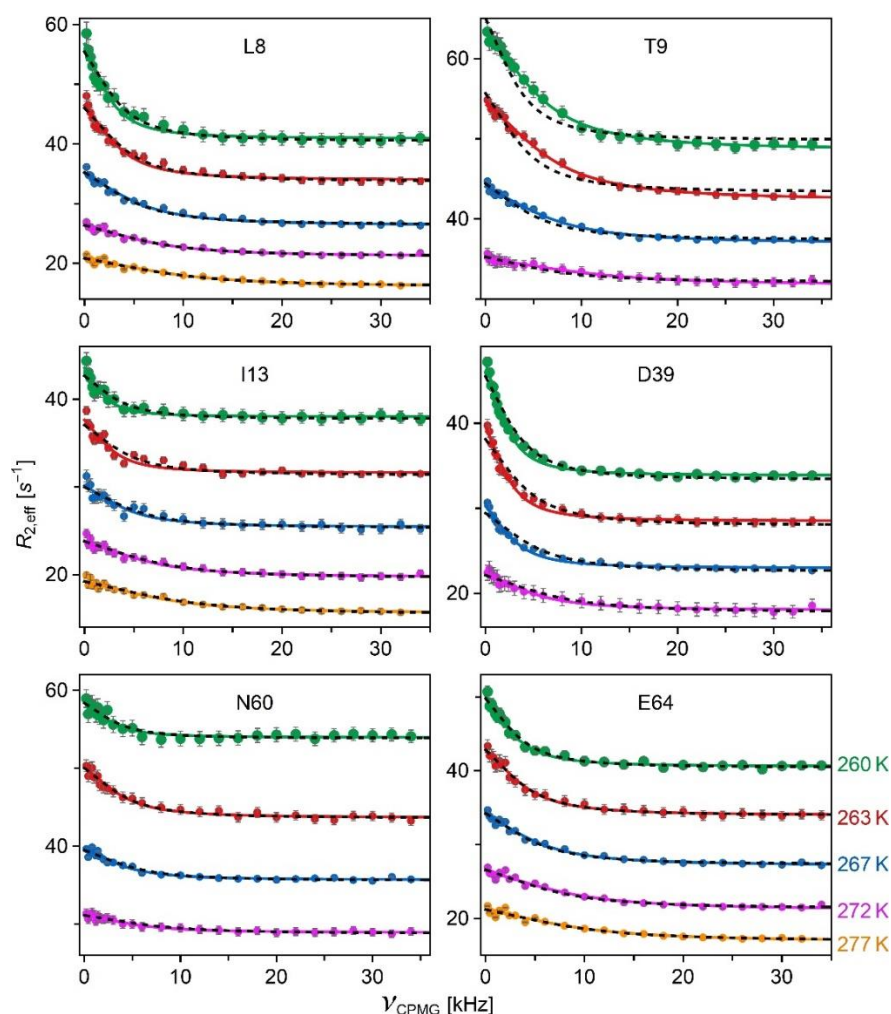


Figure 4.5: Relaxation dispersion profiles displaying timescales faster than the peptide-flip. ^1H E-CPMG RD profiles of all six residues that show the presence of a motion faster than peptide-flip are shown here with colored dots. The color code is explained in the right bottom corner of the figure. Individual fitting to equation 4.3 are represented with a solid line of corresponding color and the global fitting at each temperature is indicated as a dashed black line.

Table 4.1: Exchange parameters obtained from fitting dispersion profiles exhibiting pincer-mode timescale. The backbone amide ^1H E-CPMG profiles, shown in figure 4.5 were fitted to the Luz-Meiboom model as explained in equation 4.3. Both global (A) and individual (B) fitted parameters are listed below.

A

T [K]	Residue	L8	T9	I13	D39	N60	E64
260	τ_{ex} [μs]	45.1 ± 11.7					
	Φ_{ex} [10^3 ppm^2]	9.30 ± 0.73	9.47 ± 2.04	3.04 ± 0.54	7.54 ± 0.63	2.81 ± 0.79	5.80 ± 0.88
	$R_{2,0}$ [s^{-1}]	40.5 ± 0.3	49.8 ± 0.4	37.8 ± 0.3	33.4 ± 0.3	53.9 ± 0.3	40.5 ± 0.3
263	τ_{ex} [μs]	37.5 ± 8.3					
	Φ_{ex} [10^3 ppm^2]	9.20 ± 0.87	9.22 ± 1.97	4.25 ± 0.66	7.58 ± 0.58	4.78 ± 0.99	6.62 ± 1.02
	$R_{2,0}$ [s^{-1}]	33.7 ± 0.3	43.4 ± 0.4	31.4 ± 0.3	28.0 ± 0.3	43.6 ± 0.3	34.0 ± 0.3
267	τ_{ex} [μs]	30.9 ± 10.1					
	Φ_{ex} [10^3 ppm^2]	7.96 ± 1.51	6.35 ± 2.10	4.24 ± 1.11	6.23 ± 0.75	3.55 ± 1.10	6.29 ± 1.55
	$R_{2,0}$ [s^{-1}]	26.5 ± 0.4	37.4 ± 0.5	25.3 ± 0.4	22.6 ± 0.4	35.6 ± 0.4	27.3 ± 0.4
272	τ_{ex} [μs]	21.7 ± 8.4					
	Φ_{ex} [10^3 ppm^2]	6.72 ± 2.37	4.05 ± 4.80	5.38 ± 2.09	5.61 ± 1.55	3.01 ± 1.66	6.74 ± 2.96
	$R_{2,0}$ [s^{-1}]	21.2 ± 0.4	32.1 ± 0.6	19.6 ± 0.4	17.8 ± 0.3	28.8 ± 0.3	21.4 ± 0.4
277	τ_{ex} [μs]	17.0 ± 5.6					
	Φ_{ex} [10^3 ppm^2]	7.80 ± 4.17	-	6.15 ± 3.34	-	-	7.01 ± 4.21
	$R_{2,0}$ [s^{-1}]	16.1 ± 0.7	-	15.5 ± 0.6	-	-	17.0 ± 0.7

B

T [K]	Residue	L8	T9	I13	D39	N60	E64
260	τ_{ex} [μs]	60.6 ± 5.8	26.7 ± 2.8	78.1 ± 21.4	68.6 ± 7.8	56.4 ± 18.1	51.9 ± 8.2
	Φ_{ex} [10^3 ppm^2]	7.31 ± 0.61	15.68 ± 1.71	1.99 ± 0.45	5.41 ± 0.53	2.34 ± 0.67	5.15 ± 0.74
	$R_{2,0}$ [s^{-1}]	40.9 ± 0.3	48.6 ± 0.4	38.0 ± 0.3	33.9 ± 0.3	54.0 ± 0.3	40.6 ± 0.3
263	τ_{ex} [μs]	43.7 ± 5.3	23.4 ± 3.0	55.1 ± 13.8	61.3 ± 8.4	39.3 ± 9.3	38.5 ± 6.6
	Φ_{ex} [10^3 ppm^2]	8.03 ± 0.91	14.76 ± 2.06	3.06 ± 0.69	5.05 ± 0.60	4.58 ± 1.04	6.46 ± 1.06
	$R_{2,0}$ [s^{-1}]	34.0 ± 0.3	42.4 ± 0.4	31.6 ± 0.3	28.5 ± 0.3	43.7 ± 0.3	34.0 ± 0.3
267	τ_{ex} [μs]	28.8 ± 5.1	22.7 ± 5.1	36.5 ± 11.7	50.3 ± 10.4	36.8 ± 14.1	28.3 ± 6.3
	Φ_{ex} [10^3 ppm^2]	8.51 ± 1.54	8.70 ± 2.15	3.63 ± 1.14	4.07 ± 0.77	3.02 ± 1.12	6.86 ± 1.58
	$R_{2,0}$ [s^{-1}]	26.4 ± 0.4	37.0 ± 0.4	25.4 ± 0.3	23.0 ± 0.3	35.7 ± 0.3	27.2 ± 0.4
272	τ_{ex} [μs]	22.1 ± 6.8	14.1 ± 7.6	24.1 ± 9.1	30.0 ± 10.6	28.6 ± 18.9	19.0 ± 5.9
	Φ_{ex} [10^3 ppm^2]	6.61 ± 2.23	6.67 ± 4.52	4.83 ± 1.97	4.07 ± 1.46	2.29 ± 1.56	7.81 ± 2.79
	$R_{2,0}$ [s^{-1}]	21.2 ± 0.5	31.8 ± 0.7	19.7 ± 0.4	18.0 ± 0.4	28.9 ± 0.4	21.2 ± 0.5
277	τ_{ex} [μs]	16.5 ± 6.2	-	18.9 ± 8.7	-	-	16.4 ± 6.8
	Φ_{ex} [10^3 ppm^2]	8.10 ± 3.69	-	5.47 ± 2.96	-	-	7.32 ± 3.72
	$R_{2,0}$ [s^{-1}]	16.1 ± 0.6	-	15.6 ± 0.6	-	-	16.9 ± 0.6

Dashed black lines indicates the global fitting of all six residues to a single lifetime of $45.1 \pm 11.7 \mu\text{s}$. This timescale is more than four times faster compared to the peptide flip motion which has a lifetime of $187.9 \pm 19.1 \mu\text{s}$ at the same temperature. This motion with faster timescale could be detected at four other higher temperatures up to 277 K. RD profiles at higher temperatures are indicated in red (263 K), blue (267 K), magenta (272 K) and yellow (277 K). At these temperatures, the global timescale of motion was found to be $37.5 \pm 8.3 \mu\text{s}$, $30.9 \pm 10.1 \mu\text{s}$, $21.7 \pm 8.4 \mu\text{s}$ and $17.0 \pm 5.6 \mu\text{s}$ at 263 K, 267 K, 272 K and 277 K, respectively. Full set of global and individual fitting parameters are displayed in table 4.1(A) and table 4.1(B), respectively. Although our recently developed high power RD method is capable of detecting even faster motions, the amplitude of the RD profiles ($R_{\text{ex}} < 3 \text{ s}^{-1}$) were not high enough for getting any reasonable fit for extraction of exchange parameters at temperatures higher than 277 K. The exchange contribution to relaxation (R_{ex}) decreases at higher temperature because it is scaled by the higher exchange frequency (k_{ex}). Despite this scaling, the peptide-flip motion could be studied at eight residues up to 298 K, most of which are closer to the D52-G53 peptide bond, where the peptide bond flip occurs. This is because the peptide flip motion is originated by rearrangement of hydrogen bonding network in ubiquitin, which creates a bigger difference in chemical shift between the exchanging conformers, leading to higher chemical shift variance.

All residues showing the faster timescales are colored in red in the PDB structure of ubiquitin in figure 4.7(A). The radius of the red spheres represent the relative values of fitted chemical shift variance. Among these six residues that show faster timescales, L8 and T9 possess higher chemical shift variance, which contributes to higher exchange contribution in the dispersion profiles as shown in figure 4.5. These two residues happen to be in the first loop region of ubiquitin between the first ($\beta 1$) and second β -strands ($\beta 2$). Another residue that shows higher exchange contribution to relaxation is D39, which is also located in a loop region between the third β -strand ($\beta 3$) and the α -helix. Interestingly in previous studies (Lange et al., 2008; Peters & de Groot, 2012) both loops were found to be involved in a high-amplitude pincer-like movement from a structural ensemble of ubiquitin refined with a large set of RDCs. Through dihedral angle calculations of trajectories from one millisecond long MD simulation, D. E. Shaw and coworkers have computationally observed minor states, which differ in their conformation in both of these loops (Lindorff-Larsen, Maragakis, Piana, & Shaw, 2016). Dynamical content calculation

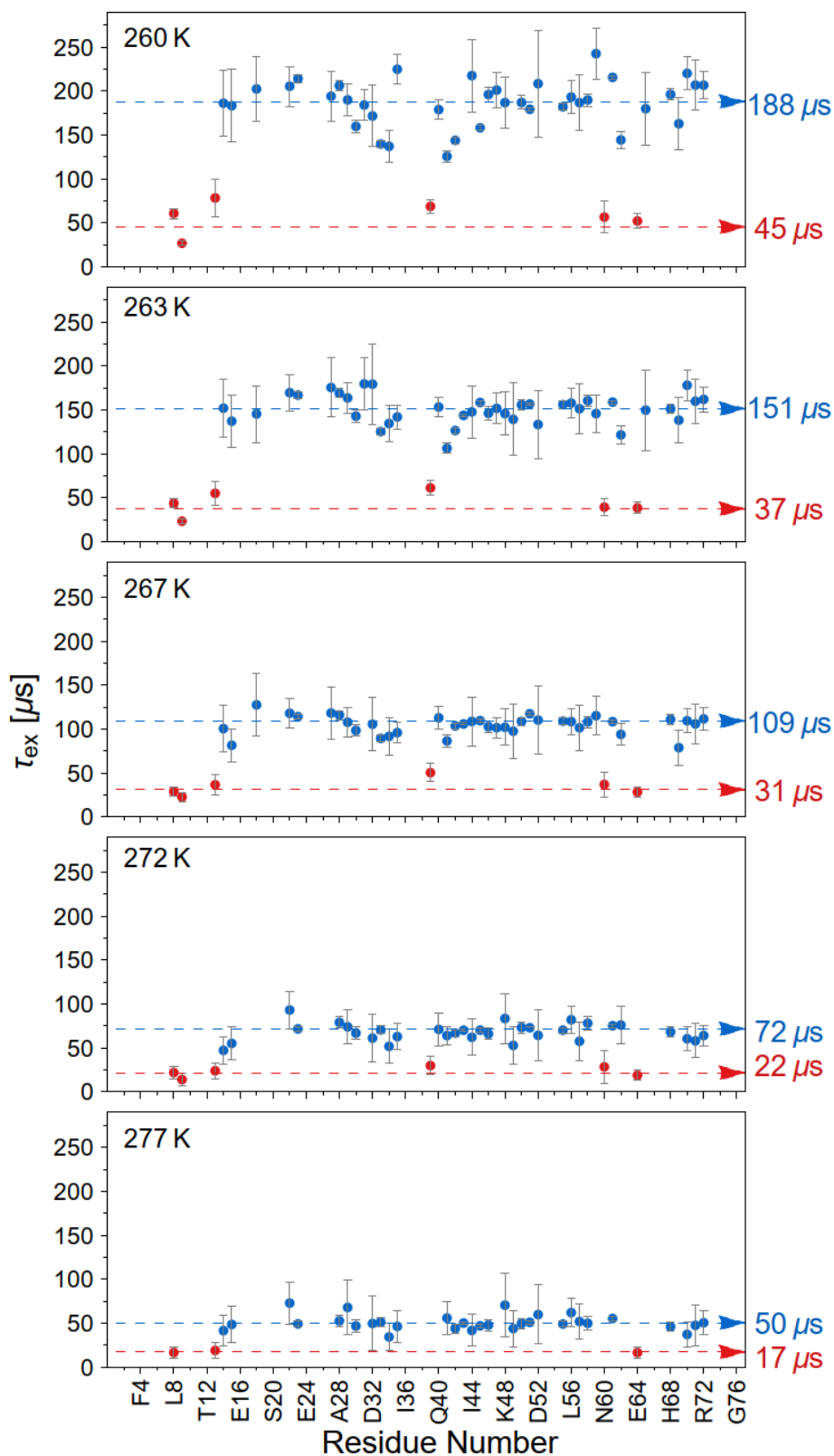


Figure 4.6: **Comparison of peptide-flip and pincer mode timescale.** Individual τ_{ex} values obtained from fitting dispersion profiles of residues showing peptide-flip (blue) and pincer mode (red) timescale are plotted against residue number. Arrows of corresponding color are drawn at the global τ_{ex} value at each temperature from 260 K to 277 K.

from this theoretical work indicated that this observed conformational fluctuation occurs in the supra- τ_c window of protein dynamics timescale spectrum. From these findings we can infer that the motion with faster timescale, observed directly for the first time through ^1H E-CPMG experiments, is coming from the pincer-mode motion.

4.2.4 Arrhenius fitting of obtained timescale of motions

^1H E-CPMG performed on backbone amide protons of ubiquitin shows two clusters of timescales at each temperature. These are represented as blue and red dots for residues showing peptide-flip and pincer-mode motion, respectively, in figure 4.6. The globally fitted timescales at each temperature are shown as arrows of corresponding colors.

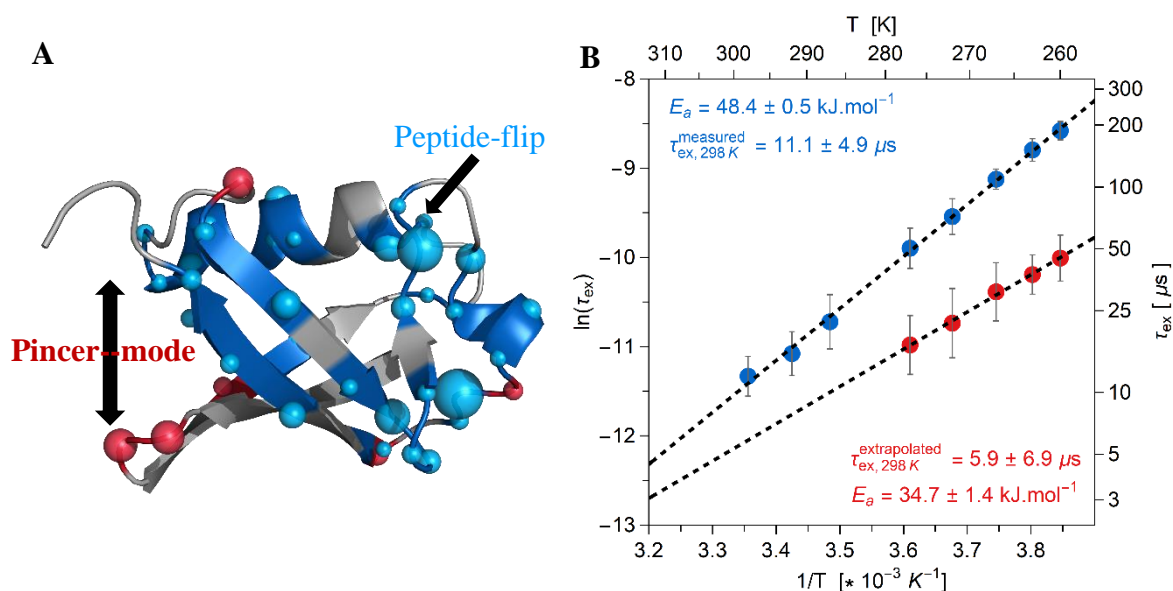


Figure 4.7: **Spatial and temporal distribution of peptide-flip and pincer-mode motion.**

(A) All residues that displayed peptide-flip and pincer-mode motions are colored in blue and red, respectively in the structure of ubiquitin (1UBI). The radius of the spheres indicates the amplitude (chemical shift variance) of the detected motion. (B) Arrhenius fitting is done with the global exchange rates found at different temperatures for both peptide flip (blue) and pincer-mode motion (red). Colored dots indicated the obtained global timescale, and the dashed black line represent the fitting to the Arrhenius model as shown in equation 4.6. Obtained activation energies and timescales at 298 K are mentioned in corresponding color.

As expected, with increasing temperature both the peptide-flip and the pincer-mode dynamics become faster resulting in lower exchange lifetimes. The logarithm of the global exchange lifetimes are plotted against the inverse temperature ($1/T$) in figure 4.7(B) in blue and red for peptide-flip and pincer-mode motion, respectively. Black dashed lines indicates the Arrhenius fitting of global exchange rates with the following equation

$$\ln(\tau_{ex}) = -\ln(A) + \left(\frac{E_a}{R}\right)\left(\frac{1}{T}\right) \quad 4.6$$

It is visible from figure 4.7(B) that the slopes of fitted lines are different for the two types of motions giving different activation energies, $48.4 \pm 0.5 \text{ kJ mol}^{-1}$ for the peptide flip and $34 \pm 1.4 \text{ kJ mol}^{-1}$ for the pincer mode motion. Due to this difference in slopes, the timescales of both types of motions come closer to each other at higher temperature. At 260 K the difference is more than a factor of four whereas at 277 K the factor is reduced to less than three. The peptide-flip motion involves breaking, formation, and redistribution of hydrogen bonds in ubiquitin whereas in the pincer-mode motion the loops move without involvement of any highly energetic processes. This could explain the lower activation energy for the pincer-mode motion. For the same reason conformers involved in pincer-mode movement are expected to differ less in chemical shift than those involved in peptide-flip motion, generating less chemical shift variance (CSV) and hence less exchange contribution to relaxation. This could be the reason behind less observed CSV for the pincer-mode motion although it is found to be the highest amplitude motion of ubiquitin in many previous studies (Lange et al., 2008; Michielssens et al., 2014; Peters & de Groot, 2012; Smith et al., 2016). Although the peptide-flip motion could be detected directly at room temperature with a timescale of $11.1 \pm 4.9 \text{ } \mu\text{s}$, the pincer-mode motion was not possible to capture at temperatures higher than 277 K due to the lower lifetime and smaller chemical shift change involved in this motion. From Arrhenius fitting of the pincer-mode motion the lifetime at 298 K was extrapolated to be $5.9 \pm 6.9 \text{ } \mu\text{s}$, which is twice as fast than peptide-flip motion at this temperature.

4.3 Conclusion

The application of ^1H E-CPMG experiments on backbone amide protons of ubiquitin is demonstrated in this chapter. We found a linear decay in all RD profiles arising from the phase cycle of 180° pulses in the CPMG block, required for removing off-resonance effects. The linear decay was corrected with the help of theoretical interpretation published

previously (Yip & Zuiderweg, 2004) and decoupled from the quenching of the exchange contribution to the relaxation rate. Although the linear decay is present in almost all CPMG experiments, at least as a minor contribution, this is the first experimental demonstration of such a decay behavior. This correction is more relevant for CPMG measurements of large molecules at very high magnetic field due to the greater difference of R_2 and R_1 . Applying this correction method, the backbone dynamics of ubiquitin was studied in eight different temperatures, ranging from supercooled condition at 260 K to room temperature (298 K). This led to the finding of already observed peptide-flip motion in double the number of residues. In addition to that, for the very first time, we could directly detect the pincer-mode motion in ubiquitin through high power RD experiments, which was previously predicted to exist from both experimental and computational methods (Lange et al., 2008; Michielssens et al., 2014; Peters & de Groot, 2012; Piana, Lindorff-Larsen, & Shaw, 2013). The global timescales of these two types of motion differ significantly at lower temperature (260 K) but the difference decreases at higher temperature. From Arrhenius fitting, this led to a higher activation energy for the peptide-flip than the pincer-mode motion. This could be attributed to the involvement of hydrogen bond breaking, formation and rearrangements, all of which are absent in the pincer-mode motion. It has already been described in many previous studies that the pincer-mode motion contributes to the conformational adaption power of ubiquitin while binding to other proteins (Michielssens et al., 2014; Peters & de Groot, 2012). Direct observation of this motion finally enlightens the “blind-spot” in ubiquitin dynamics, which will help for a better understanding of binding mechanisms.

4.4 Materials and Methods

4.4.1 Sample Preparation

All NMR experiments mentioned in this chapter were performed on a ^{15}N labeled perdeuterated ubiquitin sample. The sample was purposefully not labeled with ^{13}C nuclei to avoid the necessity of ^{13}C decoupling, which could be an extra source for RF heating. In addition, the heteronuclear J coupling of the $\text{C}\alpha$ and carbonyl carbon to the nearby amide proton and nitrogen nuclei can be a source of artifacts in relaxation dispersion profiles. ^{15}N labeled perdeuterated ubiquitin sample was expressed in *Escherichia coli*, which were adapted to a 100% D_2O Toronto minimal medium, supplemented with D7-glucose as a carbon source and $^{15}\text{N}\text{-NH}_4\text{Cl}$ as nitrogen source. The protein sample was purified as

described before in the previous chapter. NMR measurements were performed on a 3 mM protein sample in a 20 mM sodium phosphate buffer of pH 6.5 containing 50 mM NaCl and 0.05 % sodium azide. 5% D₂O was added before the NMR measurements.

For reaching supercooled conditions, a new and more convenient approach was taken. Instead of transferring the sample to multiple 1 mm capillaries and then putting them to a 5 mm tube, the protein sample was directly transferred to a single capillary of 2 mm outer diameter and 1.6 mm inner diameter (bought from Bruker). The sample could be transferred using a simple long pipette tip and, unlike the work described in previous chapters, no Hamilton syringe was necessary which are difficult to clean. About 80 μ l of sample volume was needed for achieving good shimming. These capillaries were 10 cm long which is about half of the length of normal NMR tube, hence a special sample holder (bruker MATCH system) was needed to put the sample in magnet. This also ensure the position of capillary at the center of coil volume. Supercooled conditions (up to 260 K) were reached by slowly decreasing the temperature (0.5 K / minute) after inserting the sample into the magnet.

4.4.2 NMR Experiments

All NMR experiments described in this chapter were measured on a Bruker Avance III HD spectrometer operating at a ¹H Larmor Frequency of 950 MHz (22.3 T), equipped with a 5 mm triple resonance (H-C/N-D) new generation cryogenically cooled probe, capable of operating at supercooled temperatures. An in house pulse sequence was used for the ¹H E-CPMG measurements which can be found in the appendix. The constant time CPMG measurements were performed as pseudo 3D experiments in scan interleaved fashion to spread out and minimize the heating due to RF irradiation. The CPMG block length was kept to 20 ms and a total of 28 CPMG frequencies were acquired up to 35000 Hz. Each two dimensional plane corresponding to a particular CPMG frequency were acquired with 64 complex points in the indirect dimension ($t_{1,max} = 31.62$ ms) and 512 complex points in the direct dimension ($t_{2,max} = 38.5$ ms); 8 scans were performed for each FID. The recycle delay (d_1) was set to 2 s for better heat dissipation and to protect the integrity of the probe and amplifier.

4.4.3 Data Analysis

The scan interleaved E-CPMG data was divided and then co-added using a home-built perl script to generate multiple .ser files corresponding to every CPMG frequencies. The time-domain data was then processed with NMRpipe (Delaglio et al., 1995). All processed 2D planes were loaded to Computer-Aided Resonance Assignment (CARA) as .ft2 file format and the intensities were extracted with a peak tolerance of 10% in both dimensions to take care of minor peak shifts. The extracted intensities were then used to calculate $R_{2,eff}$ values at different refocusing frequencies with the following equation;

$$R_{2,eff} = \frac{1}{\Delta t} \ln \frac{I_{ref}}{I_{CPMG}} \quad 4.7$$

Where, Δt is the length of CPMG delay (20 ms), I_{ref} is the intensity from reference experiment, where the CPMG block was omitted, I_{CPMG} is the intensity from CPMG measurement with a particular CPMG refocusing frequency. The uncertainty in intensity was obtained by repeating three refocusing CPMG frequencies and their standard deviation was used to calculate the root-mean-square-deviation (RMSD) for every peak with the following equation

$$\Delta R_{2,eff} = \sqrt{\left(R_{2,eff}^{repeat\ 1} - R_{2,eff}^{repeat\ 2}\right)^2} \quad 4.8$$

Relaxation dispersion profiles were fitted to Luz-Meiboom model as described in equation 4.3 using the NMinimize function in Mathematica software. Uncertainties of the fitted parameters were obtained by a Monte Carlo method with 100 runs.

5 Rapid Conformational Exchange in intrinsically disordered p53-TAD domain

5.1 Introduction

In the previous chapters, I have described detection of several hidden motion in backbone and side-chain of folded proteins using the recently developed high-power relaxation dispersion method in our group (Ban et al., 2012; Pratihari et al., 2016; Smith et al., 2016). Unveiling of the kinetics helped us for better understanding of protein-protein binding and molecular recognition processes. In this chapter, I turn our attention to an intrinsically disordered protein (IDP). As a challenge to the “Structure-function paradigm” intrinsically disordered proteins (IDP) or regions (IDR) have emerged as a key player in many signaling and gene regulation processes (Tompa, 2012). The transcriptional activation domain (TAD) in the N-terminal of protein p53 is one such protein with known structural disorder (Borchers et al., 2014).

5.1.1 N-terminal TAD Domain of Protein p53

Gaining fame from its tumor-suppression role, p53 is one of the most extensively studied multifunctional protein in humans (Royds & Iacopetta, 2006). While overexpression of p53 can cause unnecessary apoptosis, under-expression of this protein may lead to cancer. MDM2 keeps the optimum balance of cellular concentration of p53 by binding and marking it for ubiquitin-mediated degradation (Jebelli, Hooper, Garden, & Pocock, 2012; Vousden & Lane, 2007). However, under stressed conditions of cells, MDM2 does not bind to p53 leading to a buildup of its concentration which cause cell cycle arrest (Borchers et al., 2014; Lee et al., 2000). To perform as a cellular antagonist, MDM2 binds to p53 through its disordered N-terminal TAD domain (Chi et al., 2005). Hence, understanding the

structure and dynamics of the TAD domain is crucial for having useful insight into the binding mechanism.

Although this domain is claimed to be mostly disordered from several studies (Bell, Klein, Muller, Hansen, & Buchner, 2002), there are reports where presence of transient structural elements were observed. In a NMR based study, TAD was found to be loosely folded containing a preformed helix and two turn regions. Local helical structure was found in the stretch of residues T18-L26 whereas residues between M40-W53 were reported to take part in transient turn formation (Lee et al., 2000). A single turn helix was predicted to exist in residues L22-K24 from a combination of RDC and small-angle x-ray scattering (SAXS) measurements. Although these studies suggest that TAD exists as a disordered or loosely structured protein in the unbound state, it was found to contain fully formed secondary structural elements in its complexes with other proteins. Residues 15-35 of TAD are found to be in a helix motif in its complex with MDM2 (Kussie et al., 1996; Schon, Friedler, Bycroft, Freund, & Fersht, 2002). From these studies, it seems that the preexisting secondary structural propensities play an important role in the binding processes of TAD domain. In this scenario, understanding the timescale and amplitude of the conformational exchange in free p53-TAD domain could give useful insight. This makes it an ideal system to be studied by our recently developed high power RD method, which currently can detect single digit microsecond motion.

5.2 Results and Discussion

5.2.1 Fast Conformational Exchange Found in Wild-type p53-TAD

The high-power amide ^1H off-resonance $R_{1\rho}$ RD was applied to the wild-type p53-TAD domain on a perdeuterated sample. No detectable exchange contribution was found at the temperatures between 277 and 298 K. This suggested, either the chemical shift difference and/or the population of different conformers are too small or the exchange process is faster than what can be detected by the high power RD method ($< 2.8 \mu\text{s}$). To test the second hypothesis we reduced the measurement temperature to the supercooled regime, for slowing down any fast and undetected dynamics. The RD experiment was performed at 263 K in 1 mm capillaries (described in materials and method), keeping the sample in liquid state. At this temperature, six residues displayed significant $R_{2,\text{eff}}$ dispersion in the $R_{1\rho}$ RD profiles (figure 5.1). When the RD profiles were fitted individually with equation 5.2

(materials and method), lifetimes in the range of 3.4 to 4.4 μs were obtained, as shown by the black curve and the mentioned values in the corresponding plot. All of the six residues could be fitted globally to a single lifetime of $4.15 \pm 0.19 \mu\text{s}$. The global fitting of all RD profiles are shown by the green curve in each plot.

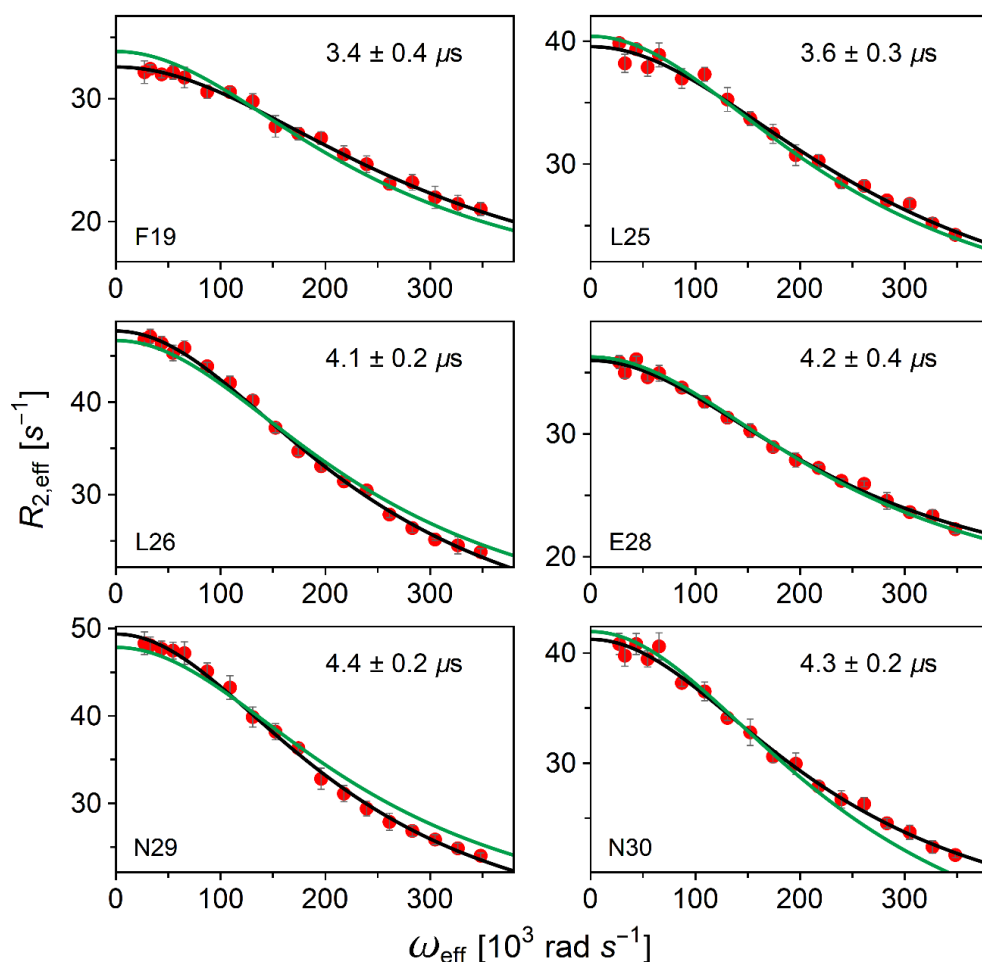


Figure 5.1: **Backbone amide proton $R_{1\rho}$ relaxation dispersion profiles of p53-TAD at 263 K.** The red dots indicated the experimentally measured $R_{2,\text{eff}}$ values obtained from high-power off-resonance $R_{1\rho}$ measurements. The black line denotes the individual fitting curve for each residue to equation 5.2, and the fitted lifetimes obtained from this fitting is shown in corresponding plot. All six RD profiles could be fitted globally to a single lifetime of $4.15 \pm 0.19 \mu\text{s}$, which is denoted by the green line.

This is, to our knowledge, the fastest detected motion so far by any NMR RD (CPMG and $R_{1\rho}$) measurement. The lifetime of $\sim 4 \mu\text{s}$ for all six residues suggests that they could be involved in some global exchange process, which remained undetected by RD before due to the limitation in applied B_1 field for both CPMG and $R_{1\rho}$. In addition, this demonstrate

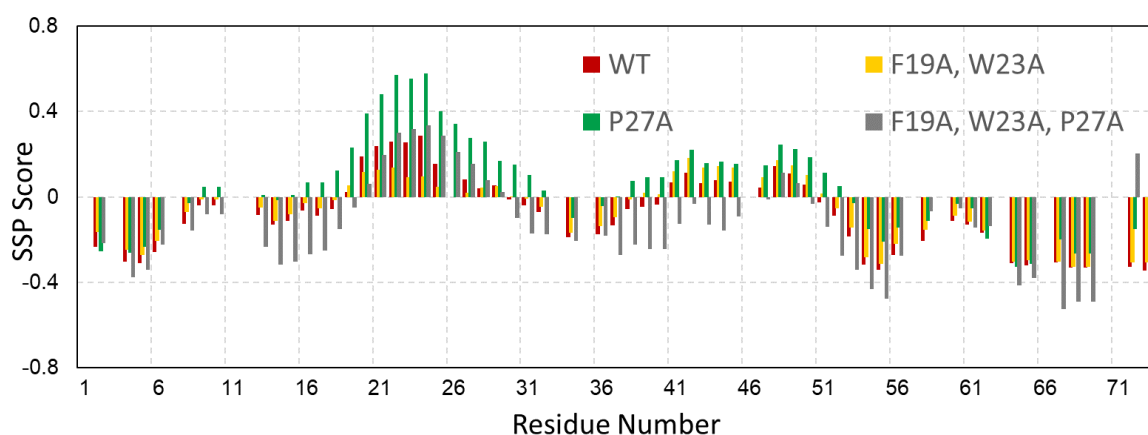


Figure 5.2: Secondary structure propensity (SSP) scores calculated from chemical shift. SSP scores were calculated for the wild-type (red), P27A (green), F19A; W23A (yellow) and P27A; F19A; W23A (gray) mutants of protein p53-TAD from the experimentally obtained chemical shifts. Positive values of SSP scores indicate the helical propensity and the negative values suggest the propensity for β -strand.

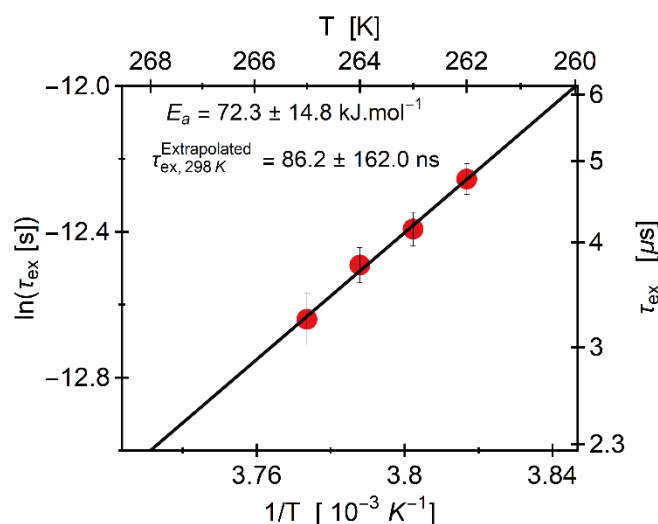


Figure 5.3: Arrhenius fitting of the global lifetimes obtained from $R_{1\rho}$ measurements on wild-type p53-TAD. Global exchange rates, found at different temperatures ranging from 262 to 265 K are shown in red dots. The gray line represents the fitting to the Arrhenius model as shown in equation 5.3. Fitted activation energy and the extrapolated timescale of motion at 298 K are mentioned in the plot.

the necessity of supercooled condition together with the high-power RD was necessary for detecting the fast exchange process in p53-TAD.

From the experimentally observed chemical shift of CO, C^α, C^β, amide ¹H, and amide ¹⁵N secondary structural propensity (SSP) scores were calculated following the work of (Marsh, Singh, Jia, & Forman-Kay, 2006). This method provides residue specific SSP scores by combining all of the above-mentioned chemical shifts which can indicate the presence of a transient structure in intrinsically disordered proteins. This method of secondary structure estimation is more reliable than reporting just $\Delta\delta C^\alpha$, because it weighs every chemical shift with their accuracy of distinguishing different secondary structures. The calculated SSP scores for residues of wild-type p53-TAD is shown in red bars in figure 5.2. Since TAD is reported to have transient helical structure in free form and fully formed helix in bound complexes, we focus towards helical propensities from SSP score. Elevated SSP (~30%) values can be seen for residues 20-27, which indicates existence of helical propensities. Interestingly the same stretch of residues showed significant exchanges contribution from the high power RD measurements. This suggests, the exchange process that we have observed in p53 could be helix formation from random-coil conformations.

To estimate the activation energy barrier for the observed conformational exchange with Arrhenius fitting, the RD experiments were performed at different temperatures. Unfortunately, the fast motion could be detected only at four temperatures in a very narrow window from 262 to 265 K. Below 262 K the liquid sample was frozen and above 265 K the lifetime was beyond the detection limit of high power $R_{1\rho}$ method. At these four temperatures, the same six residues showed detectable exchange contributions and in each temperature, all RD profiles could be fitted to a single global timescale. The observed lifetimes were 4.76 ± 0.20 , 4.15 ± 0.19 , 3.76 ± 0.18 and 3.24 ± 0.23 μ s at 262, 263, 264 and 265 K respectively. These lifetimes are plotted in figure 5.3 against the inverse of temperature ($1/T$) for Arrhenius analysis. The black line indicates the Arrhenius fitting with equation 5.3. An activation energy of 72.3 ± 14.8 kJ/mol was obtained from the Arrhenius fitting and the timescale of the motion at room temperature (298 K) was extrapolated to be 86.2 ± 162.0 ns. Narrow range of temperatures (262-265 K) at which the motion could be detected is reflected in the high uncertainty of the extrapolated timescale. Such fast lifetime (~90 ns) is still at a great distance from the current detection limit of our high-power RD method (> 2.8 μ s)

5.2.2 Slower Dynamics in P27A Mutant of p53-TAD

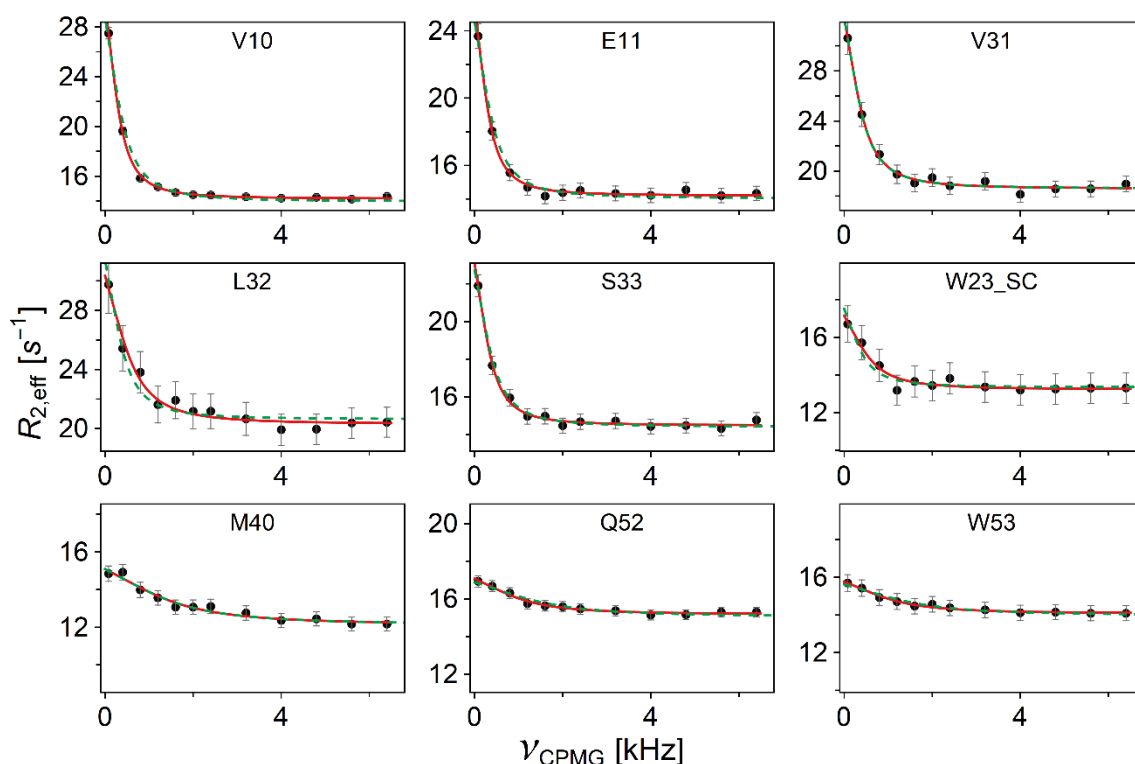


Figure 5.4: ^{15}N E-CPMG relaxation dispersion profiles obtained from P27A mutant of p53-TAD, measured at 263 K. Selected residues from different region of the protein backbone and side-chain are displayed here. The red lines indicates the individual fitting of experimentally obtained $R_{2,\text{eff}}$ values to the Luz-Meiboom model as described in equation 5.6. RD profiles from residues in the helix region and the side-chain of W23 were fitted globally to a single lifetime of $379.1 \pm 45.9 \mu\text{s}$, which is represented by the dashed green line. Whereas for the residues appearing in the second helical region, a faster lifetime of $103.7 \pm 12.5 \mu\text{s}$ was observed.

The residual helicity of p53-TAD is known to have significant impact on its binding affinity with MDM2 *in vitro* and in cells (Borcherds et al., 2014). In this study, the most preserved proline residue (P27) between human, frog, mouse and chicken was replaced by alanine. This substitution of proline, just outside the binding site (aa19-25) resulted in tenfold stronger binding with MDM2 that ultimately hindered cell cycle arrest ability of the protein p53. To investigate the effect of this mutation on the helical content, we performed SSP score calculation with the experimental chemical shifts obtained from the P27A mutant of p53-TAD. In can be seen from figure 5.2 (green bars), that the SSP scores have become twice compared to the wild-type protein in the first helical region, which indicates a twofold

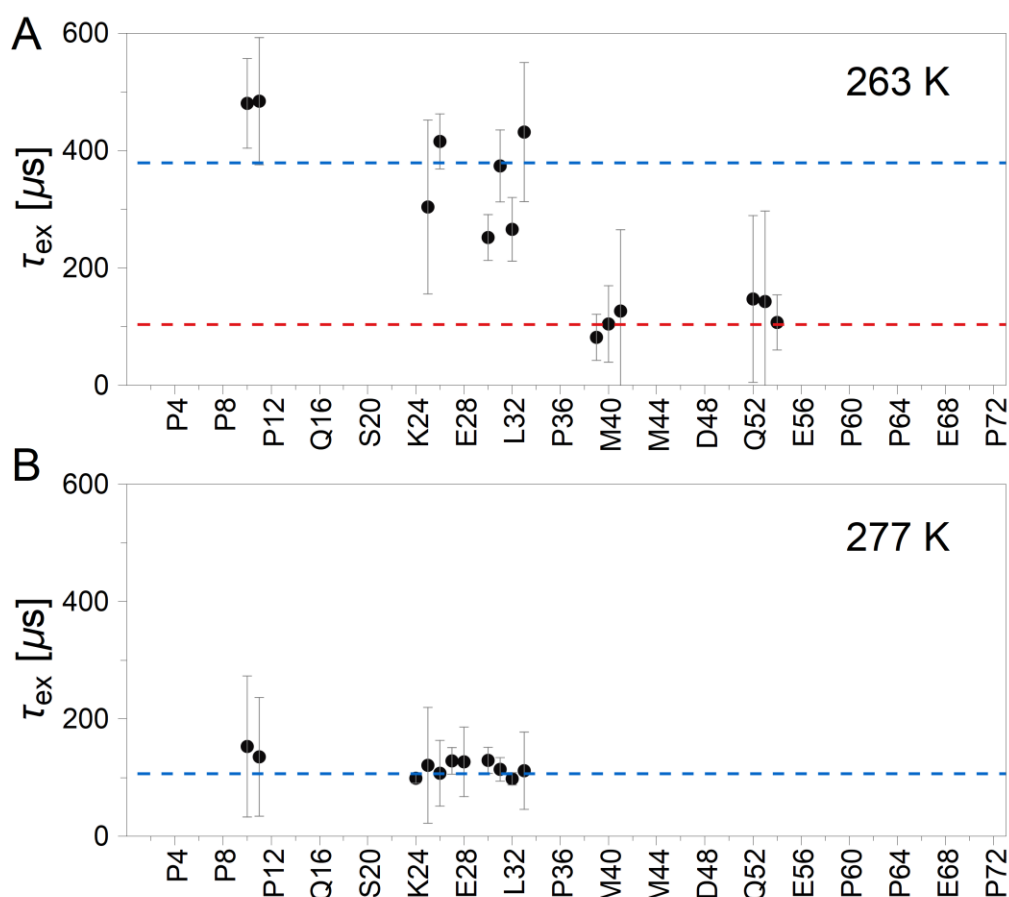


Figure 5.5: Temperature dependence of dynamics in P27A mutant of p53-TAD, obtained from ^{15}N E-CPMG experiment. Individually fitted lifetime (τ_{ex}) values from the fitting of dispersion profiles (RD) at 263 K (A) and 277 K (B) are shown here with black dots. The global exchange value of the residues in two helical segments are indicated with blue and red dotted lines. No residue in turn regions showed RD at 277 K.

increase in helical propensities (60%). This increased helicity was previously reported in the above-mentioned work (Borcherds et al., 2014) from $\Delta\delta C^\alpha$. Additionally, the residues in the stretch of 38-55 also shows increased helical contents in the mutant.

To examine the exchange timescale in the P27A mutant, ^{15}N E-CPMG RD was performed at 263 K, where exchange contribution was seen in total 15 residues. Nine of these RD profiles are shown in figure 5.4. A dramatic reduction of ~ 100 fold in the exchange lifetime from the residues in the first helical segment was observed in the P27A mutant compared to the wild type p53-TAD. In addition to backbone amide ^{15}N , RD was also observed in the

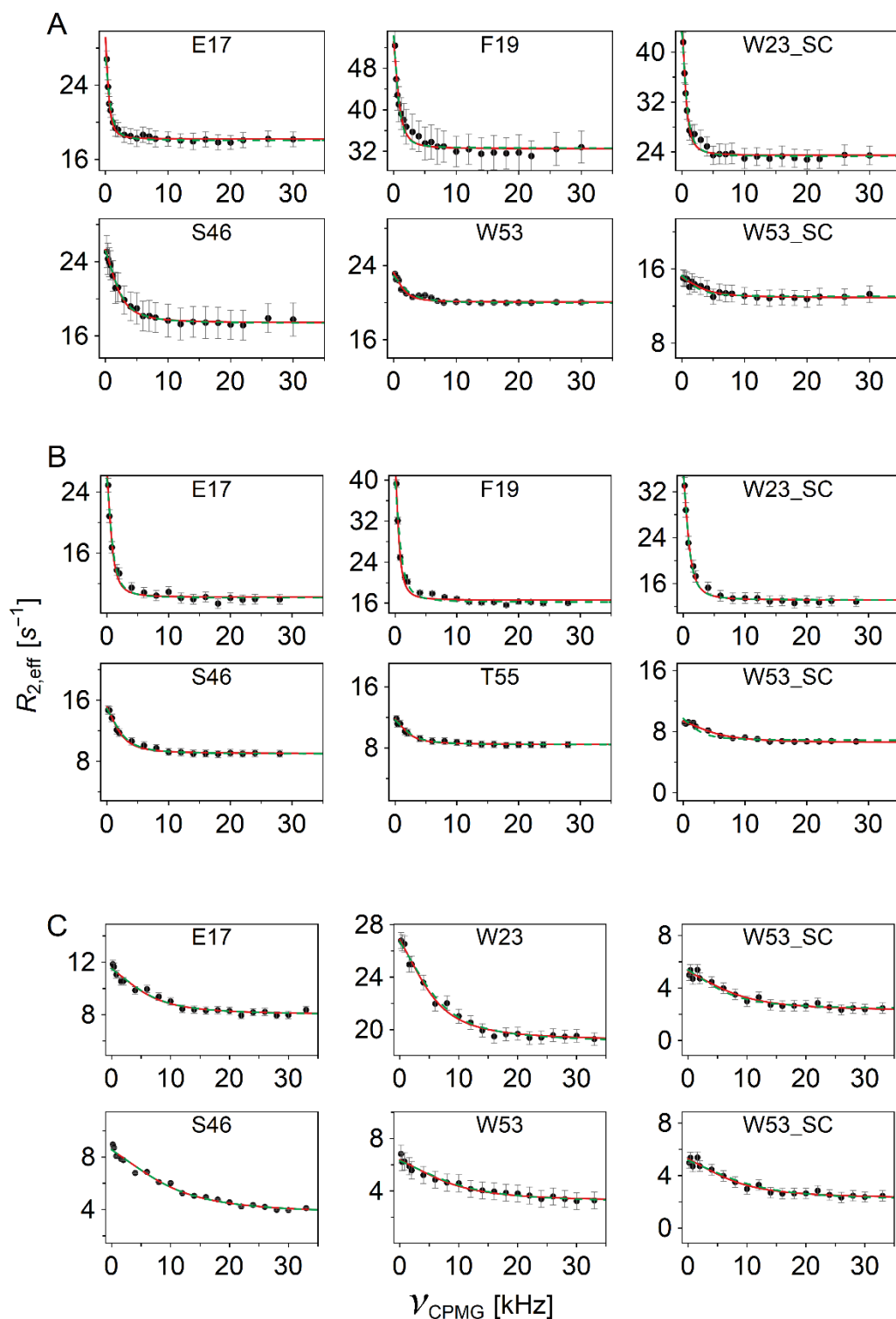


Figure 5.6: ^1H E-CPMG RD profiles of P27A mutant of p53-TAD at different temperatures. RD profiles of selected residues from helix-1 (E17, F19, W23 and W23 side-chain) and helix 2 (S46, W53, T55 and W23 sidechain) are shown here at three different temperatures, 263 K (A), 277 K (B) and 298K (C). Individual and global fitting with Luz-Meiboom model (equation 5.6) are represented with solid red and dotted green curves respectively. Full set of residues are shown in figure A5 - A7 in the Appendix.

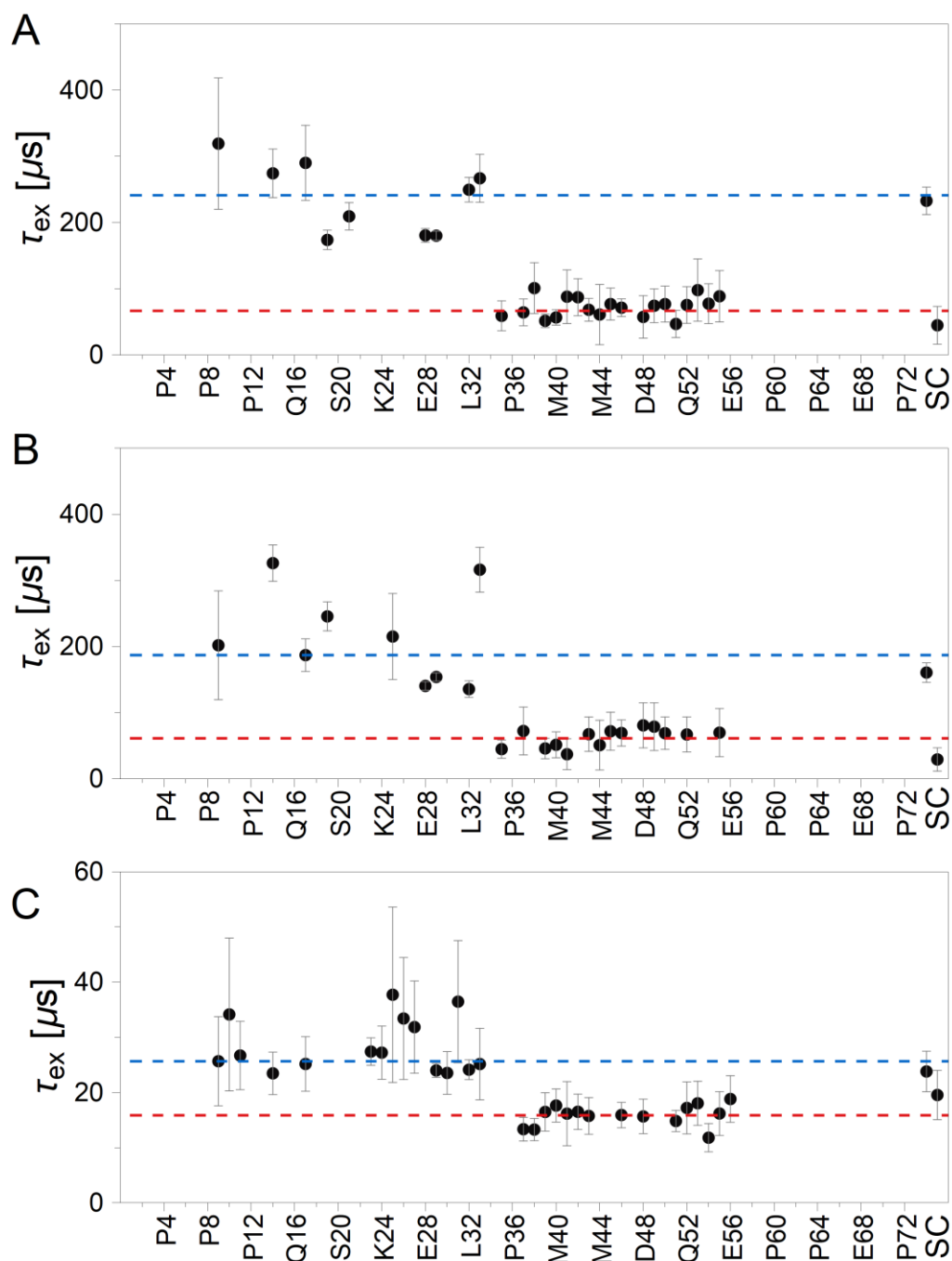


Figure 5.7: Temperature dependence of dynamics in P27A mutant of p53-TAD, obtained from ^1H E-CPMG experiment. Individually fitted lifetime (τ_{ex}) values from the fitting of dispersion profiles (RD) at 263 K (A), 277 K (B) and 298 K (C) are shown here with black dots. The global exchange value from the residues in second helical segment is indicated with red dotted line and the average lifetime of first helical segment is shown with blue dotted line in each of the three temperatures.

side-chain indole ring of amino acid W23. RD from the backbone of residues in helix-1 and W23 side-chain could be globally fitted to a single lifetime of $379.1 \pm 45.9 \mu\text{s}$ as indicated by the green dotted lines in RD profiles of figure 5.3. This suggests that the side-chain of W23 moves with the same timescale as the backbone of this segment and could be involved in the exchange process. In the P27A mutant, RD was visible also in six residues in the region 38-55, which showed higher helical content in addition to the first helix region. The global exchange lifetime ($\sim 100 \mu\text{s}$) for this segment was about four times faster than the first helix. This difference in lifetime is visible in both the appearance of the RD profiles in figure 5.4 and the fitted lifetimes in figure 5.5 (A). Although, at a higher temperature (277 K), RD was detected in more residues in the first helical segment due to higher signal to noise ratio and sharper lines, no RD was found in the predicted second helix (figure 5.5 (B)). This could be due to the limited detection timescale window of ^{15}N E-CPMG. All ^{15}N RD profiles measured at 268 K, 273 K and 277 K are shown in figure A2-A4 in the Appendix along with global and individually fitted lifetimes.

To study the exchange process at higher temperature (especially in the second helix), ^1H E-CPMG RD was employed due to its ability of capturing faster motions, as already described in the previous chapters. From ^1H E-CPMG, RD could be measured from 263 K to 298 K. RD profiles at three temperatures are shown in figure 5.6 and their individual lifetime are plotted in figure 5.7. A clear separation in the timescales could be observed between two helical segments. At 298 K global timescale of exchange for the two segments were fitted to be 24.4 ± 3.1 (helix-1) and $15.9 \pm 2.3 \mu\text{s}$. The timescale of motion from these two segments are closer to each other in higher temperature. Unlike in ^{15}N RD, with ^1H , exchange was found in the side-chains of two tryptophan residues (W23 and W53). For both of these residues the timescale found in the side-chain matches with the corresponding backbone region as evident in figure 5.7. All ^1H RD profiles measured at 263 K, 277 K and 298 K are shown in figure A.5 to A.7 in the Appendix. Global exchange lifetimes found for these two segments are plotted with inverse of temperatures ($1/T$) in figure 5.8 in blue (helix-1) and red (helix-2). Activation energy found for the exchange process in helix-1 is larger than what is found in helix-2. It is clear from the plot that global timescales from helix-1 and helix-2 region approached each other at higher temperature and become indistinguishable at 310 K.

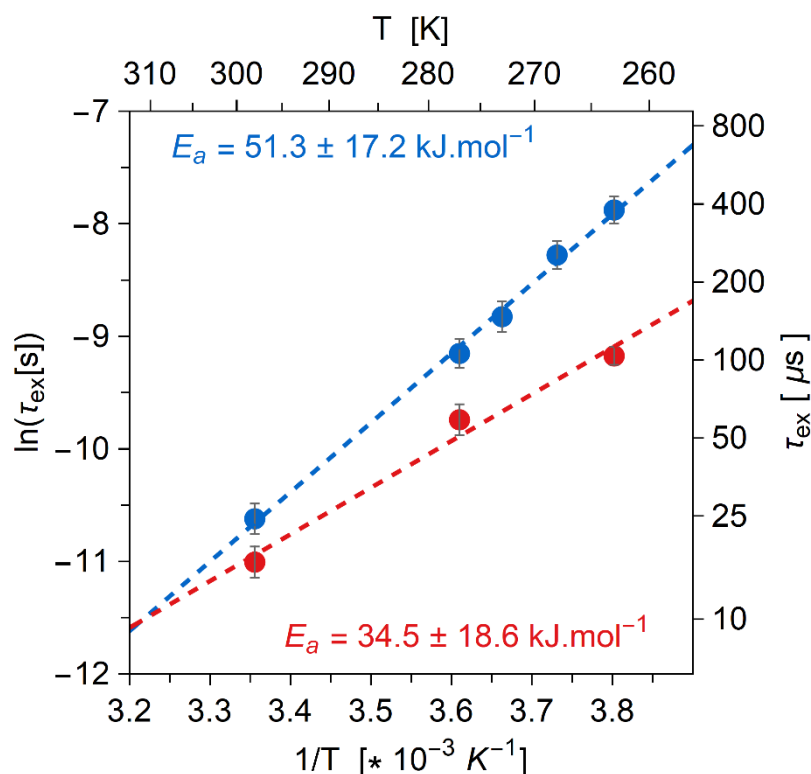


Figure 5.8: Temperature dependence of exchange processes observed at helix-1 and helix-2. Lifetimes obtained with global fitting of RD profiles from residues predicted to be in helix-1 (blue) and helix-2 (red) conformations are shown here with colored dots. Dashed lines of corresponding colors indicated the Arrhenius fitting for both helices with equation 5.3. Fitted activation energies are shown in the plot with corresponding colors.

5.2.3 Removal of the Hydrophobic Patch (F19, W23) in the Core of Helix-1

In the binding of p53-TAD with MDM2, the hydrophobic patch formed by residue F19 and W23 in the center of helix-1 found to play an important role (Kussie et al., 1996). These residues were also shown to be preserved across different species (Borchers et al., 2014). To understand the importance of these residues for the formation of the transient helix we made a mutation replacing both F19 and W23 by alanine. This mutant showed a twofold decrease in the helical propensities (15 %) of the residues in the first helical region compared to wild type p53-TAD (figure 5.2). Interestingly, no exchange process could be detected in this mutant from RD. In another mutant, in addition to the hydrophobic patch, we have also replaced the proline residue (P27) at the C-terminal of the first helix. Although this mutant shows a similar SSP score as the wild type protein, no RD was observed in this mutant too.

5.3 Conclusion

In this chapter, by using high power $R_{1\rho}$ relaxation dispersion (RD) technique, for the first time we could observe conformational exchange in p53-TAD in its free form. At 263 K, the global timescale of motion was found to be $\sim 4 \mu\text{s}$. This is, to our knowledge the fastest motion ever detected by any RD technique (CPMG and $R_{1\rho}$). From the temperature dependence of the observed exchange process in the wild type protein at a narrow temperature window (262-265 K), the lifetime of exchange at room temperature was extrapolated to be ~ 90 ns. SSP score calculated from the experimental chemical shifts for the wild type TAD shows elevated helical propensities ($\sim 30\%$) in the region where RD was observed. This suggests that in free form p53-TAD could be existing as an ensemble where the residues in the region F19-N30 find themselves in both helical and random coil conformations. In the P27A mutant, a reduction of 60-100 fold in the lifetime of conformational exchange in the helix-1 region was found from both ^1H and ^{15}N E-CPMG RD profiles. In addition to the backbone, exchange processes were also detected in the side-chain of both W23 and W53. The timescales of motions observed in the side-chains matches with the corresponding backbone regions from helix-1 and helix-2, respectively. This links the hydrophobic collapse of the side-chains with the observed global process of helix formation. A two-fold increase in the helical propensities of helix-1 region was found from the SSP scores of this mutant. This proves the higher helical content and conformational exchange in the P27A mutant, which could lead to its stronger binding affinity for MDM2, as found by ITC measurements (Borchers et al., 2014). Although in an ongoing NMR investigation, we have found weaker binding affinity of this mutant compared to the wild type, which could be due to the presence of another binding site in the second helical region of p53-TAD leading to a different recognition mechanism. In spite of having similar helical content from SSP score, the triple mutant (F19A, W23A, P27A) did not show RD. Since the chemical shift changes of protons are induced by the ring current effects of aromatic amino acids, the removal of those might also reduce the chemical shift variance of the protons such that they are undetectable. In the double mutant (F19A, W23A) both the lower population of helix and decreased $\Delta\omega$ could hinder the detection of conformational exchange. In addition to the above-mentioned factors, in both the mutant lacking the hydrophobic-core, the timescale of motion could be much faster than the wild type, shifting it to the still undetectable timescale window of RD. In summary, this work demonstrated the importance of both the hydrophobic core in the center of the first

helix and the proline residue at the C-terminal of this helix. All of these three (F19, W23 and P27) residues are preserved in p53-TAD across different species, carrying important role for the function of the protein. Application of the followed high power method in other IDPs could also discover hidden dynamics that may help to gain significant insight into their mechanism of action.

5.4 Materials and Methods

5.4.1 Sample Preparation

Perdeuterated ^{15}N -labeled p53 TAD (1-73) samples were expressed in *E. coli* adapted to 100% D_2O Toronto minimal medium supplemented with D_7 -glucose as the carbon source and ^{15}N - NH_4Cl as the nitrogen source. Recombinant p53 TAD was purified as described before (Lee et al., 2000). NMR experiments were performed on a 1.5 mM p53 TAD sample in 50 mM sodium acetate buffer at pH 6.3, containing 50 mM sodium chloride and 0.03% sodium azide. Backbone amide ^1H Off-resonance $R_{1\rho}$ relaxation dispersion ($R_{1\rho}$ -RD) experiments at temperatures ranging from 262 K to 265 K were carried out in capillary tubes to produce super-cooled conditions below the freezing point of water. Each glass capillary of 1 mm outer diameter (Wilmad, Buena, New Jersey) contained 25 μl of the p53 TAD sample and 12 such capillaries were placed inside a 5 mm NMR sample tube. The sample was purposefully not labeled with ^{13}C nuclei to avoid the necessity of ^{13}C decoupling, which could be an extra source for RF heating. In addition, the heteronuclear J coupling of $\text{C}\alpha$ and carbonyl carbon to the nearby amide proton and nitrogen nuclei can be a source of artifact in relaxation dispersion profiles.

5.4.2 NMR Experiments

All NMR measurements were performed in a Bruker Avance III HD spectrometer operating at ^1H Larmor Frequency of 700 MHz (14.1 T) and 950 MHz (22.3 T). Backbone amide proton $R_{1\rho}$ measurements were performed at 262 K, 265 K, 269 K and 275 K. For reaching the supercooled conditions, the sample temperature was lowered slowly (0.5 K / min) to avoid freezing of the liquid sample. A high VT gas flow of 1070 liter/hour was used for achieving better dissipation of heat generated by high power RF pulses. Heavy ceramic

spinner (sample holder) was necessary to avoid wobbling of the sample by the high gas flow rate.

Each two dimensional plane corresponding to a particular spin-lock power and delay was recorded with 64 complex points in the indirect dimension ($t_{1,\max} = 31$ ms) and 512 complex points in the direct dimension ($t_{2,\max} = 65.5$ ms); 4 scans were performed for each FID. The recycle delay (d_1) was set to 3 seconds for better heat dissipation and to protect the integrity of both the probe and amplifiers. The pulse program for off-resonance $R_{1\rho}$ measurement was written following the work published previously (Eichmuller & Skrynnikov, 2005) and provided in the appendix. The spin-lock power was varied between 1 kHz and 25 kHz during the measurement to obtain effective transverse relaxation rates at different RF field. The average tilt angle was kept at 35.3° ($\tan^{-1}[1/\sqrt{2}]$) to minimize the pseudo-dispersion effects caused by NOE and ROE transfers. This was achieved by choosing proper spin-lock carrier offset relative to the center of amide region (8 ppm). The off-resonance approach helped us to achieve higher maximum effective RF field of 350,000 rad/s, which can detect single digit microsecond motion (3.4 μ s). All the spins under investigation were aligned with the off-resonance spin-lock field by applying adiabatic RF pulse of 100 kHz sweep width phase and amplitude modulation. Effective transverse relaxation rates at each spin-lock power was measured by varying the spin-lock delay from 2 ms to 125 ms. To achieve homogeneous heat distribution all measurements were performed in interleaved fashion.

5.4.3 Data Analysis

The scan interleaved RD data was divided and then co-added using a home-built perl script to generate multiple .ser files corresponding to every spin-lock power and delay. The raw data was then processed with NMRpipe (Delaglio et al., 1995) software. All processed 2D planes were loaded to Computer-Aided Resonance Assignment (CARA) as .ft2 format and the intensities were extracted with a peak tolerance of 10% in both dimensions to take care of minor peak shifts. At every spin-lock power $R_{1\rho}$ values were calculated by fitting the peak intensities from spectra corresponding to spin-lock delay of 2, 45, 90 and 125 ms with the following equation

$$I_t = I_0[\exp(-R_{1\rho}t)]. \quad 5.1$$

The uncertainties of fitted $R_{1\rho}$ values were estimated from residuals of the four fitted points. Effective $R_{1\rho}$ values and effective spin-lock power were then calculated following a

previously described method (Eichmuller & Skrynnikov, 2005). RD profiles measured at all four temperatures were fitted to the following equation

$$\frac{R_{1\rho}}{\sin^2\theta} = R_{2,0} + \frac{\Phi_{ex}\tau_{ex}}{(1 + \tau_{ex}^2 \omega_{eff}^2)}. \quad 5.2$$

Where θ is the tilt angle of every spins appearing at a particular resonance frequency, Φ_{ex} is the population weighted chemical shift variance, τ_{ex} is the lifetime of exchange process and ω_{eff} is the effective spin-lock field. The fitting was done using the NonLinearModelFit function in Mathematica software. Uncertainties of the fitted parameters were estimated by “ParametersError” property of the NonLinearModelFit function. R_2 and Φ_{ex} values were local to each residues even when all residues were fitted to a single global lifetime value at a particular temperature. The lifetimes (τ_{ex}) obtained from the above-mentioned procedure were used for the Arrhenius fitting with the following equation

$$\ln(\tau_{ex}) = -\ln(A) + \left(\frac{E_a}{R}\right)\left(\frac{1}{T}\right), \quad 5.3$$

where A is attempt frequency, E_a is activation energy and R is the universal gas constant.

For CPMG RD data analysis, the extracted intensities from different 2D planes were used to calculate $R_{2,eff}$ values at different refocusing frequencies with the following equation;

$$R_{2,eff} = \frac{1}{\Delta t} \ln \frac{I_{ref}}{I_{CPMG}} \quad 5.4$$

Where, Δt is the length of CPMG delay (20 ms), I_{ref} is the intensity from reference experiment, where the CPMG block was omitted, I_{CPMG} is the intensity from CPMG measurement with a particular CPMG refocusing frequency. The uncertainties of intensities were calculated by repeating three refocusing CPMG frequencies and their standard deviation was used to calculate the root-mean-square-deviation (RMSD) for every peak with the following equation

$$\Delta R_{2,eff} = \sqrt{(R_{2,eff}^{repeat 1} - R_{2,eff}^{repeat 2})^2} \quad 5.5$$

Relaxation dispersion profiles were fitted to the Luz-Meiboom model (Luz & Meiboom, 1963) as described by the following equation

$$R_{2,eff} = R_{2,0} + \frac{4\pi^2 B_0^2 \Phi_{ex}}{k_{ex}} \left(1 - \frac{4\nu_{CPMG}}{k_{ex}} \tanh\left(\frac{k_{ex}}{4\nu_{CPMG}}\right) \right), \quad 5.6$$

6 Conclusion and Outlook

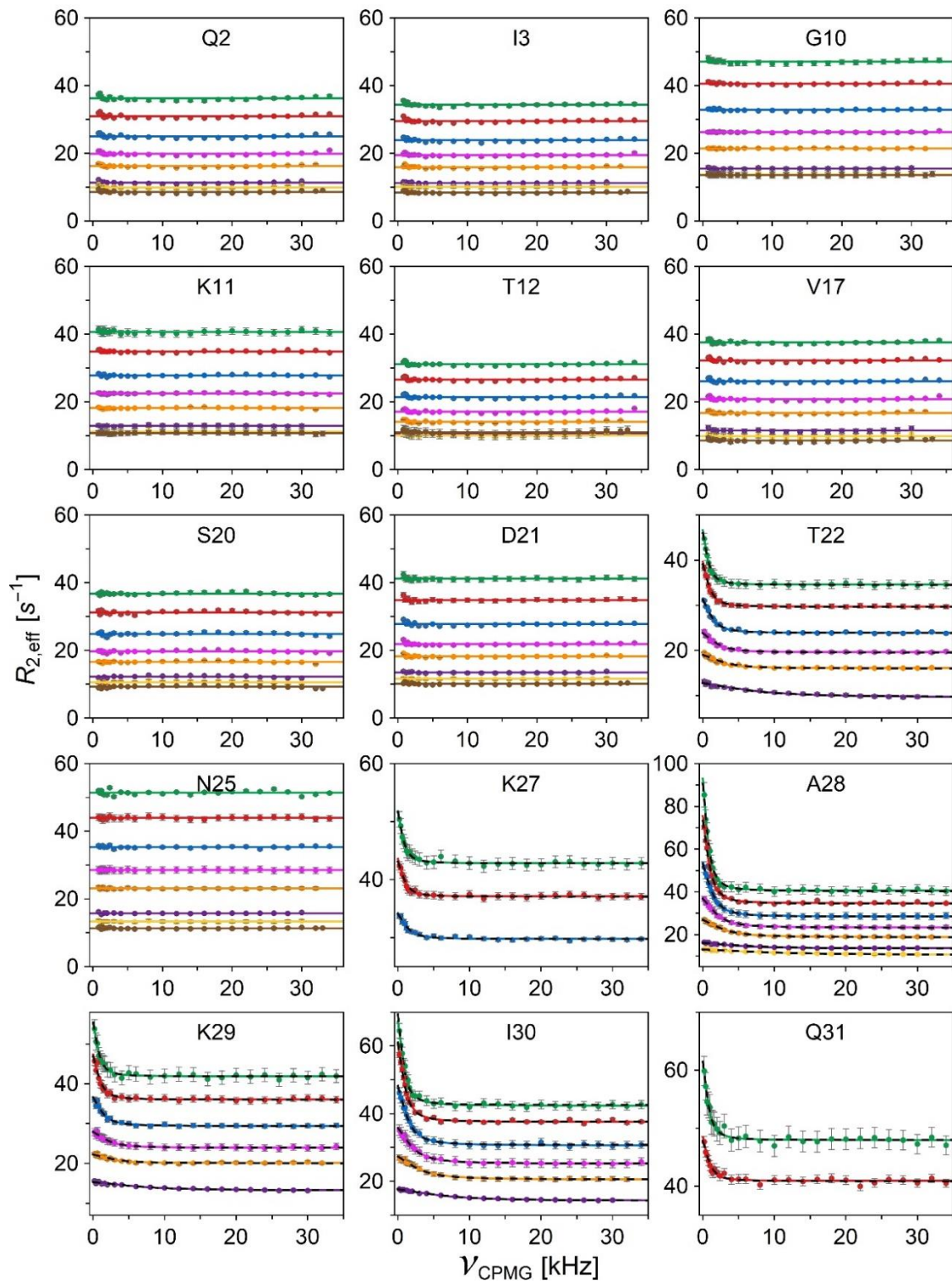
Aiming at narrowing down the invisible supra- τ_c window of protein dynamics, we have made significant progress, which is described in this dissertation. Using all commonly observed nuclei in protein NMR (^{15}N , ^{13}C and ^1H) we have exceeded the existing kinetic limit of detection by accessing faster dynamics. This was made possible with high power relaxation dispersion (CPMG and $R_{1\rho}$) by combining the advancement in hardware with smart design of pulse programs. While performing on-resonance $R_{1\rho}$ experiments we have realized the time-consuming nature of this powerful method, which puts a restriction on measuring RD of only selected residues that are likely to show conformational exchange. As a solution to this problem we have proposed the robust E-CPMG approach, which offers time-efficient detection of dynamics covering the timescale window of both conventional CPMG and $R_{1\rho}$. Furthermore, we have found the presence of a linear decay in CPMG RD profiles arising from a very commonly used phase cycle, and proposed a method for correcting this additional decay.

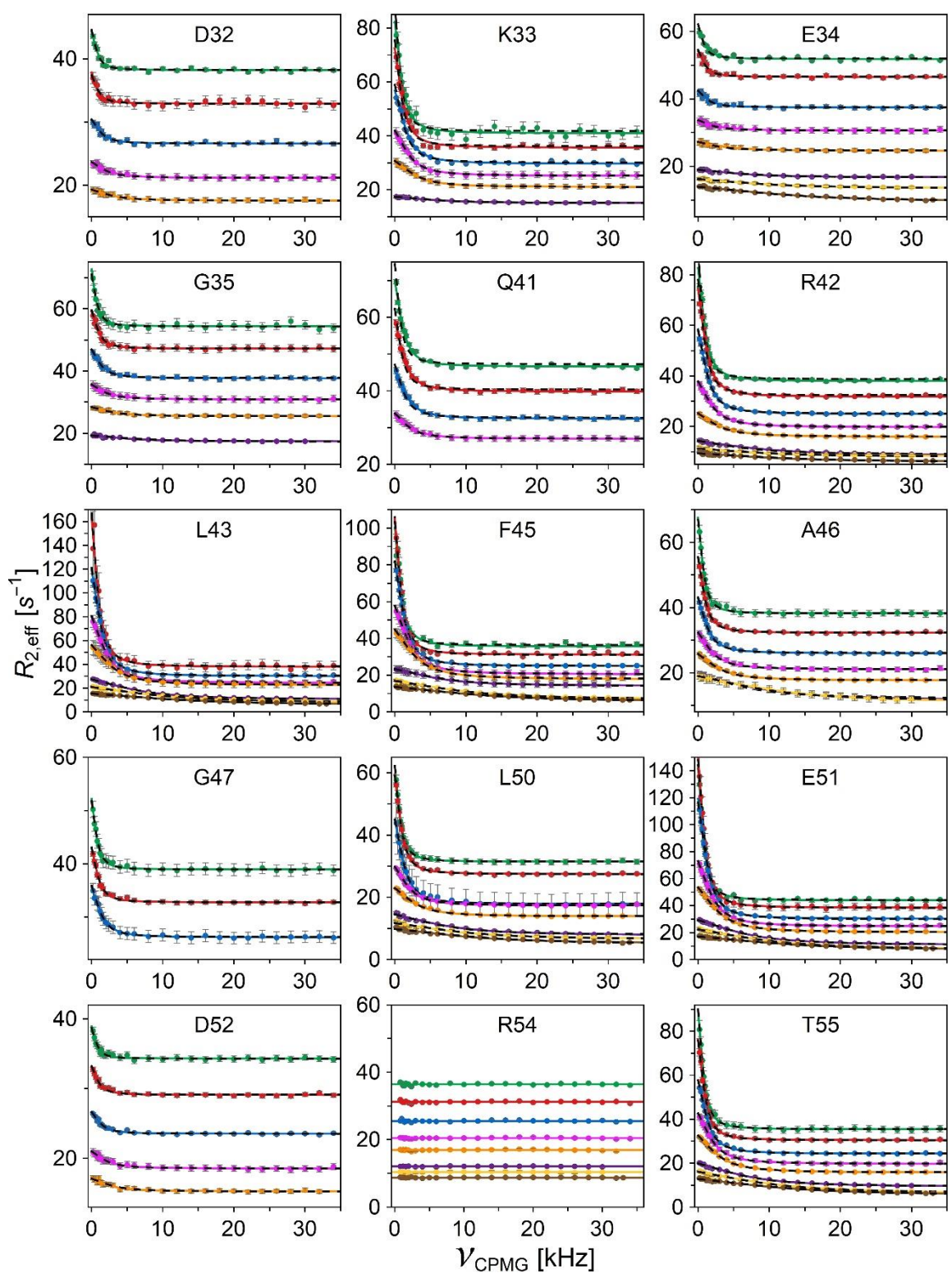
Applying this newly developed technique, we have found functionally relevant hidden supra- τ_c dynamics in the backbone and side-chains of three very well studied proteins: GB3, ubiquitin and p53-TAD. In GB3, we found a global motion in the first β -turn, which is linked to its antibody recognition. In addition to finding the involvement of more residues of ubiquitin in the peptide-flip motion, we have directly detected the high-amplitude pincer-mode motion for the first time. This newly detected mode of motion has already been predicted to contribute in the conformational adaption of ubiquitin while binding to other proteins. By studying the side-chain dynamics in mutants of ubiquitin, we could link its origin to motion happening in the backbone. As a consequence of this finding we proposed the idea of extrapolating the side-chain dynamics to the backbone in large macromolecules complexes, where backbone resonances are difficult to observe. Employing the same high-power RD, we found a very fast transient helix formation in the intrinsically disordered TAD domain of p53. The same stretch of residues where the helix is found is known to be involved in binding with MDM2 in tumor suppression during cancer progression.

The invisible supra- τ_c window spans across four orders of magnitude in timescale (~ 4 ns-40 μ s). The newly found dynamics mentioned above could be discovered by making one order of magnitude of this window (~ 4 μ s-40 μ s) visible. One can imagine how impactful the closing of the whole supra- τ_c gap will be. We are already working towards that goal and made significant progress. To achieve this goal we are developing a probe that can generate 300 kHz of B_1 field, which together with the supercooling approach can make the entire supra- τ_c window accessible by directly detecting dynamics as fast as 4 ns. The successful development of this probe will also extend the high-power RD method to challenging proteins that are stable only at lower concentrations.

7 Appendix

7.1 Figures and Tables





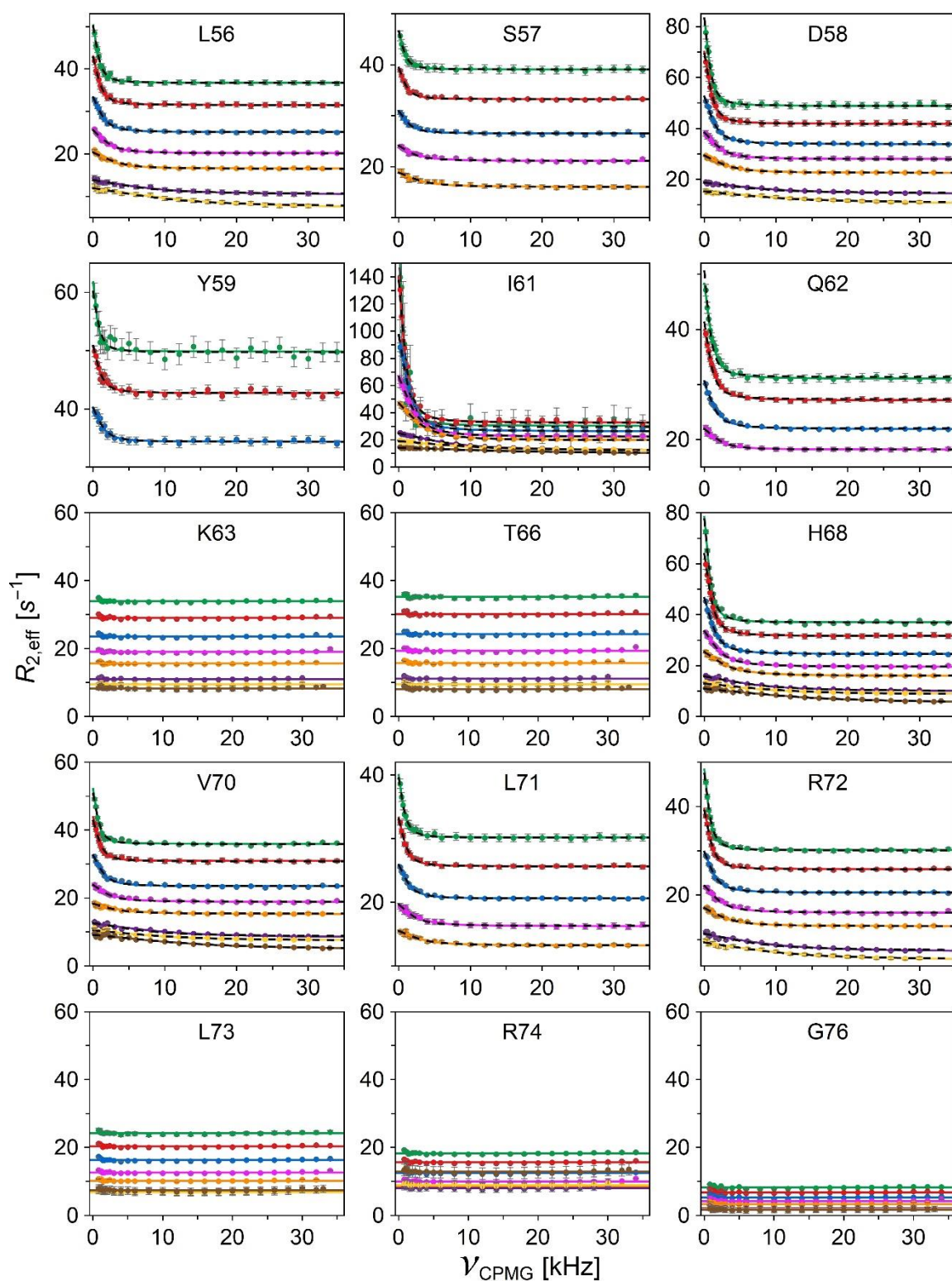


Figure A1: Backbone amide ^1H E-CPMG RD profiles of ubiquitin, showing peptide-flip timescale at different temperatures. Colored red dots and the solid colored lines indicated the measured $R_{2,\text{eff}}$ and individual fitting curves at 260 K (green), 263 K (red), 267 K (blue), 272 K (magenta), 277 K (orange), 287 K (purple), 292 K (yellow) and 298 K (brown). Black dashed line represents the globally fitted curves at each temperature.

Table A.1: Individual and global exchange lifetime of peptide flip motion at different temperatures.

Res	260 K	263 K	267 K	272 K	277 K	287 K	292 K	298 K
Global	187.9 ± 19.1	151.5 ± 19.2	109.1 ± 12.4	71.7 ± 14.4	50.3 ± 11.4	22.1 ± 6.7	15.4 ± 3.8	12.0 ± 2.7
T14	186.1 ± 37.2	152.1 ± 32.4	100.5 ± 26.1	47.3 ± 15.8	41.5 ± 17.2	16.2 ± 5.9	12.1 ± 4.3	-
L15	183.2 ± 41.4	137.2 ± 29.5	81.4 ± 19.1	55.2 ± 18.4	48.5 ± 20.2	29.9 ± 17.2	16.0 ± 6.0	-
E18	202.3 ± 36.7	145.5 ± 32.3	127.4 ± 35.2	-	-	-	-	-
T22	205.4 ± 22.7	169.7 ± 20.9	117.9 ± 17.2	93.3 ± 21.7	72.8 ± 23.8	19.8 ± 8.4	-	-
I23	213.9 ± 4.1	167.0 ± 3.4	114.1 ± 3.2	71.8 ± 3.0	49.1 ± 3.1	25.2 ± 3.7	17.4 ± 3.1	12.2 ± 2.5
K27	194.0 ± 28.1	175.6 ± 33.8	118.2 ± 29.6	-	-	-	-	-
A28	206.1 ± 5.2	169.1 ± 5.1	115.9 ± 5.1	79.2 ± 6.1	52.6 ± 6.9	32.3 ± 14.9	16.7 ± 9.5	-
K29	189.8 ± 18.0	163.7 ± 17.5	107.7 ± 16.5	74.2 ± 19.6	67.9 ± 31.0	22.1 ± 13.4	-	-
I30	159.6 ± 7.7	143.0 ± 7.3	98.4 ± 6.4	67.0 ± 6.9	46.7 ± 7.6	23.8 ± 9.0	-	-
Q31	184.0 ± 17.4	179.7 ± 30.1	-	-	-	-	-	-
D32	171.5 ± 34.9	179.4 ± 45.9	105.4 ± 30.7	61.3 ± 27.1	49.6 ± 31.0	-	-	-
K33	139.6 ± 3.9	125.4 ± 3.9	89.4 ± 3.6	70.6 ± 4.5	51.2 ± 5.7	25.2 ± 13.5	-	-
E34	137.0 ± 17.7	134.6 ± 20.3	91.6 ± 21.1	51.9 ± 19.4	34.2 ± 15.3	24.1 ± 13.6	16.9 ± 8.6	11.2 ± 3.6
G35	224.8 ± 17.1	142.1 ± 13.7	95.9 ± 11.8	63.0 ± 14.7	46.3 ± 17.7	29.9 ± 18.9	-	-
Q40	178.8 ± 11.1	153.4 ± 11.3	112.7 ± 12.8	71.2 ± 19.2	-	-	-	-
Q41	125.5 ± 6.1	106.4 ± 6.0	86.4 ± 6.9	64.2 ± 10.3	55.8 ± 18.7	-	-	-
R42	143.8 ± 3.7	126.6 ± 3.4	103.5 ± 3.5	66.9 ± 4.0	44.0 ± 5.3	16.4 ± 4.1	19.9 ± 8.7	14.3 ± 5.5
L43	-	143.8 ± 1.3	105.7 ± 1.3	70.2 ± 1.4	50.1 ± 1.6	23.0 ± 1.7	16.0 ± 1.7	11.6 ± 1.7
I44	217.5 ± 41.6	147.8 ± 29.5	108.6 ± 27.5	62.2 ± 20.6	41.7 ± 18.1	14.4 ± 5.4	16.9 ± 7.3	10.4 ± 3.5
F45	158.1 ± 2.9	158.5 ± 2.6	109.5 ± 2.1	70.3 ± 2.0	47.0 ± 1.9	25.4 ± 3.5	15.3 ± 2.2	12.2 ± 2.1
A46	195.9 ± 8.7	146.3 ± 7.5	102.6 ± 6.7	66.1 ± 6.4	47.7 ± 6.5	16.2 ± 2.9	12.7 ± 2.5	-
G47	201.0 ± 19.9	151.9 ± 17.4	101.4 ± 11.8	-	-	-	-	-
K48	186.8 ± 29.7	145.9 ± 24.7	101.9 ± 20.7	83.6 ± 28.4	70.4 ± 36.1	20.3 ± 11.4	17.8 ± 11.1	-
Q49	-	139.3 ± 41.4	97.5 ± 31.3	53.0 ± 21.0	43.8 ± 20.6	19.7 ± 8.7	13.7 ± 5.0	-
L50	186.9 ± 7.8	155.8 ± 5.8	108.7 ± 4.4	73.3 ± 6.3	49.5 ± 5.9	20.1 ± 4.0	17.3 ± 4.5	14.5 ± 3.9
E51	179.1 ± 2.3	156.8 ± 1.7	117.4 ± 1.5	73.1 ± 1.6	50.9 ± 1.6	22.2 ± 1.5	15.2 ± 1.5	12.1 ± 1.7
D52	208.3 ± 60.6	133.5 ± 39.1	110.2 ± 39.0	64.4 ± 29.1	59.7 ± 33.6	-	-	-
T55	182.0 ± 4.3	156.1 ± 4.1	109.0 ± 3.6	70.3 ± 3.3	49.0 ± 3.2	21.5 ± 2.6	14.4 ± 2.1	12.7 ± 2.4
L56	193.1 ± 18.4	157.9 ± 16.5	108.4 ± 14.6	82.2 ± 15.6	62.0 ± 16.6	19.2 ± 7.6	12.0 ± 4.2	-
S57	186.7 ± 31.8	151.4 ± 29.0	101.4 ± 25.9	57.7 ± 21.9	51.9 ± 19.9	-	-	-
D58	189.8 ± 7.1	160.6 ± 6.9	108.2 ± 6.4	78.2 ± 7.9	49.8 ± 7.9	17.4 ± 5.5	11.1 ± 3.9	-
Y59	242.5 ± 29.6	146.0 ± 21.4	115.1 ± 21.7	-	-	-	-	-
I61	215.5 ± 2.1	158.9 ± 1.8	108.4 ± 1.7	75.4 ± 1.8	55.3 ± 2.1	22.9 ± 2.4	18.8 ± 3.7	8.9 ± 3.5
Q62	144.3 ± 9.8	121.7 ± 10.6	93.9 ± 12.5	76.2 ± 21.3	-	-	-	-
S65	179.8 ± 41.4	149.8 ± 45.7	-	-	-	-	-	-
H68	196.2 ± 6.2	151.4 ± 5.6	110.9 ± 5.6	68.3 ± 5.3	45.9 ± 5.4	21.5 ± 4.8	19.8 ± 6.2	11.6 ± 2.9
L69	162.7 ± 29.7	138.4 ± 25.4	78.7 ± 20.3	-	-	-	-	-
V70	220.0 ± 18.8	178.2 ± 17.2	109.5 ± 13.2	60.5 ± 13.7	37.2 ± 14.3	15.9 ± 5.4	17.2 ± 7.8	12.1 ± 3.9
L71	206.7 ± 28.1	159.9 ± 25.2	105.8 ± 22.2	58.2 ± 19.5	47.5 ± 22.8	-	-	-
R72	206.6 ± 15.2	162.1 ± 14.4	111.6 ± 13.4	64.3 ± 11.6	50.4 ± 13.3	17.0 ± 5.9	14.1 ± 5.2	-

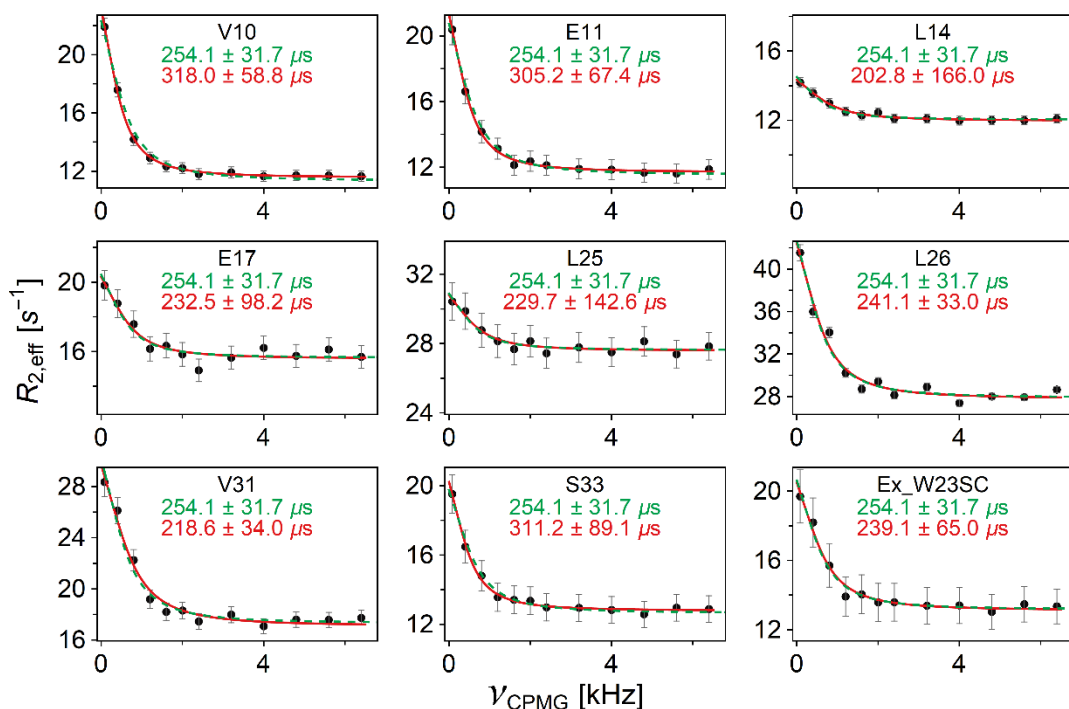


Figure A2: ^{15}N E-CPMG RD profiles of P27A mutant of p53-TAD at 268 K. Both global (green) and individual (red) fitting to equation 5.6 are shown here.

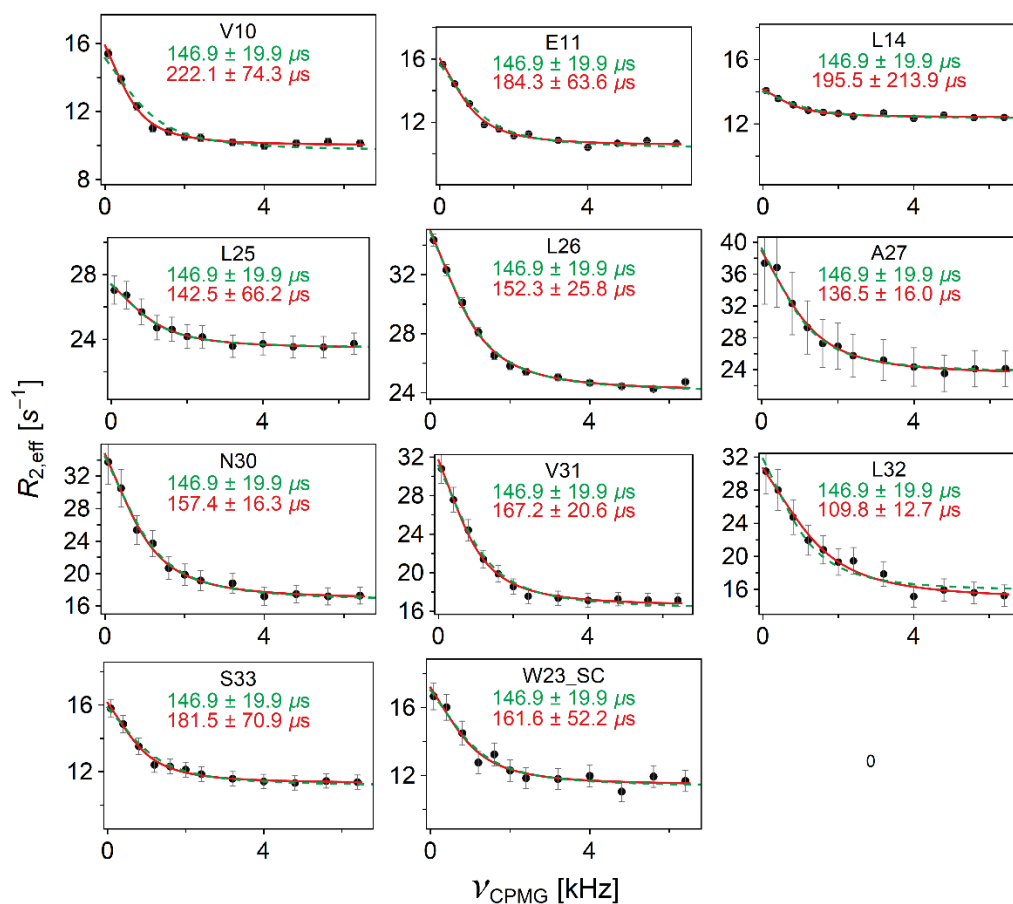


Figure A3: ^{15}N E-CPMG RD profiles of P27A mutant of p53-TAD at 273 K. Both global (green) and individual (red) fitting to equation 5.6 are shown here.

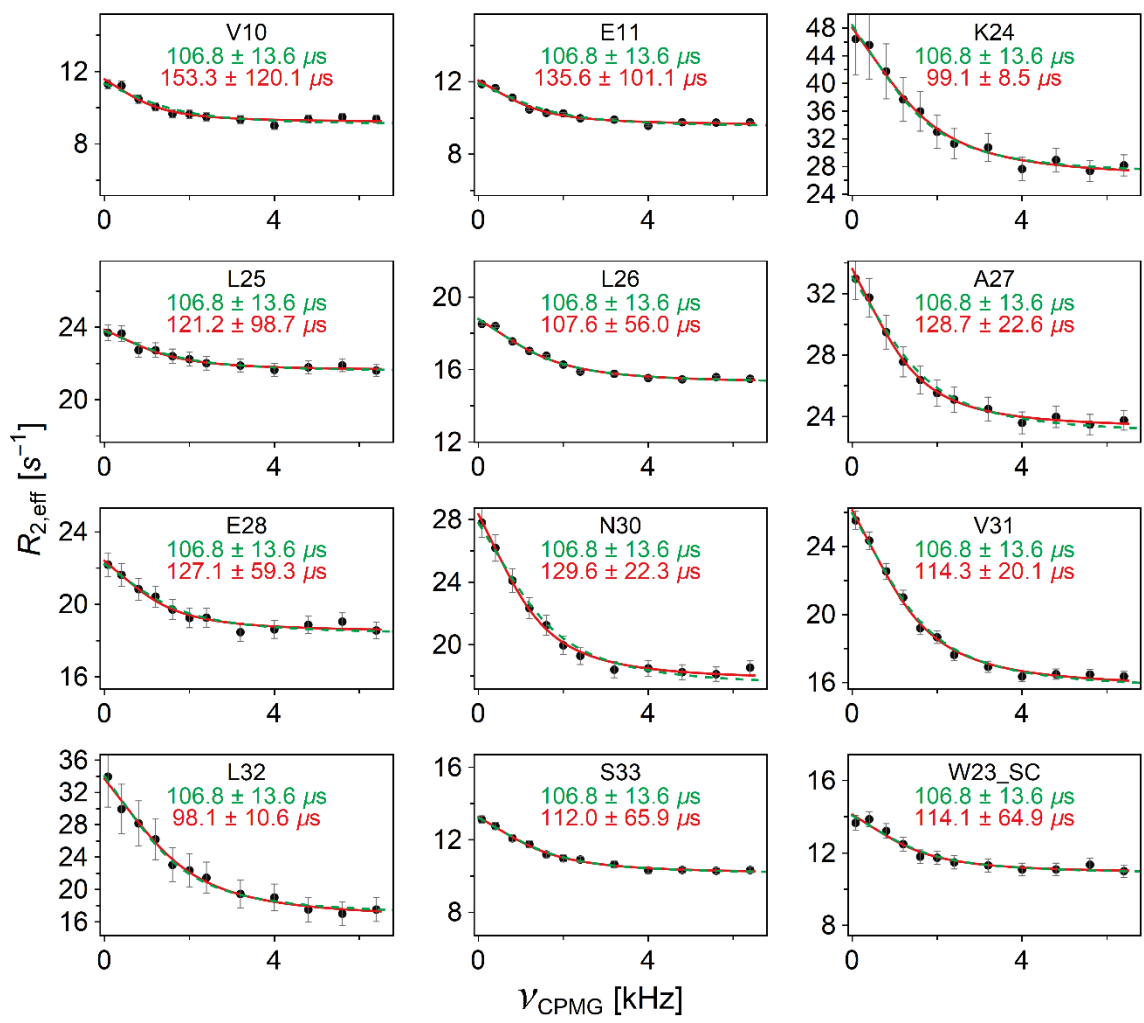


Figure A4: ^{15}N E-CPMG RD profiles of P27A mutant of p53-TAD at 277 K. Both global (green) and individual (red) fitting to equation 5.6 are shown here.

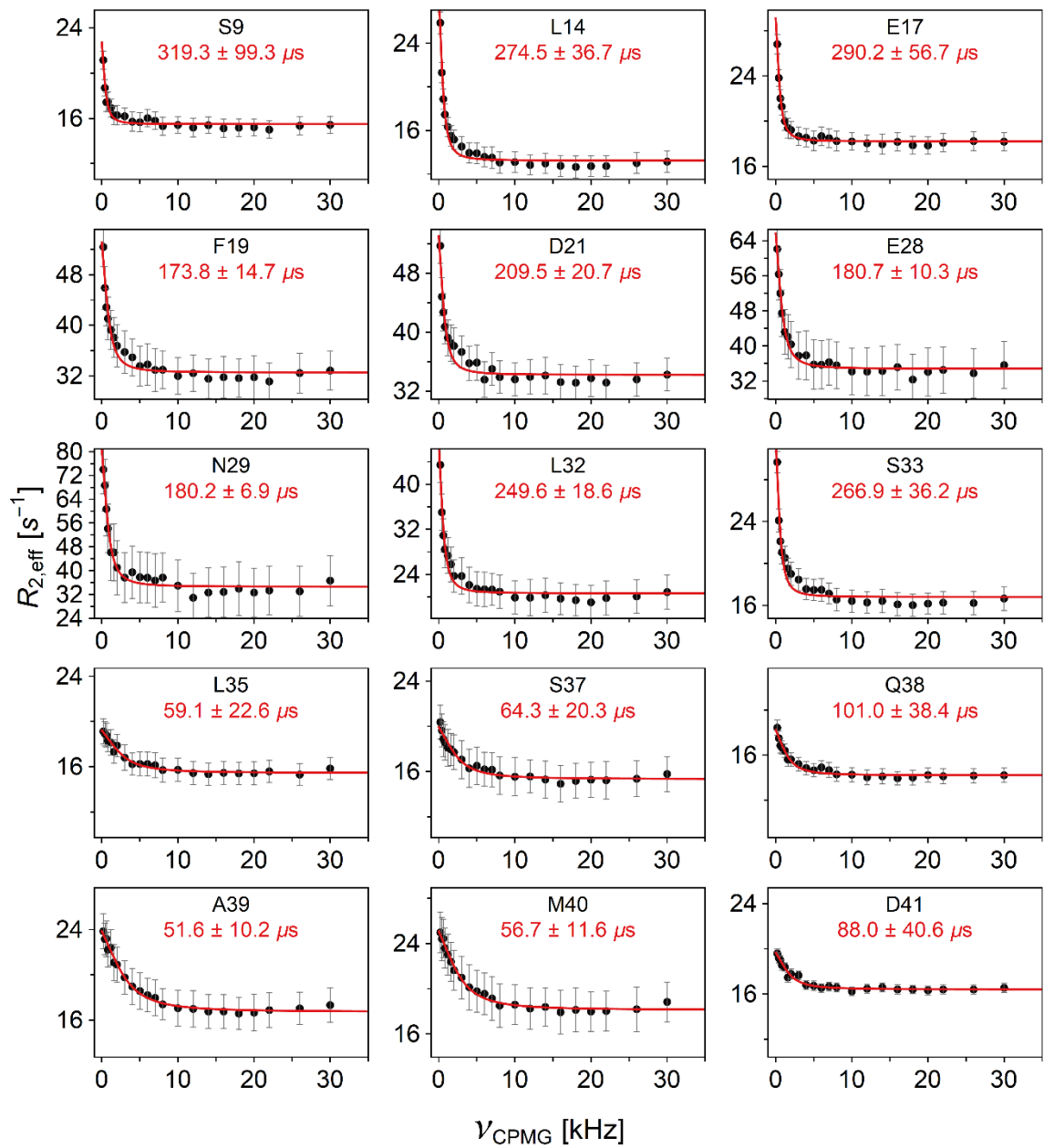


Figure continues to next page.

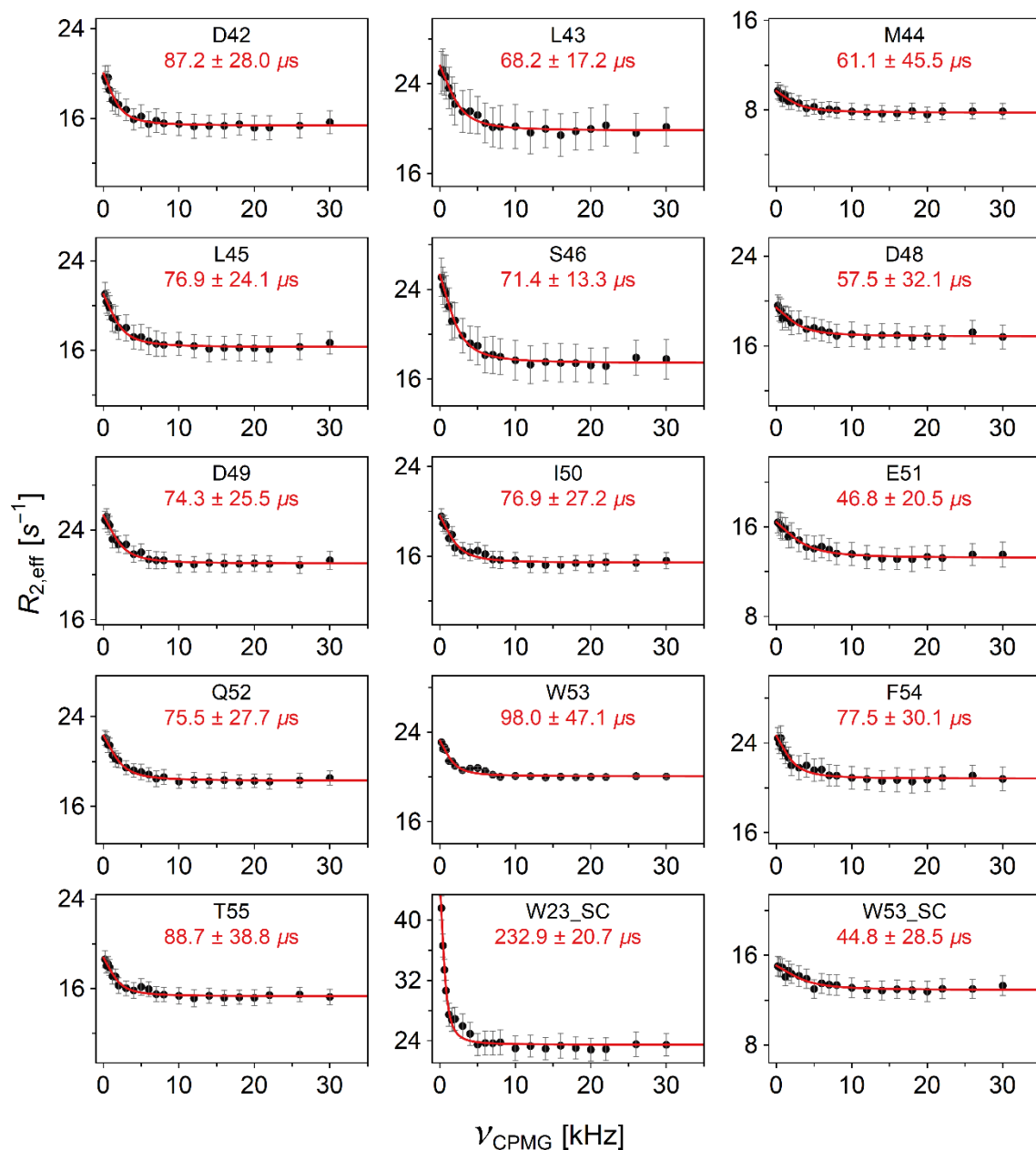


Figure A5: ^1H E-CPMG RD profiles of P27A mutant of p53-TAD at 263 K. Individual fitting to equation 5.6 and the fitted exchange lifetimes are shown here in red.

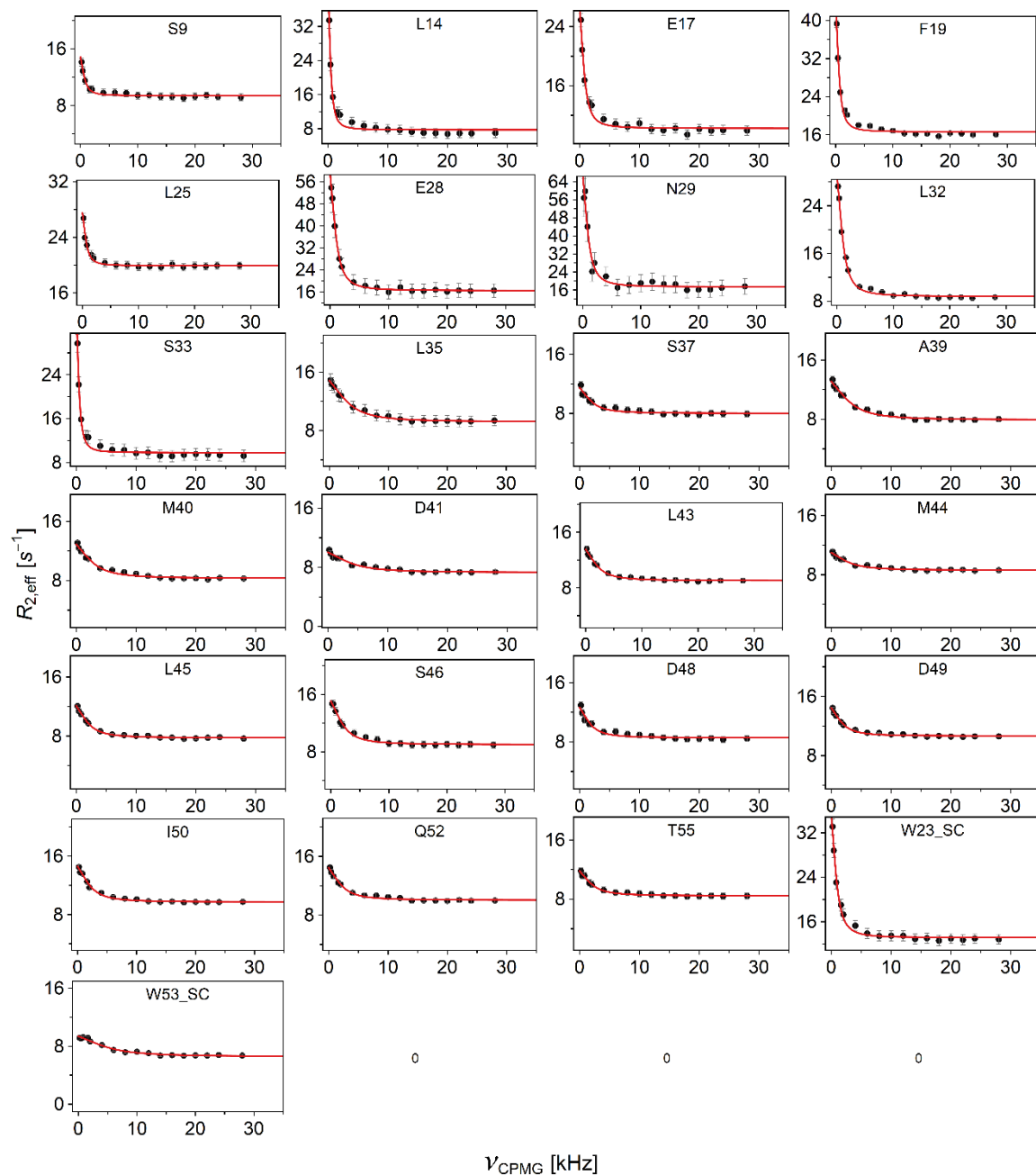


Figure A6: ^1H E-CPMG RD profiles of P27A mutant of p53-TAD at 277 K. Individual fitting to equation 5.6 is shown here in red.

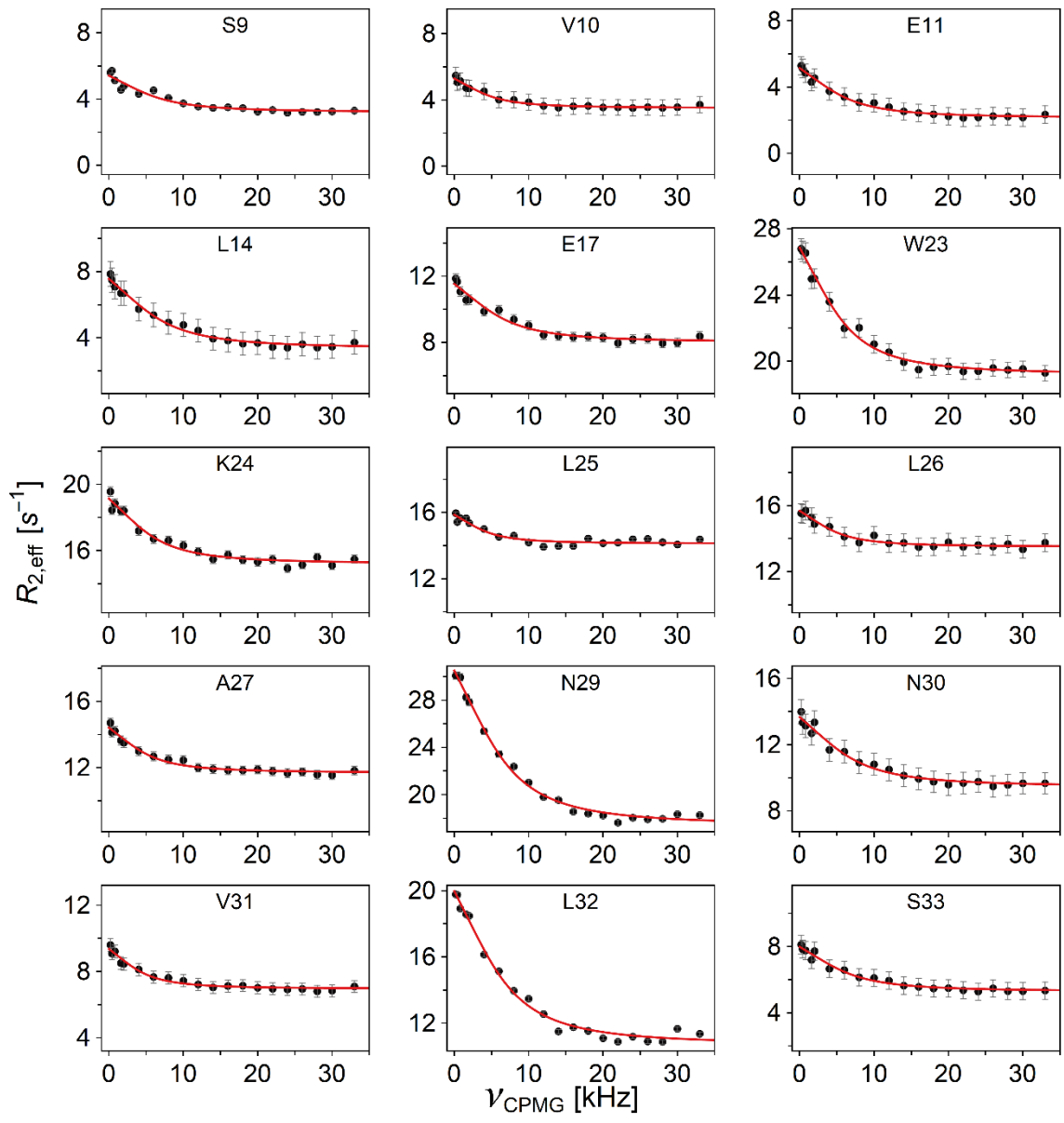


Figure continues to next page.

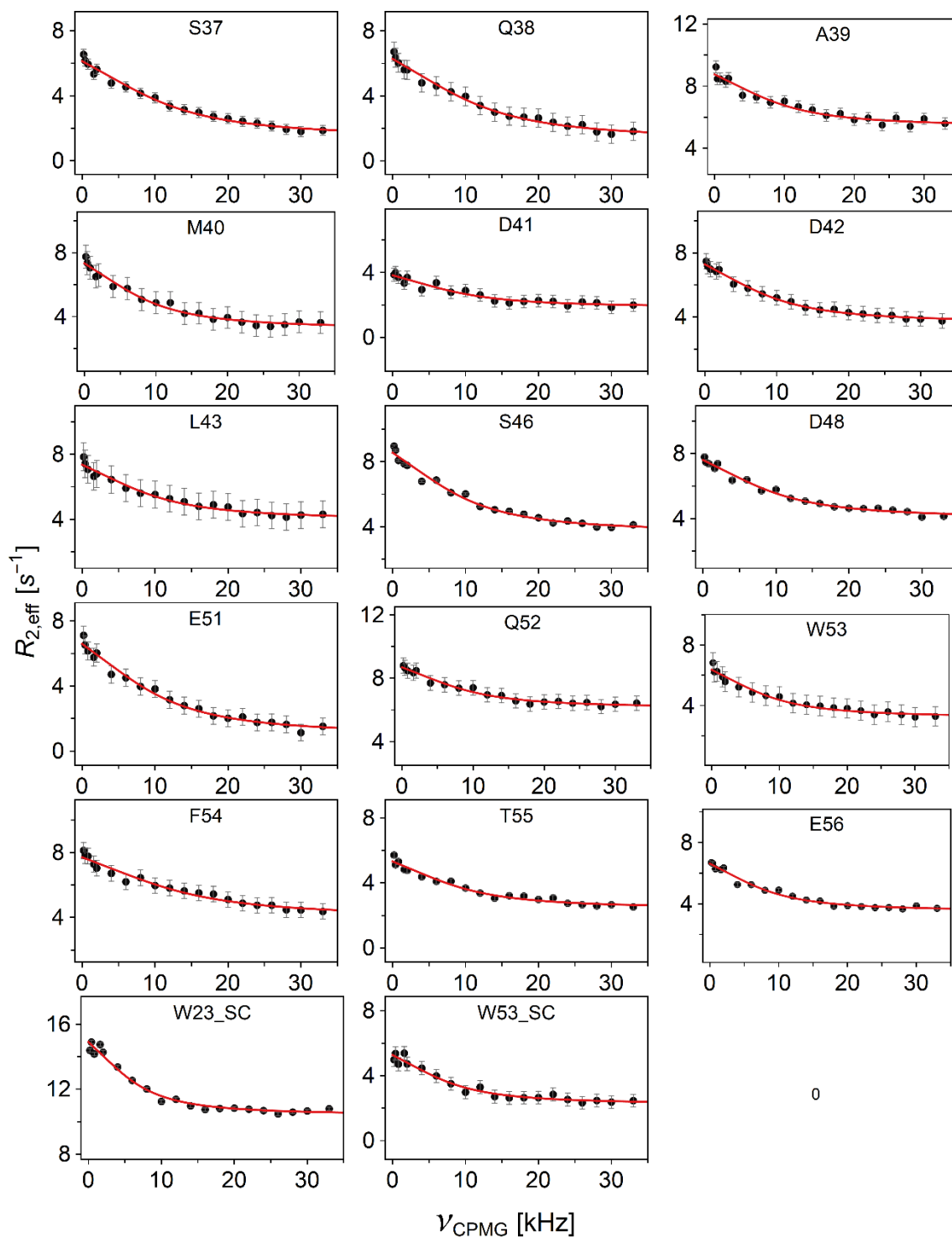


Figure A7: ^1H E-CPMG RD profiles of P27A mutant of p53-TAD at 298 K. Individual fitting to equation 5.6 is shown here in red.

7.2 Pulse Programs

The pulse programs used to record NMR data, described in this dissertation are presented here in Bruker format. Some of these pulse programs are already published in other article and thesis.

7.2.1 Backbone amide ^1H $R_{1\rho}$

```
define list<gradient> EA=<EA>
define list<power> SLPower=<SVALIST>
define list<delay> SLdelay=<SVDLIST>
define list<frequency> OFFcnst=<SFQ1LIST>
prosol relations=<triple>
#include <Avance_dl.incl>
define delay INEPT_1
define delay INEPT_2
#define GRADIENT0 10u p20:gp0 200u
#define GRADIENT1 10u p21:gp1 200u
#define GRADIENT2 10u p22:gp2 200u
#define GRADIENT3 10u p23:gp3 200u
; gradients 4-7 used in  $^{13}\text{C}$  evolution and PEP element
#define GRADIENT8 10u p28:gp8 200u

"p2=p1*2"
"p4=p3*2"
"p6=p5*2"
"in10=inf2/2"
"d10=in10/2-p1"
"d12=10u+200u+p24"
"INEPT_1=d3-(p21+210u)"
"INEPT_2=d3-(p23+210u)-10u"
"p18=p9-p17"
"acqt0=0"
baseopt_echo
aqseq 312

1 10u ze
  20m st0
  SLdelay*0.001
  10u p11:f1
2 1m
3 1m
4 1m
5 1m
  10u do:f3
  10u LOCKH_OFF
  20u
```

```

d1
;-----check calc
if "SLdelay > 0"
{
  "p17 = SLdelay"

  "p18=p9-p17"
}
10u
10u p1:f1
10u p13:f3
20u LOCKH_ON
;-----Boltzmann
(p5 ph20):f3
GRADIEN0
10m
;-----first INEPT
(p1 ph20):f1
GRADIEN1
INEPT_1
(center (p2 ph20):f1 (p6 ph20):f3)
GRADIEN1
INEPT_1
(p1 ph21):f1
GRADIEN2
;-----off-resonance spin-lock
10u fq=OFFcnst:f1
20u SLPower:f1
10u
(p15:sp15(currentpower) ph20):f1
(center (p17 ph20):f1 (p6 ph20):f3)
(p16:sp16(currentpower) ph20):f1
10u
20u
10u fq=cnst11 (bf ppm):f1
5u p18:f1
;-----CRT
;-----p18 should have zero power p18 = 120db!!!!!!!!!!!!!!
(center (p6 ph20):f3 (p18 ph20):f1)
;-----15N evolution
5u p1:f1
(p5 ph1):f3
d10
(p2 ph20):f1
d10
10u
p24:gp4*EA
200u
(p6 ph2):f3
10u

```

```

p24:gp4*-1*EA
200u
;-----PEP element
(center (p1 ph20):f1 (p5 ph4):f3)
10u
GRADIENT3
INEPT_2
(center (p2 ph20):f1 (p6 ph20):f3)
10u
GRADIENT3
INEPT_2
(center (p1 ph21):f1 (p5 ph21):f3)
10u
GRADIENT3
INEPT_2
(center (p2 ph20):f1 (p6 ph20):f3)
10u
GRADIENT3
INEPT_2
(p1 ph20):f1
d12
(p2 ph21):f1
10u
p24:gp7
200u p113:f3
;-----acquisition
goscnp ph31 cpd2:f3
10u do:f1
10u do:f2
10u do:f3
3m st SLdelay.inc
lo to 3 times l30

3m SLPower.inc
3m OFFcnst.inc
lo to 4 times l31

3m ipp1 ipp2 ipp31
lo to 5 times ns

1m mc #0 to 5

F1QF()
;F2EA(ip4*2 & rpp1 & rpp2 & rpp31 & igrad EA, ip1*2 & ip31*2 & id10)
;F2EA(calgrad(EA) & calph(ph4, +180) & exec(rppall), caldel(d10, +in10) & calph(ph2,
+180) & calph(ph31, +180))
F2EA(exec(rppall) & calph(ph4, +180) & calgrad(EA) & calph(ph2, +180) &
calph(ph31, +180), caldel(d10, +in10))

10u do:f3

```

```
10u do:f1
10m LOCKH_OFF
```

```
exit
```

```
ph1= 0 2
ph2= 0 0 1 1
ph4= 0
ph20=0
ph21=1
ph22=2
ph23=3
ph31=0 2 2 0
```

7.2.2 Side-chain ^{13}C E-CPMG

```
define delay INEPT1
define delay INEPT2
define delay INEPT3
define delay U1

#include <Avance_dl.incl>
#define GRADIENT0 10u p20:gp0 200u
#define GRADIENT1 10u p21:gp1 200u
#define GRADIENT2 10u p22:gp2 200u
#define GRADIENT3 10u p23:gp3 200u
#define GRADIENT4 10u p24:gp4 200u
#define GRADIENT5 10u p25:gp5 200u
#define GRADIENT6 10u p26:gp6 200u
#define GRADIENT7 10u p27:gp7 200u
#define GRADIENT8 10u p28:gp8 200u
;define list<delay> Clist=<${VDLIST}>
define list<loopcounter> cpmglist=<${VCLIST}>

"p2=2*p1"
"p4=2*p3"
"in0=inf2/2"
"d0=in0/2-p3*2/3.14159-p1"
"INEPT1=d2-(p21+210u)-4u"
"INEPT2=d2-(p22+210u)-4u"
"INEPT3=d2-(p23+210u)-4u"
"U1=d2-p26-210u"
"d13=d1-d8"
aqseq 312

1 10u ze
20m st0
10m LOCKDEC_ON
10u H2_PULSE
```

```

2 6m
3 3m
4 3m
  20u do:f2
  20u do:f4
  10m H2_LOCK
  10u LOCKH_OFF
  20u pl1:f1
  20u pl2:f2

  if "cpmplist > 0"
  {
    "l3=cpmplist"
    "l4=l13-l3"
    "d14=d8/(4*l3)-p3"
    "d16=d8/(4*l4)-p3"
  }
  else
  {
    "l3=0"
    "l4=l13-l3"
    "d14=p3"
    "d16=d8/(4*l4)-p3"
  }

  d13*0.5
5 d16
  (p4 ph21):f2
  d16
  d16
  (p4 ph20):f2
  d16
lo to 5 times l4
8 10u
  d13*0.5
  20u pl1:f1
  20u pl2:f2
  20u pl14:f4
  20u LOCKH_ON
;-----first INEPT
  (p3 ph20):f2
  GRADIEN0
  1m
  10u H2_PULSE
  (p1 ph20):f1
  GRADIEN1
  INEPT1
  (center(p2 ph21):f1 (p3 ph20 2u p4 ph21 2u p3 ph20):f2)
  GRADIEN1
  INEPT1

```

```

(p1 ph21):f1
GRADIENT4
(p3 ph4):f2
;-----CPMG
if "I3 ==0" goto 10
9 d14
  (p4 ph21):f2
  d14
lo to 9 times I3
;-----U element
10 GRADIENT6
  U1
  (center(p2 ph21):f1 (p3 ph20 2u p4 ph21 2u p3 ph20):f2)
  GRADIENT6
  U1
;-----CPMG
if "I3 == 0" goto 12
11 d14
  (p4 ph20):f2
  d14
lo to 11 times I3
12 (p3 ph5):f2
  GRADIENT5
  20u p14:f4
  10u cpds4:f4
;-----13C evolution
  (p3 ph1):f2
  (d0 p2 ph23 d0):f1
;-----second INEPT
  (p3 ph20):f2
  5u do:f4
  GRADIENT7
  (p3 ph21):f2
  GRADIENT2
  INEPT2
  (center(p2 ph21):f1 (p3 ph20 2u p4 ph21 2u p3 ph20):f2)
  GRADIENT2
  INEPT2
  (p3 ph20):f2
  GRADIENT8
  (p1 ph22):f1
;-----WATERGATE
  GRADIENT3
  INEPT3
  (center(p2 ph20):f1 (p3 ph20 2u p4 ph21 2u p3 ph20):f2)
  GRADIENT3
  INEPT3 p12:f2 LOCKH_OFF
;-----acquisition
  goscnp ph31 cpd2:f2

```

```

10u do:f2

3m st cpmglist.inc
lo to 3 times nbl

3m ipp1 ipp4 ipp5 ipp31
lo to 4 times ns

1m mc #0 to 4
F1QF()
F2PH(rpp1 & rpp4 & rpp5 & rpp31 & ip1,id0 & dd11)
10u do:f1
10u do:f2
10u do:f4
10m H2_LOCK
10m LOCKH_OFF
10m LOCKDEC_OFF
exit

ph1 =1 1 3 3
ph4 =0 2
ph5 =1; 1 1 1 3 3 3 3
ph31=0 2 2 0; 2 0 0 2

ph15=2
ph16=0
ph17=1
ph18=2
ph19=3

ph20=0
ph21=1
ph22=2
ph23=3

ph26=2

```

7.2.3 Backbone ¹H E-CPMG

```

prosol relations=<triple>
;#include <Avance_dl.incl>
#include <Avance.incl>

define delay INEPT_W
define delay INEPT_D
#define GRADIENT1 10u p21:gp1 200u
#define GRADIENT2 10u p22:gp2 200u
#define GRADIENT3 10u p23:gp3 200u

```

```
#define GRADIENT4 10u p24:gp4 200u
#define GRADIENT5 10u p25:gp5 190u
#define GRADIENT6 10u p26:gp6 190u
define list<loopcounter> cpmglist=<{$VCLIST}>
```

```
"p2=2*p1"
"p6=2*p5"
"in10=inf2/2"
"d10=in10/2-p5*2/3.14159"
"INEPT_D=d2-p21-210u"
"INEPT_W=d2-p24-210u"
;"l13=d8/(4*p1)"
"l13=d8/(16*p1)"
"acqt0=0"
baseopt_echo
aqseq 312
```

```
1 10m ze
  20m st0
2 1m
3 3m
4 3m do:f3
  20u
  if "cpmglist < l13"
  {
    if "cpmglist > 0"
    {
      "l3 = cpmglist"
      "d14=d8/(16*l3)-p1"
    }
    else
    {
      "l3=0"
      "d14=p1"
    }
  }
  else
  {
    "l3=l13"
    "d14=p1"
  }
  d1 p1:f1
  20u p2:f2
  20u p3:f3
  20u LOCKH_ON
;-----first INEPT
(p1 ph20):f1
  GRADIENT1
  INEPT_D
  (center(p2 ph21):f1 (p6 ph1):f3)
```

```

GRADIANT1
INEPT_D
(p1 ph21):f1
GRADIANT2
;-----15N evolution
  (refalign (p5 ph1 d10 d10 p5 ph20):f3 center (p3 ph23 1.5u p4 ph20 1.5u p3 ph23):f2
center(p2 ph23):f1)
  GRADIANT3
;-----second INEPT
  (p1 ph2):f1
if "I3 == 0" goto 7
if "I3 == I13" goto 6

5 d14
  (p2 ph21):f1
  d14
  d14
  (p2 ph21):f1
  d14
  d14
  (p2 ph20):f1
  d14
  d14
  (p2 ph22):f1
  d14
lo to 5 times I3

goto 7

6 (p2 ph21):f1
  (p2 ph21):f1
  (p2 ph20):f1
  (p2 ph22):f1
lo to 6 times I13

7 GRADIANT4
  INEPT_W
  (center(p2 ph21):f1 (p6 ph1):f3)
  GRADIANT4
  INEPT_W

if "I3 == 0" goto 10
if "I3 == I13" goto 9

8 d14
  (p2 ph20):f1
  d14
  d14
  (p2 ph20):f1
  d14

```

```

d14
(p2 ph21):f1
d14
d14
(p2 ph23):f1
d14
lo to 8 times l3

goto 10

9 (p2 ph20):f1
(p2 ph20):f1
(p2 ph21):f1
(p2 ph23):f1
lo to 9 times l13

;10 (p1 ph3):f1
10 (p1 ph21):f1
GRADIENT5
; (p1 ph23):f1
(p1 ph3):f1
GRADIENT6
10u
(p1*0.2308 ph21):f1
d5
(p1*0.6923 ph21):f1
d5
(p1*1.4615 ph21):f1
d5
(p1*1.4615 ph23):f1
d5
(p1*0.6923 ph23):f1
d5
(p1*0.2308 ph23):f1
GRADIENT6
10u pl13:f3 LOCKH_OFF

;-----acquisition
goscnp ph31 cpd3:f3
3m do:f3
3m st cpmglist.inc
lo to 3 times nbl

3m cpmglist.res
3m ipp1 ipp2 ipp3 ipp31
lo to 4 times ns

; go=2 ph31 cpd3:f3
; 1m do:f3 mc #0 to 2 F1PH(ip1,id0)
1m mc #0 to 4

```

```
F1QF()
;F2PH(ip1 & rpp1 & rpp2 & rpp3 & rpp31,id10)
F2PH(calph(ph1, +90) & exec(rppall), caldel(d10, +in10))
```

```
10u do:f1
10u do:f2
10u do:f3
10u LOCKH_OFF
exit
```

```
ph1=0 2
ph2=0 0 2 2
;ph3=1 1 1 1 3 3 3 3
ph3= 0 0 0 0 2 2 2 2
ph31=2 0 0 2 0 2 2 0
```

```
ph20=0
ph21=1
ph22=2
ph23=3
```

7.2.4 Backbone ¹⁵N E-CPMG

```
define delay INEPT1
define delay INEPT2
define delay INEPT3
define delay U1
prosol relations=<triple>
#include <Avance_dl.incl>

#define GRADIENT0 10u p20:gp0 200u
#define GRADIENT1 10u p21:gp1 200u
#define GRADIENT2 10u p22:gp2 200u
#define GRADIENT3 10u p23:gp3 200u
#define GRADIENT4 10u p24:gp4 200u
#define GRADIENT5 10u p25:gp5 200u
#define GRADIENT6 10u p26:gp6 200u
;define list<delay> Clist=<$VDLIST>
define list<loopcounter> cpmglist=<$VCLIST>

"p2=2*p1"
"p6=2*p5"
"in10=inf2/2"
"d10=in10/2-(p3*2 + 1.5u)"
"INEPT1=d2-(p21+p11+210u)-14u"
"INEPT2=d2-(p22+p11+210u)-14u"
"INEPT3=d2-(p23+p11+210u)-14u"
```

```
"U1=d2-p11-10u-p26-210u"  
"d13=d1-d8"  
"l2 = 1"  
aqseq 312
```

```
1 ze  
  20m st0  
2 6m  
3 3m  
4 3m  
  20u pl1:f1  
  20u pl2:f2  
  20u pl3:f3  
  if "cpmglst < 113"  
  {  
    if "cpmglst > 0"  
    {  
      "l3 = cpmglst"  
      "l4=113-l3"  
      "d14=d8/(16*13)-p5"  
      "d16=d8/(16*14)-p5"  
    }  
    else  
    {  
      "l3=0"  
      "l4=113"  
      "d14=p5"  
      "d16=p5"  
    }  
  }  
  else  
  {  
    "l3=113"  
    "l4=0"  
    "d14=p5"  
    "d16=p5"  
  }  
  d13*0.5  
  if "l3 == 113" goto 6  
  if "l3 == 0" goto 7
```

```
5 d16  
  (p6 ph21):f3  
  d16  
  d16  
  (p6 ph21):f3  
  d16  
  d16  
  (p6 ph20):f3  
  d16
```

```

d16
(p6 ph22):f3
d16
d16
(p6 ph20):f3
d16
d16
(p6 ph20):f3
d16
d16
(p6 ph21):f3
d16
d16
(p6 ph23):f3
d16
lo to 5 times 14

goto 8

6 d8

goto 8

7 (p6 ph21):f3
(p6 ph21):f3
(p6 ph20):f3
(p6 ph22):f3
(p6 ph20):f3
(p6 ph20):f3
(p6 ph21):f3
(p6 ph23):f3
lo to 7 times 14

8 10u
d13*0.5
20u p11:f1
20u p12:f2
20u p13:f3

20u LOCKH_ON
;-----first INEPT
(p5 ph20):f3
GRADIEN0
1m
(p1 ph20):f1
10u
(p11:sp1 ph18:r):f1
GRADIEN1
INEPT1 p11:f1
(center(p2 ph21):f1 (p6 ph20):f3)

```

```

GRADIENT1
INEPT1
(p11:sp1 ph19:r):f1
5u
5u p11:f1
(p1 ph23):f1
GRADIENT4
(p5 ph4):f3
;-----CPMG
if "I3 == 113" goto 10

if "I3 ==0" goto 11

9 d14
(p6 ph21):f3
d14
d14
(p6 ph21):f3
d14
d14
(p6 ph20):f3
d14
d14
(p6 ph22):f3
d14
lo to 9 times I3

goto 11

10 (p6 ph21):f3
(p6 ph21):f3
(p6 ph20):f3
(p6 ph22):f3
lo to 10 times I3
;-----U element
11 GRADIENT6
U1
(p11:sp3 ph15:r):f1
5u
5u p11:f1
(center(p2 ph20):f1 (p6 ph20):f3)
10u
(p11:sp3 ph15:r):f1
GRADIENT6
U1 p11:f1
;-----CPMG
if "I3 == 113" goto 13

if "I3 == 0" goto 14

```

```

12 d14
  (p6 ph20):f3
  d14
  d14
  (p6 ph20):f3
  d14
  d14
  (p6 ph21):f3
  d14
  d14
  (p6 ph23):f3
  d14
lo to 12 times l3

goto 14

13 (p6 ph20):f3
  (p6 ph20):f3
  (p6 ph21):f3
  (p6 ph23):f3
lo to 13 times l3

14 (p5 ph5):f3
  GRADIANT5

;-----15N evolution
if "l2 %2 == 1" goto 31
  (p5 ph2):f3
goto 32
31 (p5 ph1):f3
32 d10
  (p3 ph23 1.5u p4 ph20 1.5u p3 ph23):f2
  d10
;-----second INEPT
  (p1 ph10):f1
  10u
  (p11:sp1 ph17:r):f1
  GRADIANT2
  INEPT2 p11:f1
  (center(p2 ph20):f1 (p6 ph20):f3)
  GRADIANT2
  INEPT2
  (p11:sp1 ph16:r):f1
  5u
  5u p11:f1
  (center(p1 ph20):f1 (p5 ph12):f3)
;-----WATERGATE
  GRADIANT3
  INEPT3
  (p11:sp2 ph26:r):f1

```

```

5u
5u p11:f1
  (center(p2 ph20):f1 (p6 ph20):f3)
  10u
  (p11:sp2 ph26:r):f1
  GRADIENT3
  INEPT3 LOCKH_OFF
  (p5 ph11):f3
;-----acquisition
  goscnp ph31

  3m st cpmglist.inc
  lo to 3 times nbl

  3m cpmglist.res
  3m ipp1 ipp2 ipp4 ipp5 ipp10 ipp11 ipp12 ipp31
  lo to 4 times ns

;go=2 ph31
  1m mc #0 to 4
; F1I(Clist.inc,l31)

  F1QF()

; F2EA(ip10*2 & ip12*2 & ip17*2 & rpp1 & rpp2 & rpp4 & rpp5 & rpp10 & rpp11 &
rpp12 & rpp31 & iu2,ip1*2 & ip2*2 & ip31*2 & id10)
  F2EA(calph(ph10, +180) & calph(ph12, +180) & calph(ph17, +180) & calclc(l2, +1),
calph(ph1, +180) & calph(ph2, +180) & calph(ph31, +180) & caldel(d10, +in10))
  10u do:f1
  10u do:f2
  10u do:f3
  10u LOCKH_OFF
  exit

ph1 =1 3 2 0
ph2 =1 3 0 2
ph4 =0 0 0 0 2 2 2 2
ph5 =1 1 1 1 1 1 1 1 3 3 3 3 3 3 3 3
ph31=1 3 2 0 3 1 0 2 3 1 0 2 1 3 2 0

ph10=3 3 3 3
ph11=0 0 0 0
ph12=3 3 3 3

ph15=2
ph16=0
ph17=1
ph18=2
ph19=3

```

ph20=0
ph21=1
ph22=2
ph23=3

ph26=2

References

- Alberts, B., Johnson, A., Lewis, J., Morgan, D., Raff, M., Roberts, K., & Walter, P. (2015). Molecular Biology of the Cell, Sixth Edition. *Molecular Biology of the Cell, Sixth Edition*, 1-1342. Retrieved from <Go to ISI>://WOS:000347857100025
- Allan, D. C., & Phillips, J. C. (2017). Why Ubiquitin Has Not Evolved. *Int J Mol Sci*, 18(9). doi:10.3390/ijms18091995
- Balasubramanian, R., & Ramakrishnan, C. (1972). Stereochemical criteria for polypeptide and protein chain conformations. 8. Energy maps for a pair of non-planar peptide units having distortion of bond angle at the α -carbon atom. *Int J Pept Protein Res*, 4(2), 91-99. Retrieved from <https://www.ncbi.nlm.nih.gov/pubmed/5068925>
- Ban, D., Funk, M., Gulich, R., Egger, D., Sabo, T. M., Walter, K. F., . . . Griesinger, C. (2011). Kinetics of conformational sampling in ubiquitin. *Angew Chem Int Ed Engl*, 50(48), 11437-11440. doi:10.1002/anie.201105086
- Ban, D., Gossert, A. D., Giller, K., Becker, S., Griesinger, C., & Lee, D. (2012). Exceeding the limit of dynamics studies on biomolecules using high spin-lock field strengths with a cryogenically cooled probehead. *Journal of Magnetic Resonance*, 221, 1-4. doi:10.1016/j.jmr.2012.05.005
- Ban, D., Mazur, A., Carneiro, M. G., Sabo, T. M., Giller, K., Koharudin, L. M. I., . . . Lee, D. (2013). Enhanced accuracy of kinetic information from CT-CPMG experiments by transverse rotating-frame spectroscopy. *Journal of Biomolecular NMR*, 57(1), 73-82. doi:10.1007/s10858-013-9769-z
- Ban, D., Sabo, T. M., Griesinger, C., & Lee, D. (2013). Measuring Dynamic and Kinetic Information in the Previously Inaccessible Supra- τ (c) Window of Nanoseconds to Microseconds by Solution NMR Spectroscopy. *Molecules*, 18(10), 11904-11937. doi:10.3390/molecules181011904
- Ban, D., Smith, C. A., de Groot, B. L., Griesinger, C., & Lee, D. (2017). Recent advances in measuring the kinetics of biomolecules by NMR relaxation dispersion spectroscopy. *Arch Biochem Biophys*, 628, 81-91. doi:10.1016/j.abb.2017.05.016
- Bell, S., Klein, C., Muller, L., Hansen, S., & Buchner, J. (2002). p53 contains large unstructured regions in its native state. *Journal of Molecular Biology*, 322(5), 917-927. doi:10.1016/s0022-2836(02)00848-3
- Bjorck, L., & Kronvall, G. (1984). Purification and some properties of streptococcal protein G, a novel IgG-binding reagent. *Journal of Immunology*, 133(2), 969-974. Retrieved from <https://www.ncbi.nlm.nih.gov/pubmed/6234364>
- Borchers, W., Theillet, F. X., Katzer, A., Finzel, A., Mishall, K. M., Powell, A. T., . . . Daughdrill, G. W. (2014). Disorder and residual helicity alter p53-Mdm2 binding affinity and signaling in cells. *Nature Chemical Biology*, 10(12), 1000-1002. doi:10.1038/nchembio.1668
- Brzovic, P. S., & Klevit, R. E. (2006). Ubiquitin transfer from the E2 perspective: why is UbcH5 so promiscuous? *Cell Cycle*, 5(24), 2867-2873. doi:10.4161/cc.5.24.3592
- Carr, H. Y., & Purcell, E. M. (1954). Effects of Diffusion on Free Precession in Nuclear Magnetic Resonance Experiments. *Physical Review*, 94(3), 630-638. doi:DOI 10.1103/PhysRev.94.630
- Cavanagh, J., Fairbrother, W. J., Palmer, A. G., Rance, M., & Skelton, N. J. (2007). Protein NMR Spectroscopy: Principles and Practice, 2nd Edition. *Protein Nmr Spectroscopy: Principles and Practice, 2nd Edition*, 1-888. Retrieved from <Go to ISI>://WOS:000311353300013

- Chi, S. W., Lee, S. H., Kim, D. H., Ahn, M. J., Kim, J. S., Woo, J. Y., . . . Han, K. H. (2005). Structural details on mdm2-p53 interaction. *Journal of Biological Chemistry*, 280(46), 38795-38802. doi:10.1074/jbc.M508578200
- Delaglio, F., Grzesiek, S., Vuister, G. W., Zhu, G., Pfeifer, J., & Bax, A. (1995). NMRPipe: a multidimensional spectral processing system based on UNIX pipes. *Journal of Biomolecular NMR*, 6(3), 277-293. doi:10.1007/BF00197809
- Derrick, J. P., & Wigley, D. B. (1994). The third IgG-binding domain from streptococcal protein G. An analysis by X-ray crystallography of the structure alone and in a complex with Fab. *Journal of Molecular Biology*, 243(5), 906-918. doi:10.1006/jmbi.1994.1691
- Eichmuller, C., & Skrynnikov, N. R. (2005). A new amide proton R-1 rho experiment permits accurate characterization of microsecond time-scale conformational exchange. *Journal of Biomolecular NMR*, 32(4), 281-293. doi:10.1007/s10858-005-0658-y
- Fares, C., Lakomek, N. A., Walter, K. F., Frank, B. T., Meiler, J., Becker, S., & Griesinger, C. (2009). Accessing ns-micros side chain dynamics in ubiquitin with methyl RDCs. *Journal of Biomolecular NMR*, 45(1-2), 23-44. doi:10.1007/s10858-009-9354-7
- Fenwick, R. B., Esteban-Martin, S., Richter, B., Lee, D., Walter, K. F., Milovanovic, D., . . . Salvatella, X. (2011). Weak long-range correlated motions in a surface patch of ubiquitin involved in molecular recognition. *Journal of the American Chemical Society*, 133(27), 10336-10339. doi:10.1021/ja200461n
- Fossat, M. J., Garcia, A., Barrick, D., Roumestand, C., & Royer, C. A. (2016). Exploring Folding Cooperativity of a Repeat Protein Folding by 2D-NMR Detected Pressure Perturbation. *Biophysical Journal*, 110(3), 391a-391a. doi:DOI 10.1016/j.bpj.2015.11.2115
- Frauenfelder, H., & Wolynes, P. G. (1985). Rate Theories and Puzzles of Hemeprotein Kinetics. *Science*, 229(4711), 337-345. doi:DOI 10.1126/science.4012322
- Fu, I., Case, D. A., & Baum, J. (2015). Dynamic Water-Mediated Hydrogen Bonding in a Collagen Model Peptide. *Biochemistry*, 54(39), 6029-6037. doi:10.1021/acs.biochem.5b00622
- Glickman, M. H., & Ciechanover, A. (2002). The ubiquitin-proteasome proteolytic pathway: destruction for the sake of construction. *Physiological Reviews*, 82(2), 373-428. doi:10.1152/physrev.00027.2001
- Goldstein, G., Scheid, M., Hammerling, U., Boyse, E. A., Schlesinger, D. H., & Niall, H. D. (1975). Isolation of a Polypeptide That Has Lymphocyte-Differentiating Properties and Is Probably Represented Universally in Living Cells. *Proceedings of the National Academy of Sciences of the United States of America*, 72(1), 11-15. doi:DOI 10.1073/pnas.72.1.11
- Gronenborn, A. M., Filpula, D. R., Essig, N. Z., Achari, A., Whitlow, M., Wingfield, P. T., & Clore, G. M. (1991). A Novel, Highly Stable Fold of the Immunoglobulin Binding Domain of Streptococcal Protein-G. *Science*, 253(5020), 657-661. doi:DOI 10.1126/science.1871600
- Hall, J. B., & Fushman, D. (2003). Characterization of the overall and local dynamics of a protein with intermediate rotational anisotropy: Differentiating between conformational exchange and anisotropic diffusion in the B3 domain of protein G. *Journal of Biomolecular NMR*, 27(3), 261-275. doi:Doi 10.1023/A:1025467918856
- Hammes-Schiffer, S., & Benkovic, S. J. (2006). Relating protein motion to catalysis. *Annual Review of Biochemistry*, 75, 519-541. doi:10.1146/annurev.biochem.75.103004.142800

- Hansen, D. F., Vallurupalli, P., & Kay, L. E. (2008). An improved $(15)\text{N}$ relaxation dispersion experiment for the measurement of millisecond time-scale dynamics in proteins. *Journal of Physical Chemistry B*, *112*(19), 5898-5904. doi:10.1021/jp074793o
- Harper, J. W., & Schulman, B. A. (2006). Structural complexity in ubiquitin recognition. *Cell*, *124*(6), 1133-1136. doi:10.1016/j.cell.2006.03.009
- Haupt, C., Patzschke, R., Weininger, U., Groger, S., Kovermann, M., & Balbach, J. (2011). Transient Enzyme-Substrate Recognition Monitored by Real-Time NMR. *Journal of the American Chemical Society*, *133*(29), 11154-11162. doi:10.1021/ja2010048
- Henzler-Wildman, K. A., Lei, M., Thai, V., Kerns, S. J., Karplus, M., & Kern, D. (2007). A hierarchy of timescales in protein dynamics is linked to enzyme catalysis. *Nature*, *450*(7171), 913-U927. doi:10.1038/nature06407
- Hicke, L., Schubert, H. L., & Hill, C. P. (2005). Ubiquitin-binding domains. *Nature Reviews: Molecular Cell Biology*, *6*(8), 610-621. doi:10.1038/nrm1701
- Ishima, R. (2012). Recent Developments in N-15 NMR Relaxation Studies that Probe Protein Backbone Dynamics. *Nmr of Proteins and Small Biomolecules*, *326*, 99-122. doi:10.1007/128_2011_212
- Ishima, R., & Torchia, D. A. (2003). Extending the range of amide proton relaxation dispersion experiments in proteins using a constant-time relaxation-compensated CPMG approach. *Journal of Biomolecular NMR*, *25*(3), 243-248. doi:10.1023/A:1022851228405
- Jebelli, J. D., Hooper, C., Garden, G. A., & Pocock, J. M. (2012). Emerging roles of p53 in glial cell function in health and disease. *Glia*, *60*(4), 515-525. doi:10.1002/glia.22268
- Kliza, K., & Husnjak, K. (2020). Resolving the Complexity of Ubiquitin Networks. *Front Mol Biosci*, *7*, 21. doi:10.3389/fmolb.2020.00021
- Kolano, C., Helbing, J., Kozinski, M., Sander, W., & Hamm, P. (2006). Watching hydrogen-bond dynamics in a beta-turn by transient two-dimensional infrared spectroscopy. *Nature*, *444*(7118), 469-472. doi:10.1038/nature05352
- Korzhnev, D. M., Salvatella, X., Vendruscolo, M., Di Nardo, A. A., Davidson, A. R., Dobson, C. M., & Kay, L. E. (2004). Low-populated folding intermediates of Fyn SH3 characterized by relaxation dispersion NMR. *Nature*, *430*(6999), 586-590. doi:10.1038/nature02655
- Kussie, P. H., Gorina, S., Marechal, V., Elenbaas, B., Moreau, J., Levine, A. J., & Pavletich, N. P. (1996). Structure of the MDM2 oncoprotein bound to the p53 tumor suppressor transactivation domain. *Science*, *274*(5289), 948-953. doi:10.1126/science.274.5289.948
- Lange, O. F., Lakomek, N. A., Fares, C., Schroder, G. F., Walter, K. F., Becker, S., . . . de Groot, B. L. (2008). Recognition dynamics up to microseconds revealed from an RDC-derived ubiquitin ensemble in solution. *Science*, *320*(5882), 1471-1475. doi:10.1126/science.1157092
- Lazar, G. A., Desjarlais, J. R., & Handel, T. M. (1997). De novo design of the hydrophobic core of ubiquitin. *Protein Science*, *6*(6), 1167-1178. doi:10.1002/pro.5560060605
- Lee, H., Mok, K. H., Muhandiram, R., Park, K. H., Suk, J. E., Kim, D. H., . . . Han, K. H. (2000). Local structural elements in the mostly unstructured transcriptional activation domain of human p53. *Journal of Biological Chemistry*, *275*(38), 29426-29432. doi:10.1074/jbc.M003107200
- Lindorff-Larsen, K., Maragakis, P., Piana, S., & Shaw, D. E. (2016). Picosecond to Millisecond Structural Dynamics in Human Ubiquitin. *J Phys Chem B*, *120*(33), 8313-8320. doi:10.1021/acs.jpcc.6b02024

- Lipari, G., & Szabo, A. (1982a). Model-Free Approach to the Interpretation of Nuclear Magnetic-Resonance Relaxation in Macromolecules .1. Theory and Range of Validity. *Journal of the American Chemical Society*, *104*(17), 4546-4559. doi:DOI 10.1021/ja00381a009
- Lipari, G., & Szabo, A. (1982b). Model-Free Approach to the Interpretation of Nuclear Magnetic-Resonance Relaxation in Macromolecules .2. Analysis of Experimental Results. *Journal of the American Chemical Society*, *104*(17), 4559-4570. doi:DOI 10.1021/ja00381a010
- Loria, J. P., Rance, M., & Palmer, A. G., 3rd. (1999). A TROSY CPMG sequence for characterizing chemical exchange in large proteins. *Journal of Biomolecular NMR*, *15*(2), 151-155. doi:10.1023/a:1008355631073
- Luz, Z., & Meiboom, S. (1963). Nuclear Magnetic Resonance Study of Protolysis of Trimethylammonium Ion in Aqueous Solution - Order of Reaction with Respect to Solvent. *Journal of Chemical Physics*, *39*(2), 366-&. doi:Doi 10.1063/1.1734254
- Markus, M. A., Dayie, K. T., Matsudaira, P., & Wagner, G. (1994). Effect of deuteration on the amide proton relaxation rates in proteins. Heteronuclear NMR experiments on villin 14T. *J Magn Reson B*, *105*(2), 192-195. doi:10.1006/jmrb.1994.1122
- Marlow, M. S., Dogan, J., Frederick, K. K., Valentine, K. G., & Wand, A. J. (2010). The role of conformational entropy in molecular recognition by calmodulin. *Nature Chemical Biology*, *6*(5), 352-358. doi:10.1038/nchembio.347
- Marsh, J. A., Singh, V. K., Jia, Z., & Forman-Kay, J. D. (2006). Sensitivity of secondary structure propensities to sequence differences between alpha- and gamma-synuclein: implications for fibrillation. *Protein Science*, *15*(12), 2795-2804. doi:10.1110/ps.062465306
- McConnell, H. M. (1958). Reaction Rates by Nuclear Magnetic Resonance. *Journal of Chemical Physics*, *28*(3), 430-431. doi:Doi 10.1063/1.1744152
- Meiboom, S., & Gill, D. (1958). Modified Spin-Echo Method for Measuring Nuclear Relaxation Times. *Review of Scientific Instruments*, *29*(8), 688-691. doi:Doi 10.1063/1.1716296
- Meier, B. H., & Ernst, R. R. (1979). Elucidation of Chemical-Exchange Networks by 2-Dimensional Nmr-Spectroscopy - Heptamethylbenzenonium Ion. *Journal of the American Chemical Society*, *101*(21), 6441-6442. doi:DOI 10.1021/ja00515a053
- Meiler, J., Prompers, J. J., Peti, W., Griesinger, C., & Bruschweiler, R. (2001). Model-free approach to the dynamic interpretation of residual dipolar couplings in globular proteins. *Journal of the American Chemical Society*, *123*(25), 6098-6107. doi:10.1021/ja010002z
- Michielssens, S., Peters, J. H., Ban, D., Pratihari, S., Seeliger, D., Sharma, M., . . . de Groot, B. L. (2014). A designed conformational shift to control protein binding specificity. *Angew Chem Int Ed Engl*, *53*(39), 10367-10371. doi:10.1002/anie.201403102
- Mills, J. L., & Szyperski, T. (2002). Protein dynamics in supercooled water: The search for slow motional modes. *Journal of Biomolecular NMR*, *23*(1), 63-67. doi:Doi 10.1023/A:1015397305148
- Neal, S., Nip, A. M., Zhang, H. Y., & Wishart, D. S. (2003). Rapid and accurate calculation of protein H-1, C-13 and N-15 chemical shifts. *Journal of Biomolecular NMR*, *26*(3), 215-240. doi:Doi 10.1023/A:1023812930288
- Neira, J. L. (2013). NMR as a tool to identify and characterize protein folding intermediates. *Archives of Biochemistry and Biophysics*, *531*(1-2), 90-99. doi:10.1016/j.abb.2012.09.003

- Neudecker, P., Lundstrom, P., & Kay, L. E. (2009). Relaxation Dispersion NMR Spectroscopy as a Tool for Detailed Studies of Protein Folding. *Biophysical Journal*, *96*(6), 2045-2054. doi:10.1016/j.bpj.2008.12.3907
- Palmer, A. G., 3rd. (2004). NMR characterization of the dynamics of biomacromolecules. *Chem Rev*, *104*(8), 3623-3640. doi:10.1021/cr030413t
- Palmer, A. G., 3rd, & Massi, F. (2006). Characterization of the dynamics of biomacromolecules using rotating-frame spin relaxation NMR spectroscopy. *Chem Rev*, *106*(5), 1700-1719. doi:10.1021/cr0404287
- Palmer, A. G., Kroenke, C. D., & Loria, J. P. (2001). Nuclear magnetic resonance methods for quantifying microsecond-to-millisecond motions in biological macromolecules. *Nuclear Magnetic Resonance of Biological Macromolecules, Pt B*, *339*, 204-238. doi:10.1016/S0076-6879(01)39315-1
- Pawson, T. (1995). Protein Modules and Signaling Networks. *Nature*, *373*(6515), 573-580. doi:10.1038/373573a0
- Peters, J. H., & de Groot, B. L. (2012). Ubiquitin dynamics in complexes reveal molecular recognition mechanisms beyond induced fit and conformational selection. *PLoS Comput Biol*, *8*(10), e1002704. doi:10.1371/journal.pcbi.1002704
- Peti, W., Meiler, J., Bruschweiler, R., & Griesinger, C. (2002). Model-free analysis of protein backbone motion from residual dipolar couplings. *Journal of the American Chemical Society*, *124*(20), 5822-5833. doi:10.1021/ja011883c
- Piana, S., Lindorff-Larsen, K., & Shaw, D. E. (2013). Atomic-level description of ubiquitin folding. *Proc Natl Acad Sci U S A*, *110*(15), 5915-5920. doi:10.1073/pnas.1218321110
- Pratihari, S., Sabo, T. M., Ban, D., Fenwick, R. B., Becker, S., Salvatella, X., . . . Lee, D. (2016). Kinetics of the Antibody Recognition Site in the Third IgG-Binding Domain of Protein G. *Angew Chem Int Ed Engl*, *55*(33), 9567-9570. doi:10.1002/anie.201603501
- Ramakrishnan, C., & Ramachandran, G. N. (1965). Stereochemical criteria for polypeptide and protein chain conformations. II. Allowed conformations for a pair of peptide units. *Biophysical Journal*, *5*(6), 909-933. doi:10.1016/S0006-3495(65)86759-5
- Reddy, J. G., Pratihari, S., Ban, D., Frischkorn, S., Becker, S., Griesinger, C., & Lee, D. (2018). Simultaneous determination of fast and slow dynamics in molecules using extreme CPMG relaxation dispersion experiments. *Journal of Biomolecular NMR*, *70*(1), 1-9. doi:10.1007/s10858-017-0155-0
- Reif, B., Hennig, M., & Griesinger, C. (1997). Direct measurement of angles between bond vectors in high-resolution NMR. *Science*, *276*(5316), 1230-1233. doi:10.1126/science.276.5316.1230
- Robustelli, P., Piana, S., & Shaw, D. E. (2020). Mechanism of Coupled Folding-upon-Binding of an Intrinsically Disordered Protein. *Journal of the American Chemical Society*, *142*(25), 11092-11101. doi:10.1021/jacs.0c03217
- Royds, J. A., & Iacopetta, B. (2006). p53 and disease: when the guardian angel fails. *Cell Death and Differentiation*, *13*(6), 1017-1026. doi:10.1038/sj.cdd.4401913
- Sabo, T. M., Smith, C. A., Ban, D., Mazur, A., Lee, D., & Griesinger, C. (2014). ORIUM: Optimized RDC-based Iterative and Unified Model-free analysis. *Journal of Biomolecular NMR*, *58*(4), 287-301. doi:10.1007/s10858-013-9775-1
- Sakakibara, D., Sasaki, A., Ikeya, T., Hamatsu, J., Hanashima, T., Mishima, M., . . . Ito, Y. (2009). Protein structure determination in living cells by in-cell NMR spectroscopy. *Nature*, *458*(7234), 102-105. doi:10.1038/nature07814

- Schon, O., Friedler, A., Bycroft, M., Freund, S. M. V., & Fersht, A. R. (2002). Molecular mechanism of the interaction between MDM2 and p53. *Journal of Molecular Biology*, 323(3), 491-501. doi:10.1016/S0022-2836(02)00852-5
- Schutz, S., & Sprangers, R. (2020). Methyl TROSY spectroscopy: A versatile NMR approach to study challenging biological systems. *Progress in Nuclear Magnetic Resonance Spectroscopy*, 116, 56-84. doi:10.1016/j.pnmrs.2019.09.004
- Shapovalov, M. V., & Dunbrack, R. L., Jr. (2011). A smoothed backbone-dependent rotamer library for proteins derived from adaptive kernel density estimates and regressions. *Structure*, 19(6), 844-858. doi:10.1016/j.str.2011.03.019
- Shen, Y., & Bax, A. (2007). Protein backbone chemical shifts predicted from searching a database for torsion angle and sequence homology. *Journal of Biomolecular NMR*, 38(4), 289-302. doi:10.1007/s10858-007-9166-6
- Smith, C. A., Ban, D., Pratihari, S., Giller, K., Paulat, M., Becker, S., . . . de Groot, B. L. (2016). Allosteric switch regulates protein-protein binding through collective motion. *Proc Natl Acad Sci U S A*, 113(12), 3269-3274. doi:10.1073/pnas.1519609113
- Smith, C. A., Ban, D., Pratihari, S., Giller, K., Schwiegk, C., de Groot, B. L., . . . Lee, D. (2015). Population shuffling of protein conformations. *Angew Chem Int Ed Engl*, 54(1), 207-210. doi:10.1002/anie.201408890
- Swenson, J., Jansson, H., & Bergman, R. (2006). Relaxation processes in supercooled confined water and implications for protein dynamics. *Physical Review Letters*, 96(24). doi:ARTN 247802
10.1103/PhysRevLett.96.247802
- Tang, Q. Y., & Kaneko, K. (2021). Dynamics-Evolution Correspondence in Protein Structures. *Physical Review Letters*, 127(9), 098103. doi:10.1103/PhysRevLett.127.098103
- Theillet, F. X., Binolfi, A., Bekei, B., Martorana, A., Rose, H. M., Stuiver, M., . . . Selenko, P. (2016). Structural disorder of monomeric alpha-synuclein persists in mammalian cells. *Nature*, 530(7588), 45-50. doi:10.1038/nature16531
- Tompa, P. (2012). Intrinsically disordered proteins: a 10-year recap. *Trends in Biochemical Sciences*, 37(12), 509-516. doi:10.1016/j.tibs.2012.08.004
- Tugarinov, V., Hwang, P. M., Ollershaw, J. E., & Kay, L. E. (2003). Cross-correlated relaxation enhanced H-1-C-13 NMR spectroscopy of methyl groups in very high molecular weight proteins and protein complexes. *Journal of the American Chemical Society*, 125(34), 10420-10428. doi:10.1021/ja030153x
- Tugarinov, V., Kanelis, V., & Kay, L. E. (2006). Isotope labeling strategies for the study of high-molecular-weight proteins by solution NMR spectroscopy. *Nat Protoc*, 1(2), 749-754. doi:10.1038/nprot.2006.101
- Tzeng, S. R., & Kalodimos, C. G. (2012). Protein activity regulation by conformational entropy. *Nature*, 488(7410), 236-240. doi:10.1038/nature11271
- Ulmer, T. S., Campbell, I. D., & Boyd, J. (2004). Amide proton relaxation measurements employing a highly deuterated protein. *Journal of Magnetic Resonance*, 166(2), 190-201. doi:10.1016/j.jmr.2003.10.012
- Vijay-Kumar, S., Bugg, C. E., & Cook, W. J. (1987). Structure of ubiquitin refined at 1.8 Å resolution. *Journal of Molecular Biology*, 194(3), 531-544. doi:10.1016/0022-2836(87)90679-6
- Vijay-Kumar, S., Bugg, C. E., Wilkinson, K. D., & Cook, W. J. (1985). Three-dimensional structure of ubiquitin at 2.8 Å resolution. *Proc Natl Acad Sci U S A*, 82(11), 3582-3585. doi:10.1073/pnas.82.11.3582

- Voet, J. G., & Voet, D. (2000). Biochemistry and molecular biology education (BAMBE). *Biochemical Education*, 28(3), 124-124. doi:Doi 10.1016/S0307-4412(00)00032-7
- Vogeli, B., Kazemi, S., Guntert, P., & Riek, R. (2012). Spatial elucidation of motion in proteins by ensemble-based structure calculation using exact NOEs. *Nature Structural & Molecular Biology*, 19(10), 1053-U1110. doi:10.1038/nsmb.2355
- Vousden, K. H., & Lane, D. P. (2007). p53 in health and disease. *Nature Reviews: Molecular Cell Biology*, 8(4), 275-283. doi:10.1038/nrm2147
- Wilkinson, K. D. (2005). The discovery of ubiquitin-dependent proteolysis. *Proc Natl Acad Sci U S A*, 102(43), 15280-15282. doi:10.1073/pnas.0504842102
- Williamson, M. P., Havel, T. F., & Wuthrich, K. (1985). Solution conformation of proteinase inhibitor IIA from bull seminal plasma by 1H nuclear magnetic resonance and distance geometry. *Journal of Molecular Biology*, 182(2), 295-315. doi:10.1016/0022-2836(85)90347-x
- Wolf-Watz, M., Thai, V., Henzler-Wildman, K., Hadjipavlou, G., Eisenmesser, E. Z., & Kern, D. (2004). Linkage between dynamics and catalysis in a thermophilic-mesophilic enzyme pair. *Nature Structural & Molecular Biology*, 11(10), 945-949. doi:10.1038/nsmb821
- Wuthrich, K., & Wagner, G. (1975). Nmr Investigations of Dynamics of Aromatic Amino-Acid Residues in Basic Pancreatic Trypsin-Inhibitor. *FEBS Letters*, 50(2), 265-268. doi:Doi 10.1016/0014-5793(75)80504-7
- Yang, D. W., Mok, Y. K., FormanKay, J. D., Farrow, N. A., & Kay, L. E. (1997). Contributions to protein entropy and heat capacity from bond vector motions measured by NMR spin relaxation. *Journal of Molecular Biology*, 272(5), 790-804. doi:DOI 10.1006/jmbi.1997.1285
- Yao, L., Vogeli, B., Torchia, D. A., & Bax, A. (2008). Simultaneous NMR study of protein structure and dynamics using conservative mutagenesis. *Journal of Physical Chemistry B*, 112(19), 6045-6056. doi:10.1021/jp0772124
- Yip, G. N., & Zuiderweg, E. R. (2004). A phase cycle scheme that significantly suppresses offset-dependent artifacts in the R2-CPMG 15N relaxation experiment. *Journal of Magnetic Resonance*, 171(1), 25-36. doi:10.1016/j.jmr.2004.06.021
- Zeeb, M., & Balbach, J. (2004). Protein folding studied by real-time NMR spectroscopy. *Methods*, 34(1), 65-74. doi:10.1016/j.ymeth.2004.03.014
- Zhang, Q., Stelzer, A. C., Fisher, C. K., & Al-Hashimi, H. M. (2007). Visualizing spatially correlated dynamics that directs RNA conformational transitions. *Nature*, 450(7173), 1263-1267. doi:10.1038/nature06389

Curriculum Vitae

Personal Details

Name: Supriya Pratihar
Date of Birth: 12.04.88
Place of Birth: Kantapahari, India

Education

- 2013–Present Ph.D. Student, Georg-August University School of Science, Max Planck Institute for Biophysical Chemistry, Göttingen, Germany
Supervisor: Prof. Dr. Christian Griesinger
- 2010–2013 M. Sc., Department of Chemical Science
Tata Institute of Fundamental Research, Mumbai, India
Thesis: NMR Characterisation of DLC8 Protein: In-vitro and In-cell Investigation
Supervisor: Prof. Dr. R. V. Hosur
- 2005–2008 B. Sc., Department of Chemistry
College: Ramakrisna Mission Vidyamandira
University: Calcutta University, Kolkata, India

Publications

1. A litmus test for classification of recognition mechanisms of transiently binding proteins. (under review in Nature Communications)
2. Common origin of backbone and side-chain dynamics found with ^{13}C E-CPMG. (under preparation)
3. Direct detection of pincer mode motion in Ubiquitin from ^1H E-CPMG. (under preparation)
4. Rapid Conformational Exchange in intrinsically disordered p53-TAD domain. (under preparation)
5. Movellan, K. T.; Najbauer, E. E.; **Pratihar, S.**; Salvi, M.; Giller, K.; Becker, S.; Andreas, L. B., Alpha protons as NMR probes in deuterated proteins. *J Biomol NMR* **2019**.
6. Reddy, J. G.; **Pratihar, S.**; Ban, D.; Frischkorn, S.; Becker, S.; Griesinger, C.; Lee, D., Simultaneous determination of fast and slow dynamics in molecules using extreme CPMG relaxation dispersion experiments. *J Biomol NMR* **2018**, *70* (1), 1-9.
7. **Pratihar, S.**; Sabo, T. M.; Ban, D.; Fenwick, R. B.; Becker, S.; Salvatella, X.; Griesinger, C.; Lee, D., Kinetics of the Antibody Recognition Site in the Third IgG-Binding Domain of Protein G. *Angew Chem Int Ed* **2016**, *55* (33), 9567-70.
8. Chakrabarti, K. S.; Ban, D.; **Pratihar, S.**; Reddy, J. G.; Becker, S.; Griesinger, C.; Lee, D., High-power ^1H composite pulse decoupling provides artifact free exchange-mediated saturation transfer (EST) experiments. *J Magn Reson* **2016**, *269*, 65-9.
9. Smith, C. A.; Ban, D.; **Pratihar, S.**; Giller, K.; Paulat, M.; Becker, S.; Griesinger, C.; Lee, D.; de Groot, B. L., Allosteric switch regulates protein-protein binding through collective motion. *Proc Natl Acad Sci U S A*, **2016**, *113* (12), 3269-74.
10. Smith, C. A.; Ban, D.; **Pratihar, S.**; Giller, K.; Schwiegk, C.; de Groot, B. L.; Becker, S.; Griesinger, C.; Lee, D., Population shuffling of protein conformations. *Angew Chem Int Ed* **2015**, *54* (1), 207-10.

11. Michielssens, S.; Peters, J. H.; Ban, D.; **Pratihari, S.**; Seeliger, D.; Sharma, M.; Giller, K.; Sabo, T. M.; Becker, S.; Lee, D.; Griesinger, C.; de Groot, B. L., A designed conformational shift to control protein binding specificity. *Angew Chem Int Ed* **2014**, *53* (39), 10367-71.
12. Anoop, A.; Ranganathan, S.; Das Dhaked, B.; Jha, N. N.; **Pratihari, S.**; Ghosh, S.; Sahay, S.; Kumar, S.; Das, S.; Kombrabail, M.; Agarwal, K.; Jacob, R. S.; Singru, P.; Bhaumik, P.; Padinhateeri, R.; Kumar, A.; Maji, S. K., *J Biol Chem* **2014**, *289* (24), 16884-903.
13. Mithu, V. S.; **Pratihari, S.**; Paul, S.; Madhu, P. K., Efficiency of heteronuclear dipolar decoupling schemes in solid-state NMR: investigation of effective transverse relaxation times. *J Magn Reson* **2012**, *220*, 8-17.
14. Chakraborty, S.; **Pratihari, S.**; Hosur, R. V., NMR derived model of GTPase effector domain (GED) self association: relevance to dynamin assembly. *Plos One* **2012**, *7* (1), e30109.

Oral Communications in Conferences

- 2020 Functionally relevant rapid protein motions captured with high power Relaxation Dispersion in dedicated solution-NMR probe, **61st ENC**
8th – 13th March, 2020, Baltimore, Maryland, USA
- 2020 Application of Relaxation Dispersion Experiments
4th G-NMR School, Gottingen, Germany
- 2018 Capturing Protein Dynamics with Unprecedented Speed by High Power Relaxation Measurements, European Magnetic Resonance Conference (**EUROMAR**)
1st – 5th July 2018, Nantes, France
- 2017 Supra- τ_c Protein Dynamics from High-Power Relaxation Dispersion Experiments
ISMAR, 23rd – 28th July, Quebec, Canada

